ADVANCED METHODS FOR CONTROLLING UNTETHERED MAGNETIC DEVICES USING ROTATING MAGNETIC FIELDS

by

Arthur W. Mahoney Jr.

A dissertation submitted to the faculty of
The University of Utah
in partial fulfillment of the requirements for the degree of

Doctor of Philosophy

in

Computing

School of Computing

The University of Utah

August 2014

The University of Utah Graduate School

STATEMENT OF DISSERTATION APPROVAL

The dissertation of **Arthur W. Mahoney Jr.**

has been approved by the following supervisory committee members:

Jake J. Abbott	, Chair	**4/30/2014** Date Approved
John M. Hollerbach	, Member	**4/30/2014** Date Approved
Jur P. van den Berg	, Member	**5/28/2014** Date Approved
William R. Provancher	, Member	**4/30/2014** Date Approved
Stephen A. Mascaro	, Member	**4/30/2014** Date Approved

and by **Ross T. Whitaker**, Chair/Dean of

the Department/College/School of **Computing**

and by David B. Kieda, Dean of The Graduate School.

ABSTRACT

This dissertation presents results documenting advancements on the control of untethered magnetic devices, such as magnetic "microrobots" and magnetically actuated capsule endoscopes, motivated by problems in minimally invasive medicine. This dissertation focuses on applying *rotating* magnetic fields for magnetic manipulation. The contributions include advancements in the way that helical microswimmers (devices that mimic the propulsion of bacterial flagella) are controlled in the presence of gravitational forces, advancements in ways that groups of untethered magnetic devices can be differentiated and semi-independently controlled, advancements in the way that untethered magnetic device can be controlled with a single rotating permanent magnet, and an improved understanding in the nature of the magnetic force applied to an untethered device by a rotating magnet.

CONTENTS

LIST OF FIGURES

ACKNOWLEDGMENTS

I have received support, encouragement, and mentorship from many people during my studies. I give Dr. Jake Abbott a tremendous amount of credit for my growth as a researcher and an individual. Dr. Abbott has been a mentor, a colleague, and a friend through this journey, and his guidance has made this effort fruitful and enjoyable. I am grateful to the members of the Telerobotics Laboratory for friendship, thoughtful conversation, encouragement, and insight. I acknowledge my family (especially Kris, my wife) for patience, encouragement, and support through this effort. Finally, I thank my father, Dr. Arthur Mahoney, and my sister, Dr. Cynthia Furse, for the inspiration to embark on this journey, along with my teacher, Russell Weeks, who "started the ball rolling" in the first place.

This work is largely funded by the National Science Foundation through a Graduate Research Fellowship, an Integrative Graduate Education and Research Traineeship (no. 0654414), and a Faculty Early Career Development grant (no. 0952718).

CHAPTER 1

INTRODUCTION

Untethered magnetic devices, such as magnetic "microrobots" [1] and magnetically actuated capsule endoscopes [2], have become an active area of research because of their potential impact to minimally invasive medicine. These devices typically consist of a rigidly attached magnetic body on which magnetic forces and torques are applied by an external field. These devices can be viewed as end-effectors of a larger robotic system, and they may range in size from the microscale to the mesoscale.

Let the magnetic field be denoted by the vector $\mathbf{h} \in \mathbb{R}^3\,\mathrm{A/m}$ and let the vector $\mathbf{m} \in \mathbb{R}^3\,\mathrm{A{\cdot}m^2}$ be the magnetic device's dipole moment (the product of magnetization of the device's magnetic body and the volume of the magnetic body). The magnetic torque applied to the dipole moment $\mathbf{m}$ is related to the applied magnetic field $\mathbf{h}$ at the position of the device's magnetic body:

$$\boldsymbol{\tau} = \mu_0 \mathbf{m} \times \mathbf{h}, \tag{1.1}$$

where $\mu_0 = 4\pi \times 10^{-7}\,\mathrm{N{\cdot}A^{-2}}$ is the permeability of free-space. The magnetic force applied to the dipole moment $\mathbf{m}$ is related to the spatial derivative of the applied magnetic field at the position of the device's magnetic body:

$$\mathbf{f} = \mu_0 (\mathbf{m} \cdot \nabla)\mathbf{h}. \tag{1.2}$$

In general, with increasing distance d from the magnetic source, the magnitude of the applied field (and thus the magnetic torque) tends to decrease as d^{-3}, and the gradient of the magnetic field (and thus the magnetic force) tends to decrease as d^{-4}. For clinical applications, where the distance between the magnetic field source and the untethered magnetic device may be large, this scaling indicates that propulsion methods that employ magnetic torque may be preferable to methods that employ magnetic force [3]. Untethered device propulsion strategies making use of magnetic torque include those that employ rolling [4]–[10], helical propulsion [9]–[19], resonant behavior [20], [21], stick-slip locomotion [22], and screw propulsion through tissue [23], [24]. In order to generate continuous propulsion, all

of these techniques make use of continuously rotating magnetic fields. Rotating magnetic fields are generally created in one of two ways: 1) a sinusoidal electrical current flowing through an arrangement of electromagnets and 2) with a rotating permanent magnet.

1.1 Controlling Untethered Magnetic Devices with Electromagnets

Electromagnetic systems generate magnetic fields using the physical phenomenon known by *Ampere's Law*, which relates the current flowing through an oriented contour to the magnetic field flowing through the contour's boundary. Electromagnets are particularly attractive for magnetic manipulation because the magnitude of the magnetic field produced by an electromagnet is proportional to the magnitude of the current flowing through the electromagnet, which makes an electromagnet's field easy to control. Additionally, an electromagnet's geometry can be designed to specifically tailor the generated magnetic fields for particular tasks. A common electromagnet arrangement is the Helmholtz configuration, which produces uniform magnetic fields in the center of the Helmholtz system, where magnetic devices are actuated. Uniform magnetic fields apply no magnetic force to an untethered device, only magnetic torque, which greatly simplifies control.

Helmholtz systems are particularly well suited for bench-top manipulation applications where a large workspace is not needed. One such application for which Helmholtz systems have been almost exclusively employed is for the control of helical microswimmers, which mimic bacterial flagellar propulsion, in three-dimensional fluidic volumes for microscale manipulation tasks. Typical experimental setups contain a microscope looking downward into the center of the electromagnet system where a microscope slide is placed that contains a microscale swimmer and the objects for manipulation (e.g., biological cells). Helical microswimmers have been demonstrated to be quite useful for both contact and noncontact (using fluidic flow) manipulation [25]–[27]. Helical microswimmers tend to sink under their own weight, making three-dimensional control difficult, particularly when observed through a microscope from the top down. Consequently, helical microswimmers have been nearly exclusively limited to manipulation on the two-dimensional surface of the microscope slide for simplicity. The necessary rotating field inputs that cause a microswimmer to travel at a desired three-dimensional spatial velocity is difficult to determine intuitively. *Chapter 2 describes a published open-loop method for controlling the spatial velocity of helical microswimmers in uniform magnetic fields with the presence of gravity [16].* The approach enables intuitive three-dimensional control of helical swimmers, eliminating the need to restrict their operation to the two-dimensional surface of a microscope slide.

If one untethered magnetic device is useful for manipulating objects at the microscale, then a group of untethered magnetic devices must be better! A grand challenge for magnetic manipulation systems is the ability to perform manipulation using multiple, independently controllable magnetic devices in concert (note that the micromanipulation community generally refers to untethered magnetic devices as "microrobots") [28]. Such control is difficult in the uniform magnetic field generated by a Helmholtz system because each microrobot experiences the same actuating signal. Differentiating the individual response of microrobots in a group is an active area of research. *Chapter 3 details a published method for exploiting the behavior of rotating magnetic microrobots when actuated above their step-out frequencies (the maximum field rotation frequency where a microrobot's rotation remains synchronized with the rotating field) to add an additional dimension of microrobot differentiation to multimicrorobot systems [19].* The behavior of rotating microrobots above their step-out frequency is difficult to intuit. Consequently, prior work has assumed that microrobots should always be actuated beneath their step-out frequency.

1.2 Controlling Untethered Magnetic Devices with Permanent Magnets

The second, but less common, method for generating a rotating magnetic field is with a rotating permanent magnet. Permanent magnets maintain a persistent dipole-shaped magnetic field due the fixed alignment of the magnet's internal microcrystalline structure (which is set during the manufacturing process). Compared to electromagnets, permanent-magnet systems are able to produce stronger magnetic fields in smaller form-factors without consuming power. However, control with a rotating permanent magnet is more difficult than with electromagnets because the behavior of the rotating dipole field is difficult to visualize. As a result, all prior work has followed simple approaches that operate untethered magnetic device in regions where the behavior of the rotating dipole field is simple and easy to understand. *Chapter 4 present published analysis of rotating dipole-field behavior and a method for controlling the rotation axis of a rotating permanent magnet so that an untethered magnetic device can be controlled in any position [10].* That is, control of a magnetic device is no longer limited to regions where the rotating field behavior is easy to understand.

The magnetic force applied to an untethered magnetic device by a rotating permanent magnet has not been well understood. In fact, it has generally been accepted that the magnetic force is always attractive in nature. However, I have found that by adjusting the angular velocity of the rotating permanent magnet, the applied magnetic force can actually be manipulated to point in a lateral direction (i.e., neither attractive nor repulsive). *Chapter*

5 describes a published study that describes this phenomenon and exploits it to contribute to the propulsion of a rolling magnetic device (in concert with the applied magnetic torque) and to limit the attractive force for safety [8]. Prior work has not fully exploited the available magnetic force to contribute to propulsion of an untethered magnetic device alongside the contribution of the applied magnetic torque. The ability to simultaneously utilize the available magnetic torque and force for propulsion and the ability to limit the magnetic force for safety, is particularly useful for clinical applications, where a magnetic device may be called upon to operate in a high friction environment (e.g., the small intestine) with the rotating actuator permanent magnet positioned far from the untethered device.

Chapter 6 presents a discussion of future possibilities for magnetic manipulation, and finally, concluding statements are presented in Chapter 7.

1.3 References

[1] B. J. Nelson, I. K. Kaliakatsos, and J. J. Abbott, "Microrobots for minimally invasive medicine," *Annu. Rev. Biomed. Eng.*, vol. 12, pp. 55–85, 2010.

[2] J. L. Toennies, G. Tortora, M. Simi, P. Valdastri, and R. J. Webster III, "Swallowable medical devices for diagnosis and surgery: the state of the art," *J. Mech. Eng. Sci.*, vol. 224, no. 7, pp. 1397–1414, 2010.

[3] J. J. Abbott, K. E. Peyer, M. Cosentino Lagomarsino, L. Zhang, L. X. Dong, I. K. Kaliakatsos, and B. J. Nelson, "How should microrobots swim?" *Int. J. Robot. Res.*, vol. 28, no. 11–12, pp. 1434–1447, 2009.

[4] M. T. Hou, H.-M. Shen, G.-L. Jiang, C.-N. Lu, I.-J. Hsu, and J. A. Yeh, "A rolling locomotion method for untethered magnetic microrobots," *Appl. Phys. Lett.*, vol. 96, no. 024102, pp. 1–3, 2010.

[5] G.-L. Jiang, Y.-H. Guu, C.-N. Lu, P.-K. Li, H.-M. Shen, L.-S. Lee, J. A. Yeh, and M. T.-K. Hou, "Development of rolling magnetic microrobots," *J. Micromech. Microeng.*, vol. 20, no. 085042, pp. 1–11, 2010.

[6] S. Yim and M. Sitti, "Design and rolling locomotion of a magnetically actuated soft capsule endoscope," *IEEE Trans. Robot.*, vol. 28, no. 1, pp. 183–194, 2012.

[7] G. Lien, C. Liu, J. Jiang, C. Chuang, and M. Teng, "Magnetic control system targeted for capsule endoscopic operations in the stomach: design, fabrication, and in vitro and ex vivo evaluations," *IEEE Trans. Biomed. Eng.*, vol. 59, no. 7, pp. 2068–2079, 2012.

[8] A. W. Mahoney and J. J. Abbott, "Managing magnetic force applied to a magnetic device by a rotating dipole field," *Appl. Phys. Lett.*, vol. 99, no. 134103, pp. 1–3, 2011.

[9] A. W. Mahoney, D. L. Cowan, K. M. Miller, and J. J. Abbott, "Control of untethered magnetically actuated tools using a rotating permanent magnet in any position," in *Proc. IEEE Int. Conf. Robot. Autom.*, 2012, pp. 3375–3380.

[10] A. W. Mahoney and J. J. Abbott, "Generating rotating magnetic fields with a single permanent magnet for propulsion of untethered magnetic devices in a lumen," *IEEE Trans. Robot.*, vol. 30, no. 2, pp. 411–420, 2014.

[11] M. Sendoh, K. Ishiyama, and K. I. Arai, "Direction and individual control of magnetic micromachine," *IEEE Trans. Magn.*, vol. 38, no. 5, pp. 3356–3358, 2002.

[12] ——, "Fabrication of magnetic actuator for use in a capsule endoscope," *IEEE Trans. Magn.*, vol. 39, no. 5, pp. 3232–3234, 2003.

[13] W. Zhang, Y. Chen, and P. Huang, "Study on the system of a capsule endoscope driven by an outer rotational magnetic field," in *Proc. IEEE/ASME Int. Conf. Mechatronic, Embedded Syst., Appl.*, 2006, pp. 1–5.

[14] L. Zhang, J. J. Abbott, L. X. Dong, B. E. Kratochvil, D. Bell, and B. J. Nelson, "Artificial bacterial flagella: fabrication and magnetic control," *Appl. Phys. Lett.*, vol. 94, no. 064107, pp. 1–3, 2009.

[15] L. Zhang, J. J. Abbott, L. X. Dong, K. E. Peyer, B. E. Kratochvil, H. Zhang, C. Bergeles, and B. J. Nelson, "Characterizing the swimming properties of artificial bacterial flagella," *Nano Lett.*, vol. 9, no. 10, pp. 3663–3667, 2009.

[16] A. W. Mahoney, J. C. Sarrazin, E. Bamberg, and J. J. Abbott, "Velocity control with gravity compensation for magnetic helical microswimmers," *Adv. Robot.*, vol. 25, no. 8, pp. 1007–1028, 2011.

[17] K. M. Popek, A. W. Mahoney, and J. J. Abbott, "Localization method for a magnetic capsule endoscope propelled by a rotating magnetic dipole field," in *Proc. IEEE Int. Conf. Robot. Autom.*, 2013, pp. 5328–5333.

[18] A. W. Mahoney and J. J. Abbott, "Control of untethered magnetically actuated tools with localization uncertainty using a rotating permanent magnet," in *Proc. IEEE Int. Conf. Biomed. Robot. Biomechatron.*, 2012, pp. 1632–1637.

[19] A. W. Mahoney, N. D. Nelson, K. E. Peyer, B. J. Nelson, and J. J. Abbott, "Behavior of rotating magnetic microrobots above the step-out frequency with application to control of multi-microrobot systems," *Appl. Phys. Lett.*, vol. 104, no. 144101, pp. 31–34, 2014.

[20] K. Vollmers, D. R. Frutiger, B. E. Kratochvil, and B. J. Nelson, "Wireless resonant magnetic microactuator for untethered mobile microrobots," *Appl. Phys. Lett.*, vol. 92, no. 144103, pp. 1–3, 2008.

[21] D. R. Frutiger, K. Vollmers, B. E. Kratochvil, and B. J. Nelson, "Small, fast, and under control: wireless resonant magnetic micro-agents," *Int. J. Robot. Res.*, vol. 29, no. 5, pp. 613–636, 2010.

[22] C. Pawashe, S. Floyd, and M. Sitti, "Modeling and experimental characterization of an untethered magnetic micro-robot," *Int. J. Robot. Res.*, vol. 28, no. 8, pp. 1077–1094, 2009.

[23] A. W. Mahoney, N. D. Nelson, E. M. Parsons, and J. J. Abbott, "Non-ideal behaviors of magnetically driven screws in soft tissue," in *Proc. IEEE/RSJ Int. Conf. Intell. Robots Syst.*, 2012, pp. 3559–3564.

[24] K. Ishiyama, K. I. Arai, M. Sendoh, and A. Yamazaki, "Spiral-type micro-machine for medical applications," *J. Micromechatronics*, vol. 2, no. 1, pp. 77–86, 2003.

[25] L. Zhang, J. J. Abbott, L. X. Dong, B. E. Kratochvil, H. Zhang, K. E. Peyer, and B. J. Nelson, "Micromanipulation using artificial bacterial flagella," in *IEEE/RSJ Int. Conf. Intell. Robots Syst.*, 2009, pp. 1401–1406.

[26] K. E. Peyer, L. Zhang, and B. J. Nelson, "Localized non-contact manipulation using artificial bacterial flagella," *Appl. Phys. Lett.*, vol. 99, no. 174101, pp. 1–3, 2011.

[27] S. Tottori, L. Zhang, F. Qiu, K. K. Krawczyk, A. Franco-Obregón, and B. J. Nelson, "Magnetic helical micromachines: fabrication, controlled swimming, and cargo transport," *Adv. Mater.*, vol. 24, no. 6, pp. 811–816, 2012.

[28] E. Diller and M. Sitti, "Micro-scale mobile robotics," *Found. Trends Rob.*, vol. 2, no. 3, pp. 143–259, 2013.

CHAPTER 2

VELOCITY CONTROL WITH GRAVITY COMPENSATION FOR MAGNETIC HELICAL MICROSWIMMERS

The paper that follows was published in the special issue "Cordless Technology for Milli/Micro/Nano Robots" of the journal *Advanced Robotics* and is reprinted here with permission. The paper introduces a 6-DOF model of helical-microswimmer motion and applies it toward solving for the necessary rotation axis and rotation speed of the applied rotating magnet field to achieve a desired 3-DOF swimmer spatial velocity. In prior work, the magnetic field's rotation axis and speed was adjusted manually, making 3-DOF control over a microswimmer's velocity difficult, particularly since man-made swimmers tend to sink under their own weight and are generally observed from the top down using a microscope. The open-loop approach presented in this paper takes a desired 3-DOF swimmer spatial velocity from the user, which is a much more intuitive input than controlling field rotation axis and speed (even if there is error in the open-loop model).

A. W. Mahoney, J. C. Sarrazin, E. Bamberg, and J. J. Abbott, "Velocity Control with Gravity Compensation for Magnetic Helical Microswimmers," *Adv. Robot.*, vol. 25, no. 8, pp. 1007–1028, 2011.

Velocity Control with Gravity Compensation for Magnetic Helical Microswimmers

Arthur W. Mahoney [a,*], **John C. Sarrazin** [b], **Eberhard Bamberg** [b] **and Jake J. Abbott** [b]

[a] School of Computing, University of Utah, Salt Lake City, UT 84112, USA

[b] Department of Mechanical Engineering, University of Utah, Salt Lake City, UT 84112, USA

Received 25 June 2010; accepted 11 August 2011

Abstract

Magnetic helical microswimmers, which swim using a method inspired by the propulsion of bacterial flagella, are promising for use as untethered micromanipulators and as medical microrobots. Man-made devices are typically heavier than their fluid environment and consequently sink due to their own weight. To date, methods to compensate for gravitational effects have been *ad hoc*. In this paper, we present an open-loop algorithm for velocity control with gravity compensation for magnetic helical microswimmers that enables a human operator or automated controller to command desired velocity intuitively, rather than directly controlling the microswimmer's orientation and rotation speed. We provide experimental verification of the method.

Keywords

Microrobot, helix, screw, magnetic, wireless, untethered

1. Introduction

Untethered biomedical microrobots are a topic of considerable research. Microrobots have the potential to radically transform many medical procedures by operating in hard-to-reach locations of the body, performing tasks such as targeted therapy (e.g., drug delivery, hyperthermia), tissue removal (e.g., ablation) and remote sensing, and the bodies of the microrobots themselves may be used as maneuverable structures (e.g., stents, tissue scaffolding) [1]. Microrobots have also already been demonstrated as useful tools for untethered manipulation at the microscale, both on planar surfaces [2, 3] and in three-dimensional fluidic environments [4, 5]. Un-

* To whom correspondence should be addressed. E-mail: art.mahoney@utah.edu

 DOI:10.1163/016918611X568620

tethered microrobots stand to impact a broad range of fields, but we must first understand their locomotion and how to effectively control them wirelessly.

The environment in which a microrobot operates is significantly different than that of macroscale robots as we know them. In particular, microrobots typically operate in fluids at the low-Reynolds-number regime, where viscous drag significantly dominates over inertia [6]. In this environment, propulsion and actuation can be challenging, and although there are a number of ways for a microrobot to be wirelessly propelled, one method of particular interest is helical propulsion — a swimming method inspired by the propulsion of bacterial flagella — using torque produced from the rotation of an externally applied magnetic field [4, 7, 8]. It has been shown that magnetic helical swimming performs well compared to other methods of magnetic propulsion as the size of the microrobot scales down [9]. Microrobots that are propelled in this manner are typically simple devices consisting of a magnetic body rigidly attached to a chiral structure resembling a cork screw or wood screw. The community now has a good basic understanding of the ways in which magnetic helical microswimmers can be controlled and researchers have begun to tackle some of the non-idealities that manifest themselves during experimentation [10].

One such non-ideality is the microrobot sinking due to its own weight. Magnetic control of helical microswimmers has typically started from the assumption that the microswimmers behave similarly to bacteria, which are approximately neutrally buoyant, and the microswimmer is simply pointed in the direction of desired velocity, as depicted in Fig. 1a. When swimming under an optical microscope, the microswimmer typically lies near the horizontal plane, such that it can be easily observed and controlled. However, man-made microswimmers are typically heavier than their fluid medium and they sink down, albeit slowly, due to their own weight, resulting in a velocity that is not aligned with the thrust direction of the microswimmer (Fig. 1b and d), thus making the microswimmer attain a desired velocity is not as simple as merely pointing the microrobot in the desired direction. To counteract this downward drift and keep the microswimmer at a desired focal plane, researchers have pitched the microswimmer up in an *ad hoc* manner, as shown in Fig. 1c, with the goal of keeping the long axis of the microswimmer close to the horizontal plane such that observation through the microscope is relatively unchanged. In Ref. [4], for example, the authors report that their microswimmers require a compensation pitch of approximately 10°–20°, with the necessary pitch being inversely proportional to the microswimmer's rotation speed. As we will show herein, there is a unique combination of pitch angle and rotation speed (modulo 180° change in pitch) to achieve the desired velocity of the microswimmer, whether or not the desired velocity lies in the horizontal plane, and this combination of pitch angle and rotation speed is not intuitive to a human operator. In this paper, we describe a velocity-control-plus-gravity-compensation algorithm that calculates the correct pitch angle and rotation speed to achieve the commanded velocity with results like those shown in Fig. 1e, making teleoperation much more intuitive.

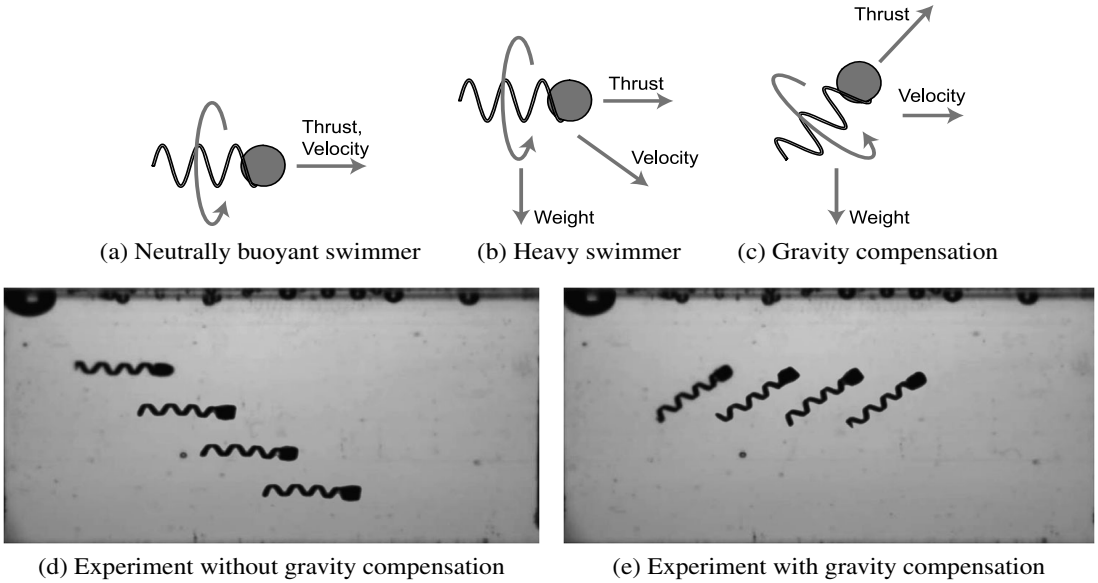

(a) Neutrally buoyant swimmer (b) Heavy swimmer (c) Gravity compensation

(d) Experiment without gravity compensation (e) Experiment with gravity compensation

Figure 1. (a) Natural flagellated bacteria are nearly neutrally buoyant. (b) Man-made swimmers are denser than water, causing them to drift downward under their weight. (c) To compensate for this drift, the microswimmer must be commanded to swim at a unique pitch angle and rotation speed. (d and e) Composite images from scaled experiments where the swimmer is commanded to move horizontally with a constant velocity, without and with the proposed gravity-compensation algorithm, demonstrating the behaviors described in (b) and (c), respectively. Gravity points downward in the images.

Considering the command input of magnetic helical microswimmer to be spatial velocity rather than manual control of pitch and rotation speed has not been done previously. It may be more appropriate to think of microswimmers as tiny helicopters as opposed to bacteria. Rather than the default configuration of the microswimmer being in the horizontal plane, it should be pointed vertically such that the thrust of the microswimmer is directly counteracting gravity. From this vertical configuration, the microrobot can move up or down simply by changing the rotation speed. To make lateral movements, the microswimmer pitches away from vertical, and again there is a unique combination of pitch angle and rotation speed to achieve the desired velocity.

To accurately command a velocity to our microswimmer that is not aligned with the microswimmer's central axis requires a model of the microswimmer that goes beyond the simple 2-d.o.f. model that has been used in prior work; in Section 2 we develop a full 6-d.o.f. model for helical microswimmers. In Section 3 we develop an algorithm that calculates the microswimmer orientation and rotation speed needed to achieve a desired spatial velocity. We experimentally verify the algorithm in Section 4, using a scaled magnetic swimmer propelled by the rotating uniform magnetic field of an electromagnetic system consisting of nested Helmholtz coils. Finally, in Section 5 we provide some additional discussion and interpretation of our algorithm and experimental results.

2. The 6-d.o.f. Helical Microswimmer Model

The swimming properties of magnetic helical microswimmers are well understood for motion along the microswimmer's central axis [6, 9, 11]. In a low-Reynolds-number regime, the applied nonfluidic torque and force, τ and f, acting along the microswimmer's central axis are linearly related to the translational velocity and angular velocity, v and ω, also along the microswimmer's central axis. This is expressed in the form of the widely used system of equations:

$$\begin{bmatrix} f \\ \tau \end{bmatrix} = \begin{bmatrix} a & b \\ b & c \end{bmatrix} \begin{bmatrix} v \\ \omega \end{bmatrix}, \tag{1}$$

where a, b and c are scalars that depend upon the geometry of the microswimmer and the properties of the fluid in which it swims. This 2-d.o.f. axial model has been used with good success to study the feasibility of helical swimming [9, 11] and to characterize basic swimming properties [12]; however, it does not provide sufficient information to understand how a helical microswimmer behaves in full 6-d.o.f. motion.

In this section, we extend (1) from 2 to 6 d.o.f. using resistive force theory (RFT) and spatial transformations, including effects caused by rigidly fixing a spherical magnetic head to the end of a helix. Making the assumption that the fluidic forces acting on the helix and the head are independent from each other, we first determine the fluidic force and torque acting purely on the helix, $\mathbf{f}_{\mathrm{h}}$ and $\boldsymbol{\tau}_{\mathrm{h}}$, using RFT, and then the fluidic force and torque acting solely on the spherical magnet head, $\mathbf{f}_{\mathrm{m}}$ and $\boldsymbol{\tau}_{\mathrm{m}}$ (this assumption has been used in other work to obtain a good approximations of the fluidic properties of rigid helices in the low Reynolds regime [9, 13]). Thus, the total force and torque acting on the microswimmer is the sum of the forces and torques acting on the helix and the spherical head: $\mathbf{f} = \mathbf{f}_{\mathrm{h}} + \mathbf{f}_{\mathrm{m}}$ and $\boldsymbol{\tau} = \boldsymbol{\tau}_{\mathrm{h}} + \boldsymbol{\tau}_{\mathrm{m}}$, respectively. Although we only consider helices of right-handed chirality, the results derived in this section can be obtained for left-handed helices using the same methods. A similar 6-d.o.f. model was presented in Ref. [13] for the study of cellular flagella motility where the helical flagella rotates opposite the direction of the cell body.

RFT is a simple approach used to determine the forces caused by velocity on an infinitesimally small length of helix [14, 15]. RFT takes the velocity $\mathbf{v}_s$ of one of these small segments of the helix, decomposes the velocity into components parallel and perpendicular to the segment, and relates them to parallel and perpendicular drag forces acting on the segment with the differential forces:

$$\mathrm{d}\mathbf{f}_{\perp s} = \xi_{\perp} \mathbf{v}_{\perp s} \, \mathrm{d}s \tag{2}$$

$$\mathrm{d}\mathbf{f}_{\parallel s} = \xi_{\parallel} \mathbf{v}_{\parallel s} \, \mathrm{d}s, \tag{3}$$

where $\xi_{\perp}$ and $\xi_{\parallel}$ are scalar drag coefficients, which have a number of empirical approximations (e.g., Ref. [15]). Integrating these differential forces along the length of the helix provides the fluidic forces acting on the helix ($\mathbf{f}_{\mathrm{h}}$) induced by a spe-

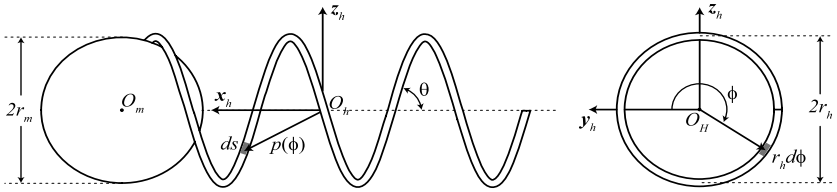

Figure 2. A helical microswimmer consisting of spherical magnetic body of radius r_{m} attached to a right-handed helix with pitch θ and radius r_{h}. The coordinate frame of the microswimmer's helix (denoted by h) is oriented with $\mathbf{x}_{\mathrm{h}}$ along the central axis of the helix with the origin $\mathbf{O}_{\mathrm{h}}$ of the right-handed coordinate system at the center of the helix.

cific movement of the helix. To perform this integration in three dimensions, we first need to define the coordinate frames for the helix and for a given differential segment. Let the geometry of the helix be defined with pitch θ and radius r_{h}, and let the helix coordinate frame (denoted by h) lie with the $\mathbf{x}_{\mathrm{h}}$ axis parallel to the central axis of the helix, and the $\mathbf{y}_{\mathrm{h}}$ and $\mathbf{z}_{\mathrm{h}}$ axis be arranged as in Fig. 2. The origin of this coordinate system is located at the center of the helix, denoted by $\mathbf{O}_{\mathrm{h}}$. For ease of integration, we will describe the helix using a cylindrical coordinate system parameterized by the polar angle ϕ. The matrix that will rotate vectors written in a given segment coordinate frame (denoted by s) to the helix frame is ${}^{\mathrm{h}}\mathbf{R}_{\mathrm{s}}(\phi) = \mathbf{R}_x(\phi)\mathbf{R}_y(-\theta)$, where ${}^{\mathrm{h}}\mathbf{R}_{\mathrm{s}} \in SO(3)$ denotes a rotation matrix from frame s to frame h, and $\mathbf{R}_x(\phi) \in SO(3)$ denotes a rotation matrix about axis $\mathbf{x}$ by ϕ rad [16]. We can write the vector from $\mathbf{O}_{\mathrm{h}}$ to the origin of each segment frame with respect to ϕ in the form:

$$ {}^{\mathrm{h}}\mathbf{p}(\phi) = \begin{bmatrix} \dfrac{r\phi}{\tan(\theta)} & r\cos(\phi) & r\sin(\phi) \end{bmatrix}^{\mathrm{T}}, \tag{4} $$

where ${}^{\mathrm{h}}\mathbf{p}$ denotes the vector $\mathbf{p}$ represented in frame h. At each of these points, the $\mathbf{x}_{\mathrm{s}}$ axis of the segment frame lies parallel to the helix segment, and both $\mathbf{y}_{\mathrm{s}}$ and $\mathbf{z}_{\mathrm{s}}$ lie perpendicular to the helix segment, with $\mathbf{y}_{\mathrm{s}}$ pointing radially away from the central axis of the microswimmer's helix. This leads us to express the differential relating velocity to force in three dimensions with respect to the frame of an arbitrary segment along the helix in the segment frame as:

$$ {}^{\mathrm{s}}\mathrm{d}\mathbf{f}_s = {}^{\mathrm{s}}\boldsymbol{\Xi}\,{}^{\mathrm{s}}\mathbf{v}_s\,\mathrm{d}s, \tag{5} $$

where:

$$ {}^{\mathrm{s}}\boldsymbol{\Xi} = \begin{bmatrix} \xi_{\parallel} & 0 & 0 \\ 0 & \xi_{\perp} & 0 \\ 0 & 0 & \xi_{\perp} \end{bmatrix}, \tag{6} $$

and ${}^{\mathrm{s}}\mathbf{f}_s$ and ${}^{\mathrm{s}}\mathbf{v}_s$ are the force and velocity of the segment expressed in the segment's own frame. The relationship between velocity and forces in the segment frame can be expressed in the helix frame as:

$$ {}^{\mathrm{h}}\mathrm{d}\mathbf{f}_s = {}^{\mathrm{h}}\boldsymbol{\Xi}(\phi)\,{}^{\mathrm{h}}\mathbf{v}_s\,\mathrm{d}s, \tag{7} $$

where:

$$^{\mathrm{h}}\boldsymbol{\Xi}(\phi) = {}^{\mathrm{h}}\mathbf{R}_{\mathrm{s}}(\phi)\,{}^{\mathrm{s}}\boldsymbol{\Xi}\,{}^{\mathrm{s}}\mathbf{R}_{\mathrm{h}}(\phi). \tag{8}$$

As the helix is swimming, the velocity $\mathbf{v}_s$ of an infinitesimally small segment of helix (parameterized by ϕ with position described by $\mathbf{p}(\phi)$) can be decomposed into the sum of the microswimmer's translational velocity $\mathbf{v}$ and the velocity caused by an arbitrary helix rotation $\boldsymbol{\omega}$:

$$\mathbf{v}_s = \mathbf{v} + \boldsymbol{\omega} \times \mathbf{p}(\phi) = \mathbf{v} - \mathbf{p}(\phi) \times \boldsymbol{\omega}. \tag{9}$$

This can be expressed in the helix frame as:

$$^{\mathrm{h}}\mathbf{v}_s = {}^{\mathrm{h}}\mathbf{v} - \mathbb{S}\{{}^{\mathrm{h}}\mathbf{p}(\phi)\}\,{}^{\mathrm{h}}\boldsymbol{\omega} = {}^{\mathrm{h}}\mathbf{v} + \mathbb{S}\{{}^{\mathrm{h}}\mathbf{p}(\phi)\}^{\mathrm{Th}}\boldsymbol{\omega}, \tag{10}$$

where $\mathbb{S}\{\mathbf{k}\}$ packs the vector $\mathbf{k} = [k_1 \quad k_2 \quad k_3]^{\mathrm{T}}$ into the skew-symmetric matrix, representing the cross-product operation:

$$\mathbb{S}\{\mathbf{k}\} = \begin{bmatrix} 0 & -k_3 & k_2 \\ k_3 & 0 & -k_1 \\ -k_2 & k_1 & 0 \end{bmatrix}. \tag{11}$$

Substituting (10) into (7) results in:

$$^{\mathrm{h}}\mathrm{d}\mathbf{f}_s = {}^{\mathrm{h}}\boldsymbol{\Xi}(\phi)\,{}^{\mathrm{h}}\mathbf{v}\,\mathrm{d}s + {}^{\mathrm{h}}\boldsymbol{\Xi}(\phi)\mathbb{S}\{{}^{\mathrm{h}}\mathbf{p}(\phi)\}^{\mathrm{Th}}\boldsymbol{\omega}\,\mathrm{d}s. \tag{12}$$

A similar differential expression relating fluidic torque to translational and angular velocities of the helix can also be derived. Each force acting on an infinitesimally small segment of helix induces a subsequent torque about the helix origin. The relationship between the torque and force at an arbitrary helix segment, parameterized by ϕ, can be expressed in the helix frame as:

$$^{\mathrm{h}}\mathrm{d}\boldsymbol{\tau}_s = {}^{\mathrm{h}}\mathbf{p}(\phi) \times {}^{\mathrm{h}}\mathrm{d}\mathbf{f}_s = \mathbb{S}\{{}^{\mathrm{h}}\mathbf{p}(\phi)\}\,{}^{\mathrm{h}}\,\mathrm{d}\mathbf{f}_s. \tag{13}$$

Here, we make an assumption that is common when using RFT: that the drag torque on the helix due to a given segment is due to the translational velocity of the segment as it slices through the fluid and that the torque due to the small segment's rotation is negligible. This assumption significantly simplifies calculations and should be valid provided that the cross-section of the segment is small compared to the overall radius of the helix.

The total fluidic force and torque on the helix are found by integrating the forces and torques on the segments along the total length of the helix:

$$\mathbf{f}_{\mathrm{h}} = \int \mathrm{d}\mathbf{f}_s, \qquad \boldsymbol{\tau}_{\mathrm{h}} = \int \mathrm{d}\boldsymbol{\tau}_s. \tag{14}$$

For both (12) and (13) the helix was parameterized using the polar angle ϕ. Therefore, the force and torque will be obtained by integrating both differentials with respect to ϕ. Substituting (12) into (13), replacing $\mathrm{d}s$ with $r_{\mathrm{h}}\,\mathrm{d}\phi/\sin(\theta)$ and integrating ϕ from $-\pi n$ to πn produces two integral equations for an n-turn helix

centered at $\mathbf{O}_{\mathrm{h}}$:

$$
\begin{aligned}
{}^{\mathrm{h}}\mathbf{f}_{\mathrm{h}} &= \left(\frac{r_{\mathrm{h}}}{\sin(\theta)}\int_{-\pi n}^{\pi n} {}^{\mathrm{h}}\boldsymbol{\Xi}(\phi)\,\mathrm{d}\phi\right){}^{\mathrm{h}}\mathbf{v} \\
&\quad + \left(\frac{r_{\mathrm{h}}}{\sin(\theta)}\int_{-\pi n}^{\pi n} {}^{\mathrm{h}}\boldsymbol{\Xi}(\phi)\mathbb{S}\{{}^{\mathrm{h}}\mathbf{p}(\phi)\}^{\mathrm{T}}\,\mathrm{d}\phi\right){}^{\mathrm{h}}\boldsymbol{\omega} \qquad (15)\\
{}^{\mathrm{h}}\boldsymbol{\tau}_{\mathrm{h}} &= \left(\frac{r_{\mathrm{h}}}{\sin(\theta)}\int_{-\pi n}^{\pi n} \mathbb{S}\{{}^{\mathrm{h}}\mathbf{p}(\phi)\}{}^{\mathrm{h}}\boldsymbol{\Xi}(\phi)\,\mathrm{d}\phi\right){}^{\mathrm{h}}\mathbf{v} \\
&\quad + \left(\frac{r_{\mathrm{h}}}{\sin(\theta)}\int_{-\pi n}^{\pi n} \mathbb{S}\{{}^{\mathrm{h}}\mathbf{p}(\phi)\}{}^{\mathrm{h}}\boldsymbol{\Xi}(\phi)\mathbb{S}\{{}^{\mathrm{h}}\mathbf{p}(\phi)\}^{\mathrm{T}}\,\mathrm{d}\phi\right){}^{\mathrm{h}}\boldsymbol{\omega}. \qquad (16)
\end{aligned}
$$

Evaluating all four matrix integrals results in two equations relating force and torque to translational velocity and angular velocity around $\mathbf{O}_{\mathrm{h}}$:

$$
\begin{bmatrix} {}^{\mathrm{h}}\mathbf{f}_{\mathrm{h}} \\ {}^{\mathrm{h}}\boldsymbol{\tau}_{\mathrm{h}} \end{bmatrix} = \begin{bmatrix} {}^{\mathrm{h}}\mathbf{A}_{\mathrm{h}} & {}^{\mathrm{h}}\mathbf{B}_{\mathrm{h}} \\ {}^{\mathrm{h}}\mathbf{B}_{\mathrm{h}}^{\mathrm{T}} & {}^{\mathrm{h}}\mathbf{C}_{\mathrm{h}} \end{bmatrix} \begin{bmatrix} {}^{\mathrm{h}}\mathbf{v} \\ {}^{\mathrm{h}}\boldsymbol{\omega} \end{bmatrix}, \qquad (17)
$$

where:

$$
\begin{aligned}
{}^{\mathrm{h}}\mathbf{A}_{\mathrm{h}} &= \begin{bmatrix} a_{\mathrm{h}11} & 0 & 0 \\ 0 & a_{\mathrm{h}22} & 0 \\ 0 & 0 & a_{\mathrm{h}22} \end{bmatrix}, \qquad {}^{\mathrm{h}}\mathbf{B}_{\mathrm{h}} = \begin{bmatrix} b_{\mathrm{h}11} & 0 & b_{\mathrm{h}13} \\ 0 & b_{\mathrm{h}22} & 0 \\ 0 & 0 & b_{\mathrm{h}33} \end{bmatrix} \\
{}^{\mathrm{h}}\mathbf{C}_{\mathrm{h}} &= \begin{bmatrix} c_{\mathrm{h}11} & 0 & c_{\mathrm{h}13} \\ 0 & c_{\mathrm{h}22} & 0 \\ c_{\mathrm{h}13} & 0 & c_{\mathrm{h}33} \end{bmatrix},
\end{aligned} \qquad (18)
$$

and:

$$
a_{\mathrm{h}11} = \frac{2\pi n r_{\mathrm{h}}(\xi_{\parallel}\cos^2(\theta) + \xi_{\perp}\sin^2(\theta))}{\sin(\theta)} \qquad (19)
$$

$$
a_{\mathrm{h}22} = \frac{\pi n r_{\mathrm{h}}(\xi_{\perp} + \xi_{\perp}\cos^2(\theta) + \xi_{\parallel}\sin^2(\theta))}{\sin(\theta)} \qquad (20)
$$

$$
b_{\mathrm{h}11} = 2\pi n r_{\mathrm{h}}^2(\xi_{\parallel} - \xi_{\perp})\cos(\theta) \qquad (21)
$$

$$
b_{\mathrm{h}13} = \frac{-2\pi n r_{\mathrm{h}}^2(\xi_{\parallel} - \xi_{\perp})\cos(\theta)}{\tan(\theta)} \qquad (22)
$$

$$
b_{\mathrm{h}22} = \frac{-3\pi n r_{\mathrm{h}}^2(\xi_{\parallel} - \xi_{\perp})\cos(\theta)}{2} \qquad (23)
$$

$$
b_{\mathrm{h}33} = \frac{-\pi n r_{\mathrm{h}}^2(\xi_{\parallel} - \xi_{\perp})\cos(\theta)}{2} \qquad (24)
$$

$$
c_{\mathrm{h}11} = \frac{2\pi n r_{\mathrm{h}}^3(\xi_{\perp}\cos^2(\theta) + \xi_{\parallel}\sin^2(\theta))}{\sin(\theta)} \qquad (25)
$$

$$
c_{\mathrm{h}13} = \frac{-2\pi n r_{\mathrm{h}}^3(\xi_{\perp}\cos^2(\theta) + \xi_{\parallel}\sin^2(\theta))}{\sin(\theta)\tan(\theta)} \qquad (26)
$$

$$c_{\mathrm{h}22} = \frac{2\pi n r_{\mathrm{h}}^3(\xi_{\parallel}\cos^2(\theta) + \xi_{\perp}\sin^2(\theta) - \xi_{\perp}/2)}{\sin(\theta)} + \frac{\pi n r_{\mathrm{h}}^3(\xi_{\parallel}\cos^2(\theta) - \xi_{\perp}\sin^2(\theta) - \xi_{\perp})}{2\tan^2(\theta)\sin(\theta)} \tag{27}$$

$$+ \frac{(\pi n r_{\mathrm{h}})^3(\xi_{\parallel}\cos^2(\theta) - \xi_{\perp}\sin^2(\theta) + \xi_{\perp})}{3\tan^2(\theta)\sin(\theta)} \tag{28}$$

$$c_{\mathrm{h}33} = \frac{\pi n r_{\mathrm{h}}^3 \xi_{\perp}}{\sin(\theta)} - \frac{\pi n r_{\mathrm{h}}^3(\xi_{\perp}\cos^2(\theta) + \xi_{\parallel}\sin^2(\theta) - \xi_{\perp})}{2\tan^2(\theta)\sin(\theta)} \tag{29}$$

$$+ \frac{(\pi n r_{\mathrm{h}})^3(\xi_{\perp}\cos^2(\theta) + \xi_{\parallel}\sin^2(\theta) + \xi_{\perp})}{3\tan^2(\theta)\sin(\theta)}. \tag{30}$$

As the microswimmer rotates about $\mathbf{O}_{\mathrm{h}}$, the spherical magnetic head of radius r_{m} fixed to the helix exerts fluidic forces and torques on the microswimmer that we assume to be independent from those caused by the helix. Let $\mathbf{k}$ be the vector from the center of the helix $\mathbf{O}_{\mathrm{h}}$ to the center of the magnetic head $\mathbf{O}_{\mathrm{m}}$ as shown in Fig. 2. Given that the translational and rotational drag coefficients in Stokes flow of viscosity η are $\xi_{v\mathrm{m}} = 6\pi\eta r_{\mathrm{m}}$ and $\xi_{\omega\mathrm{m}} = 8\pi\eta r_m^3$, respectively [17], the drag force acting on the head is the product of the translational drag coefficient and the head's velocity. Arbitrary movement of the microswimmer produces a magnet velocity, expressed in the helix frame, of

$${}^{\mathrm{h}}\mathbf{v}_{\mathrm{m}} = {}^{\mathrm{h}}\mathbf{v} + {}^{\mathrm{h}}\boldsymbol{\omega} \times {}^{\mathrm{h}}\mathbf{k} = {}^{\mathrm{h}}\mathbf{v} - {}^{\mathrm{h}}\mathbf{k} \times {}^{\mathrm{h}}\boldsymbol{\omega} = {}^{\mathrm{h}}\mathbf{v} + \mathbb{S}\{{}^{\mathrm{h}}\mathbf{k}\}^{\mathrm{T}\,\mathrm{h}}\boldsymbol{\omega}, \tag{31}$$

which corresponds to a force on the magnet:

$${}^{\mathrm{h}}\mathbf{f}_{\mathrm{m}} = \xi_{v\mathrm{m}}{}^{\mathrm{h}}\mathbf{v} + \xi_{v\mathrm{m}}\mathbb{S}\{{}^{\mathrm{h}}\mathbf{k}\}^{\mathrm{T}\,\mathrm{h}}\boldsymbol{\omega}. \tag{32}$$

The drag torque caused by the spherical head is a result of the force acting at the moment arm $\mathbf{k}$ as well as the drag caused by the rotation of the head itself. This can be expressed in the form ${}^{\mathrm{h}}\boldsymbol{\tau}_{\mathrm{m}} = {}^{\mathrm{h}}\mathbf{k} \times {}^{\mathrm{h}}\mathbf{f}_{\mathrm{m}} + \xi_{\omega\mathrm{m}}{}^{\mathrm{h}}\boldsymbol{\omega}$, with ${}^{\mathrm{h}}\mathbf{f}_{\mathrm{m}}$ from (32). Replacing the cross-product operator with its corresponding skew-symmetric matrix and grouping like terms produces:

$${}^{\mathrm{h}}\boldsymbol{\tau}_{\mathrm{m}} = \xi_{v\mathrm{m}}\mathbb{S}\{{}^{\mathrm{h}}\mathbf{k}\}{}^{\mathrm{h}}\mathbf{v} + \left(\xi_{v\mathrm{m}}\mathbb{S}\{{}^{\mathrm{h}}\mathbf{k}\}\mathbb{S}\{{}^{\mathrm{h}}\mathbf{k}\}^{\mathrm{T}} + \xi_{\omega\mathrm{m}}\mathbf{I}\right){}^{\mathrm{h}}\boldsymbol{\omega}, \tag{33}$$

where $\mathbf{I}$ is the identity matrix. If we let the matrices:

$$\begin{aligned} {}^{\mathrm{h}}\mathbf{A}_{\mathrm{m}} &= \xi_{v\mathrm{m}}\mathbf{I}, \qquad {}^{\mathrm{h}}\mathbf{B}_{\mathrm{m}} = \xi_{v\mathrm{m}}\mathbb{S}\{{}^{\mathrm{h}}\mathbf{k}\}^{\mathrm{T}} \\ {}^{\mathrm{h}}\mathbf{C}_{\mathrm{m}} &= \xi_{v\mathrm{m}}\mathbb{S}\{{}^{\mathrm{h}}\mathbf{k}\}\mathbb{S}\{{}^{\mathrm{h}}\mathbf{k}\}^{\mathrm{T}} + \xi_{\omega\mathrm{m}}\mathbf{I}, \end{aligned} \tag{34}$$

then the total force ${}^{\mathrm{h}}\mathbf{f} = {}^{\mathrm{h}}\mathbf{f}_{\mathrm{h}} + {}^{\mathrm{h}}\mathbf{f}_{\mathrm{m}}$ and torque ${}^{\mathrm{h}}\boldsymbol{\tau} = {}^{\mathrm{h}}\boldsymbol{\tau}_{\mathrm{h}} + {}^{\mathrm{h}}\boldsymbol{\tau}_{\mathrm{m}}$ acting on the microswimmer are:

$$\begin{bmatrix} {}^{\mathrm{h}}\mathbf{f} \\ {}^{\mathrm{h}}\boldsymbol{\tau} \end{bmatrix} = \begin{bmatrix} {}^{\mathrm{h}}\mathbf{A} & {}^{\mathrm{h}}\mathbf{B} \\ {}^{\mathrm{h}}\mathbf{B}^{\mathrm{T}} & {}^{\mathrm{h}}\mathbf{C} \end{bmatrix} \begin{bmatrix} {}^{\mathrm{h}}\mathbf{v} \\ {}^{\mathrm{h}}\boldsymbol{\omega} \end{bmatrix}, \tag{35}$$

where ${}^{\mathrm{h}}\mathbf{A} = {}^{\mathrm{h}}\mathbf{A}_{\mathrm{h}} + {}^{\mathrm{h}}\mathbf{A}_{\mathrm{m}}$, ${}^{\mathrm{h}}\mathbf{B} = {}^{\mathrm{h}}\mathbf{B}_{\mathrm{h}} + {}^{\mathrm{h}}\mathbf{B}_{\mathrm{m}}$ and ${}^{\mathrm{h}}\mathbf{C} = {}^{\mathrm{h}}\mathbf{C}_{\mathrm{h}} + {}^{\mathrm{h}}\mathbf{C}_{\mathrm{m}}$:

$$ {}^{\mathrm{h}}\mathbf{A} = \begin{bmatrix} a_{11} & 0 & 0 \\ 0 & a_{22} & 0 \\ 0 & 0 & a_{22} \end{bmatrix} = \begin{bmatrix} a_{\mathrm{h}11} + \xi_{v\mathrm{m}} & 0 & 0 \\ 0 & a_{\mathrm{h}22} + \xi_{v\mathrm{m}} & 0 \\ 0 & 0 & a_{\mathrm{h}22} + \xi_{v\mathrm{m}} \end{bmatrix} \tag{36} $$

$$ {}^{\mathrm{h}}\mathbf{B} = \begin{bmatrix} b_{11} & 0 & b_{13} \\ 0 & b_{22} & b_{23} \\ 0 & -b_{23} & b_{33} \end{bmatrix} = \begin{bmatrix} b_{\mathrm{h}11} & 0 & b_{\mathrm{h}13} \\ 0 & b_{\mathrm{h}22} & \xi_{v\mathrm{m}}|\mathbf{k}| \\ 0 & -\xi_{v\mathrm{m}}|\mathbf{k}| & b_{\mathrm{h}33} \end{bmatrix} \tag{37} $$

$$ \begin{aligned} {}^{\mathrm{h}}\mathbf{C} &= \begin{bmatrix} c_{11} & 0 & c_{13} \\ 0 & c_{22} & 0 \\ c_{13} & 0 & c_{33} \end{bmatrix} \\ &= \begin{bmatrix} c_{\mathrm{h}11} + \xi_{\omega\mathrm{m}} & 0 & c_{\mathrm{h}13} \\ 0 & c_{\mathrm{h}22} + \xi_{v\mathrm{m}}|\mathbf{k}|^2 + \xi_{\omega\mathrm{m}} & 0 \\ c_{\mathrm{h}13} & 0 & c_{\mathrm{h}33} + \xi_{v\mathrm{m}}|\mathbf{k}|^2 + \xi_{\omega\mathrm{m}} \end{bmatrix}. \end{aligned} \tag{38} $$

Equation (35) is the 6 d.o.f. equivalent of (1). Note that $\mathbf{f}$ and $\boldsymbol{\tau}$ do not represent viscous drag associated with the microswimmer's total velocity $\mathbf{v}$ and $\boldsymbol{\omega}$. Rather, they represent non-fluidic force and torque — in this paper, force due to gravity and torque due to magnetism — corresponding to a given microswimmer velocity (i.e., the force and torque required to overcome viscous drag for a given microswimmer velocity). Now that we are equipped with a 6-d.o.f. helical microswimmer model, we are ready to develop the control algorithm that enables intuitive control over the microswimmer's velocity, as opposed to directly controlling the microswimmer's orientation and rotation speed.

3. Algorithm for Velocity Control with Gravity Compensation

To compensate for the drift caused by an applied force on the microswimmer, it is necessary to find the direction that it must point, $\mathbf{x}_{\mathrm{h}}$, and at what speed it must rotate, Ω, to achieve a desired spatial velocity, ${}^{\mathrm{w}}\mathbf{v}$, where w indicates the stationary world frame. In this paper, the microswimmer's weight is the sole applied non-fluidic force, represented by a vector $m\mathbf{g}$, where m is the mass of the microswimmer and $\mathbf{g}$ is the acceleration of gravity, and the 'downward' direction is defined with the unit vector $\hat{\mathbf{g}} = \mathbf{g}/\|\mathbf{g}\|$. As can be seen from the off-diagonal terms in the ${}^{\mathrm{h}}\mathbf{B}$ and ${}^{\mathrm{h}}\mathbf{C}$ matrices of Section 2, the result of steering the microswimmer (i.e., rotating the swimmer around the $\mathbf{y}_{\mathrm{h}}$ or $\mathbf{z}_{\mathrm{h}}$ axis) can produce complex forces and torques acting on the microswimmer aside from those produced by weight. Despite this fact, previous research has shown that magnetic helical microswimmers can be turned effectively by adjusting the axis around which the applied magnetic field rotates [4, 12]. Although there is evidence that commanding steering maneuvers that are too rapid can lead to loss of control, we make the assumption herein that the microswimmer can be turned continuously to a desired pitch angle away from vertical fast enough such that the microswimmer's transient behavior is negligible.

In this section, we present a steady-state solution to the velocity problem, and use it to produce a control algorithm that takes a desired velocity as its input and outputs

the direction the microswimmer must be pointed and how fast it must be rotating to attain the desired velocity at steady state. We denote the pointing direction by $\tilde{\mathbf{x}}$ and the rotation speed by Ω. In the context of command inputs using magnetic fields, $\tilde{\mathbf{x}}$ is also the axis around which the magnetic field should rotate, such that the magnetic field is always perpendicular to $\tilde{\mathbf{x}}$ and Ω is the rate of rotation.

If the stationary world frame is aligned with the microswimmer's workspace in an intuitive manner, the control inputs would best be expressed in this frame. To avoid requiring vectors to be converted back and forth between the world frame and the microswimmer's coordinate frame (i.e., frame h, which rotates), any equations used to generate the necessary pitch and angular velocity would also best be represented in the world frame. From the 6-d.o.f. model derived in Section 2, the portion of (35) that is of particular interested to us is:

$$^{\mathrm{h}}\mathbf{f} = {}^{\mathrm{h}}\mathbf{A}\,{}^{\mathrm{h}}\mathbf{v} + {}^{\mathrm{h}}\mathbf{B}\,{}^{\mathrm{h}}\boldsymbol{\omega}, \tag{39}$$

which relates the microswimmer's velocity to applied non-fluidic forces and angular velocity of the microswimmer. As $^{\mathrm{h}}\mathbf{A}$ is clearly invertible, the desired velocity can be solved for in (39) to produce:

$$^{\mathrm{h}}\mathbf{v} = (^{\mathrm{h}}\mathbf{A}^{-1})\,{}^{\mathrm{h}}\mathbf{f} + (-{}^{\mathrm{h}}\mathbf{A}^{-1}\,{}^{\mathrm{h}}\mathbf{B})\,{}^{\mathrm{h}}\boldsymbol{\omega} = {}^{\mathrm{h}}\mathbf{D}\,{}^{\mathrm{h}}\mathbf{f} + {}^{\mathrm{h}}\mathbf{E}\,{}^{\mathrm{h}}\boldsymbol{\omega}, \tag{40}$$

where:

$$^{\mathrm{h}}\mathbf{D} = \begin{bmatrix} d_{11} & 0 & 0 \\ 0 & d_{22} & 0 \\ 0 & 0 & d_{22} \end{bmatrix}, \qquad {}^{\mathrm{h}}\mathbf{E} = \begin{bmatrix} e_{11} & 0 & e_{13} \\ 0 & e_{22} & e_{23} \\ 0 & -e_{23} & e_{33} \end{bmatrix}, \tag{41}$$

all expressed in the microswimmer's helix frame. Using $^{\mathrm{w}}\mathbf{R}_{\mathrm{h}}$, (40) can be written in the world frame:

$$^{\mathrm{w}}\mathbf{v} = {}^{\mathrm{w}}\mathbf{D}\,{}^{\mathrm{w}}\mathbf{f} + {}^{\mathrm{w}}\mathbf{E}\,{}^{\mathrm{w}}\boldsymbol{\omega}, \tag{42}$$

using similarity transformations:

$$\begin{aligned} {}^{\mathrm{w}}\mathbf{v} &= {}^{\mathrm{w}}\mathbf{R}_{\mathrm{h}}\,{}^{\mathrm{h}}\mathbf{v}, & {}^{\mathrm{w}}\mathbf{f} &= {}^{\mathrm{w}}\mathbf{R}_{\mathrm{h}}\,{}^{\mathrm{h}}\mathbf{f} \\ {}^{\mathrm{w}}\mathbf{D} &= {}^{\mathrm{w}}\mathbf{R}_{\mathrm{h}}\,{}^{\mathrm{h}}\mathbf{D}\,{}^{\mathrm{h}}\mathbf{R}_{\mathrm{w}}, & {}^{\mathrm{w}}\mathbf{E} &= {}^{\mathrm{w}}\mathbf{R}_{\mathrm{h}}\,{}^{\mathrm{h}}\mathbf{E}\,{}^{\mathrm{h}}\mathbf{R}_{\mathrm{w}}. \end{aligned} \tag{43}$$

Constructing $^{\mathrm{h}}\mathbf{R}_{\mathrm{w}}$ requires the orientation of the robot as it rotates to be detected. In practice, it is difficult to sense the orientation of the robot about its central axis as it rotates during propulsion (e.g., using computer vision). To make best use of (42) for anything aside from the trivial cases where the microswimmer is being commanded to move vertically, we will express (42) in a manner that does not require the orientation of the microswimmer about its central axis to be known.

Since weight is the sole non-fluidic force acting upon the microrobot, the input force $\mathbf{f}$ to (39) is $m\mathbf{g}$. The desired velocity, $\mathbf{v}$, can be broken into vertical and horizontal components, respectively:

$$\mathbf{v}_{\mathrm{ver}} = (\mathbf{v} \cdot \hat{\mathbf{g}})\hat{\mathbf{g}} \tag{44}$$

$$\mathbf{v}_{\mathrm{hor}} = \mathbf{v} - \mathbf{v}_{\mathrm{ver}}. \tag{45}$$

If $\|\mathbf{v}_{\text{hor}}\| = 0$, then the microswimmer is being commanded to move vertically: either straight up, straight down or a stationary hover. This is the trivial case where (39) effectively becomes equivalent to its 2-d.o.f. counterpart from (1), making the solution for $\tilde{\mathbf{x}}$ and Ω straightforward:

$$\tilde{\mathbf{x}} = -\hat{\mathbf{g}} \tag{46}$$

$$\Omega = \frac{\|\mathbf{v}\| + d_{11}\|\mathbf{f}\|}{e_{11}}. \tag{47}$$

If $\|\mathbf{v}_{\text{hor}}\| \neq 0$, the solution is more complicated. Using $\hat{\mathbf{g}}$, we will construct a new coordinate frame associated with the microswimmer that does not rotate when the microswimmer rotates about its central axis and we will express (42) in this frame. This coordinate system (denoted by p) will be constructed such that the basis vectors are eigenvectors of ${}^{\text{w}}\mathbf{D}$ or ${}^{\text{w}}\mathbf{E}$. As the eigenvectors of ${}^{\text{w}}\mathbf{D}$ or ${}^{\text{w}}\mathbf{E}$ are aligned with the principle directions of the microswimmer, we will refer to this frame as the 'principle' coordinate frame. Let the basis of this coordinate frame be defined as:

$$\mathbf{x}_{\text{p}} = \frac{(\mathbf{x}_{\text{h}} \cdot \mathbf{v})\mathbf{x}_{\text{h}}}{|\mathbf{x}_{\text{h}} \cdot \mathbf{v}|} \tag{48}$$

$$\mathbf{y}_{\text{p}} = \frac{\mathbf{x}_{\text{p}} \times \mathbf{g}}{\|\mathbf{x}_{\text{p}} \times \mathbf{g}\|} \tag{49}$$

$$\mathbf{z}_{\text{p}} = \mathbf{x}_{\text{p}} \times \mathbf{y}_{\text{p}}. \tag{50}$$

The principle frame is depicted in Fig. 3a. Expressing (42) in the principle coordinate frame transforms the problem of finding the necessary pitch and angular velocity into one that is relatively easy to solve and, as will be seen, is invariant to rotations of the microswimmer about its central axis. The representation of (42) in terms of the principle frame can be found by determining the representation of its terms, ${}^{\text{w}}\mathbf{D}{}^{\text{w}}\mathbf{f}$ and ${}^{\text{w}}\mathbf{E}{}^{\text{w}}\boldsymbol{\omega}$, individually.

If we make the assumption that the swimmer is at steady state as discussed earlier, then we know ${}^{\text{w}}\boldsymbol{\omega} = \Omega{}^{\text{w}}\tilde{\mathbf{x}} = \Omega{}^{\text{w}}\mathbf{x}_{\text{p}}$ and ${}^{\text{w}}\mathbf{x}_{\text{p}}$ is parallel to ${}^{\text{w}}\mathbf{x}_{\text{h}}$ (i.e., ${}^{\text{w}}\mathbf{x}_{\text{p}} = {}^{\text{w}}\mathbf{x}_{\text{h}}$ or

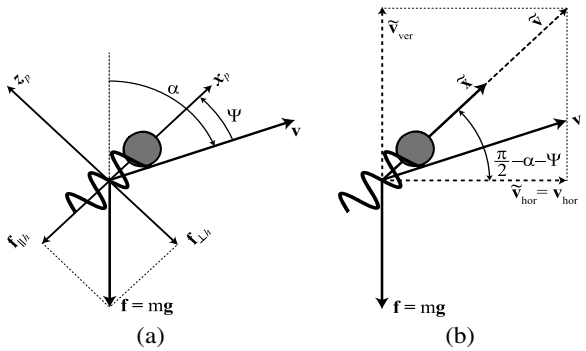

Figure 3. (a) Definition of the principle frame, angles and forces. (b) Construction of $\tilde{\mathbf{x}}$.

${}^{\mathrm{w}}\mathbf{x}_{\mathrm{p}} = -{}^{\mathrm{w}}\mathbf{x}_{\mathrm{h}}$). It can be easily verified that ${}^{\mathrm{h}}\mathbf{x}_{\mathrm{h}}$ is an eigenvector of ${}^{\mathrm{h}}\mathbf{E}$ corresponding to the eigenvalue e_{11}. The similarity transformations of (43) do not affect the eigenvalues of matrices and only rotate the eigenvectors with the ${}^{\mathrm{w}}\mathbf{R}_{\mathrm{h}}$ transformation, implying that e_{11} is an eigenvalue of ${}^{\mathrm{w}}\mathbf{E}$ and its corresponding eigenvector is ${}^{\mathrm{w}}\mathbf{x}_{\mathrm{h}}$, and due to their parallelism, ${}^{\mathrm{w}}\mathbf{x}_{\mathrm{p}}$ is also a corresponding eigenvector. Thus, the expression of ${}^{\mathrm{w}}\mathbf{E}{}^{\mathrm{w}}\boldsymbol{\omega}$ using the principle frame basis vectors can be easily found:

$$ {}^{\mathrm{w}}\mathbf{E}{}^{\mathrm{w}}\boldsymbol{\omega} = {}^{\mathrm{w}}\mathbf{E}\Omega{}^{\mathrm{w}}\mathbf{x}_{\mathrm{p}} = e_{11}\Omega{}^{\mathrm{w}}\mathbf{x}_{\mathrm{p}}. \tag{51} $$

Recasting the ${}^{\mathrm{w}}\mathbf{D}{}^{\mathrm{w}}\mathbf{f}$ term of (42) is performed in a similar manner. It is also easily verified that ${}^{\mathrm{h}}\mathbf{D}$ has two eigenvalues: d_{11} and d_{22}. The d_{11} eigenvalue has the corresponding eigenvector ${}^{\mathrm{h}}\mathbf{x}_{\mathrm{h}}$ and an eigenspace spanned by $\{{}^{\mathrm{h}}\mathbf{y}_{\mathrm{h}}, {}^{\mathrm{h}}\mathbf{z}_{\mathrm{h}}\}$ corresponds to the eigenvalue d_{22}. Any vector that is a linear combination of ${}^{\mathrm{h}}\mathbf{y}_{\mathrm{h}}$ and ${}^{\mathrm{h}}\mathbf{z}_{\mathrm{h}}$ will be scaled by the eigenvalue d_{22}. Again, eigenvalues are preserved under similarity transformations, so the subsequent eigenvalues and eigenvectors of ${}^{\mathrm{w}}\mathbf{D}$ are d_{11} corresponding to ${}^{\mathrm{w}}\mathbf{x}_{\mathrm{h}}$ and d_{22} corresponding to any vector fo[illegible] the span of $\{{}^{\mathrm{w}}\mathbf{y}_{\mathrm{h}}, {}^{\mathrm{w}}\mathbf{z}_{\mathrm{h}}\}$. The force ${}^{\mathrm{w}}\mathbf{f}$ acting on the microswimmer can be br[illegible]to two component vectors with one parallel to the eigenvector ${}^{\mathrm{w}}\mathbf{x}_{\mathrm{h}}$, which is aligned with the central axis of the helix, and the other perpendicular (i.e., in the span of ${}^{\mathrm{s}}\mathbf{y}_{\mathrm{h}}$ and ${}^{\mathrm{s}}\mathbf{z}_{\mathrm{h}}$):

$$ {}^{\mathrm{w}}\mathbf{f} = \big((\mathbf{f}\cdot\mathbf{x}_{\mathrm{h}}){}^{\mathrm{w}}\mathbf{x}_{\mathrm{h}}\big) + \big((\mathbf{f}\cdot\mathbf{y}_{\mathrm{h}}){}^{\mathrm{w}}\mathbf{y}_{\mathrm{h}} + (\mathbf{f}\cdot\mathbf{z}_{\mathrm{h}}){}^{\mathrm{w}}\mathbf{z}_{\mathrm{h}}\big) = {}^{\mathrm{w}}\mathbf{f}_{\parallel\mathrm{h}} + {}^{\mathrm{s}}\mathbf{f}_{\perp\mathrm{h}}. \tag{52} $$

Both ${}^{\mathrm{w}}\mathbf{f}$ and ${}^{\mathrm{w}}\mathbf{f}_{\parallel\mathrm{h}}$ are unaffected by the spinning of the microswimmer about the ${}^{\mathrm{w}}\mathbf{x}_{\mathrm{h}}$ axis, implying that ${}^{\mathrm{w}}\mathbf{f}_{\perp\mathrm{h}}$ remains unchanged as well. Using this fact, and because both ${}^{\mathrm{w}}\mathbf{y}_{\mathrm{p}}$ and ${}^{\mathrm{w}}\mathbf{z}_{\mathrm{p}}$ are in the span of $\{{}^{\mathrm{w}}\mathbf{y}_{\mathrm{h}}, {}^{\mathrm{w}}\mathbf{z}_{\mathrm{h}}\}$, ${}^{\mathrm{w}}\mathbf{f}_{\perp\mathrm{h}}$ can be written as linear combinations of ${}^{\mathrm{w}}\mathbf{y}_{\mathrm{p}}$ and ${}^{\mathrm{w}}\mathbf{z}_{\mathrm{p}}$. In fact, as can be seen from Fig. 3, no component of ${}^{\mathrm{w}}\mathbf{f}_{\perp\mathrm{h}}$ lies in the direction of ${}^{\mathrm{w}}\mathbf{y}_{\mathrm{p}}$, making ${}^{\mathrm{w}}\mathbf{f}_{\perp\mathrm{h}} = (\mathbf{f}\cdot\mathbf{z}_{\mathrm{p}}){}^{\mathrm{w}}\mathbf{z}_{\mathrm{p}}$. This implies that ${}^{\mathrm{w}}\mathbf{f}_{\perp\mathrm{h}}$ is an eigenvector corresponding to eigenvalue d_{22} and, along with the fact that ${}^{\mathrm{w}}\mathbf{f}_{\parallel\mathrm{h}}$ is an eigenvector corresponding to eigenvalue d_{11}, leads us to write the ${}^{\mathrm{w}}\mathbf{D}{}^{\mathrm{w}}\mathbf{f}$ term of (42) using the principle frame basis:

$$ \begin{aligned} {}^{\mathrm{w}}\mathbf{D}{}^{\mathrm{w}}\mathbf{f} &= {}^{\mathrm{w}}\mathbf{D}{}^{\mathrm{w}}\mathbf{f}_{\parallel\mathrm{h}} + {}^{\mathrm{w}}\mathbf{D}{}^{\mathrm{w}}\mathbf{f}_{\perp\mathrm{h}} = d_{11}{}^{\mathrm{w}}\mathbf{f}_{\parallel\mathrm{h}} + d_{22}{}^{\mathrm{w}}\mathbf{f}_{\perp\mathrm{h}} \\ &= d_{11}(\mathbf{f}\cdot\mathbf{x}_{\mathrm{p}}){}^{\mathrm{w}}\mathbf{x}_{\mathrm{p}} + d_{22}(\mathbf{f}\cdot\mathbf{z}_{\mathrm{p}}){}^{\mathrm{w}}\mathbf{z}_{\mathrm{p}}. \end{aligned} \tag{53} $$

Combining (51) and (53) produces (42) written using the basis vectors of the principle frame:

$$ {}^{\mathrm{w}}\mathbf{v} = d_{11}(\mathbf{f}\cdot\mathbf{x}_{\mathrm{p}}){}^{\mathrm{w}}\mathbf{x}_{\mathrm{p}} + d_{22}(\mathbf{f}\cdot\mathbf{z}_{\mathrm{p}}){}^{\mathrm{w}}\mathbf{z}_{\mathrm{p}} + e_{11}\Omega{}^{\mathrm{w}}\mathbf{x}_{\mathrm{p}}. \tag{54} $$

As $(\mathbf{f}\cdot\mathbf{z}_{\mathrm{p}}){}^{\mathrm{w}}\mathbf{z}_{\mathrm{p}} = {}^{\mathrm{w}}\mathbf{f}_{\perp\mathrm{h}}$ is invariant to the microswimmer's propulsive rotation and the swimmer rotates around the ${}^{\mathrm{w}}\mathbf{x}_{\mathrm{p}}$ axis, neither of the terms in (54) are affected by the rotation of the swimmer about its central axis.

Since the horizontal component of the desired velocity $\mathbf{v}_{\mathrm{hor}}$ is nonzero, we can denote the angle of $\mathbf{v}$ measured from the vertical axis of the world frame by $\alpha = \tan^{-1}(\|\mathbf{v}_{\mathrm{hor}}\|/\|\mathbf{v}_{\mathrm{ver}}\|)$. To compensate for weight, the microswimmer will need to be pitched upward by some angle above $\mathbf{v}$ as shown in Fig. 3. Let this angle be

denoted by Ψ. Taking (54) and projecting it first onto the ${}^{\mathrm{w}}\mathbf{x}_{\mathrm{p}}$ axis and then the ${}^{\mathrm{w}}\mathbf{z}_{\mathrm{p}}$ axis produces two scalar equations of the form:

$$(\mathbf{v} \cdot \mathbf{x}_{\mathrm{p}}) = d_{11}(\mathbf{f} \cdot \mathbf{x}_{\mathrm{p}}) + e_{11}\Omega \tag{55}$$

$$(\mathbf{v} \cdot \mathbf{z}_{\mathrm{p}}) = d_{22}(\mathbf{f} \cdot \mathbf{z}_{\mathrm{p}}). \tag{56}$$

The angle Ψ can be computed from (56) by recognizing from Fig. 2 that $(\mathbf{v} \cdot \mathbf{z}_{\mathrm{p}}) = -\|\mathbf{v}\| \sin(\Psi)$ and $(\mathbf{f} \cdot \mathbf{z}_{\mathrm{p}}) = \|\mathbf{f}\| \sin(\Psi - \alpha)$, producing:

$$-\|\mathbf{v}\| \sin(\Psi) = d_{22}\|\mathbf{f}\| \sin(\Psi - \alpha). \tag{57}$$

By utilizing the identity $\sin(\Psi - \alpha) = \sin(\Psi)\cos(\alpha) - \cos(\Psi)\sin(\alpha)$ and then grouping terms, we can solve for Ψ resulting in:

$$\Psi = \tan^{-1}\left(\frac{d_{22}\|\mathbf{f}\| \sin(\alpha)}{\|\mathbf{v}\| + d_{22}\|\mathbf{f}\| \cos(\alpha)}\right), \tag{58}$$

where the values for $\|\mathbf{v}\|$, $\|\mathbf{f}\|$, d_{22} and α are all known. Using α and Ψ, the solution $\tilde{\mathbf{x}}$ can be reconstructed by defining an intermediate vector $\tilde{\mathbf{v}} = \tilde{\mathbf{v}}_{\mathrm{hor}} + \tilde{\mathbf{v}}_{\mathrm{ver}}$ composed of its horizontal and vertical components, respectively, where $\tilde{\mathbf{v}}_{\mathrm{hor}} = \mathbf{v}_{\mathrm{hor}}$ and $\tilde{\mathbf{v}}_{\mathrm{ver}} = -\|\tilde{\mathbf{v}}_{\mathrm{hor}}\| \tan(\pi/2 - \alpha + \Psi)\hat{\mathbf{g}}$. The solution $\tilde{\mathbf{x}}$, then is computed as:

$$\tilde{\mathbf{x}} = \frac{\tilde{\mathbf{v}}}{\|\tilde{\mathbf{v}}\|}. \tag{59}$$

The construction of $\tilde{\mathbf{x}}$ is depicted in Fig. 3b. Once Ψ has been determined, Ω can be found from (55) after recognizing that $(\mathbf{v} \cdot \mathbf{x}_{\mathrm{p}}) = \|\mathbf{v}\| \cos(\Psi)$ and $(\mathbf{f} \cdot \mathbf{x}_{\mathrm{p}}) = -\|\mathbf{f}\| \cos(\Psi - \alpha)$:

$$\Omega = \frac{\|\mathbf{v}\| \cos(\Psi) + d_{11}\|\mathbf{f}\| \cos(\Psi - \alpha)}{e_{11}}. \tag{60}$$

To summarize the control algorithm, the commanded velocity $\mathbf{v}$ is decomposed into vertical and horizontal components using (44) and (45), respectively. If $\|\mathbf{v}_{\mathrm{hor}}\| = 0$, then (46) and (47) are used to solve for $\tilde{\mathbf{x}}$ and Ω, respectively. Otherwise, (59) and (60) are used. The magnetic field should then be perpendicular to and rotated about the axis $\tilde{\mathbf{x}}$ with a rotation speed of Ω rad/s to achieve the commanded velocity.

4. Experimental Verification

4.1. Experimental Setup

The experimental setup used to generate the controlled magnetic fields is shown in Fig. 4. The system consists of three nested sets of Helmholtz coils. Each set of Helmholtz coils generates a magnetic field that is optimally uniform in the center of the workspace, which is aligned with the axis of the coils and which varies linearly with the electrical current flowing through wire. Each set of Helmholtz coils is connected in series, such that a single current is used to power set. The three

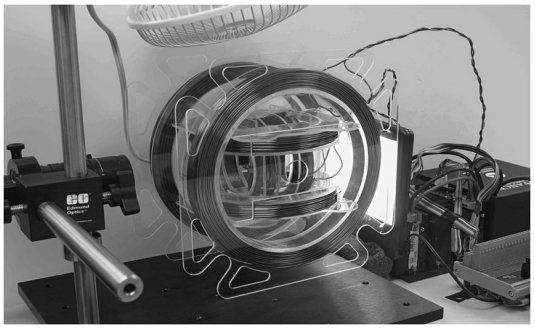

Figure 4. Experimental setup.

Table 1.
Parameters of Helmholtz coil electromagnets

Coil set	Coil radius (mm)	No. wraps (width)	No. wraps (depth)	No. wraps (total)	Resistance (Ω)	Inductance (mH)
Inner	44	9	7	63	0.5	0.944
Middle	69	9	11	99	0.9	3.78
Outer	98	13	11	143	1.6	12.2

The radius, number of wraps wide, number of wraps deep and total wraps are reported per individual coil, whereas the resistance and inductance are reported for each pair. All coils are wrapped with 14 AWG insulated copper magnet wire (1.628 mm diameter). The separation of the coils in a Helmholtz pair is equal to the radius of the coils in the pair.

sets are arranged orthogonally such that the magnetic field vector can be assigned arbitrarily, with each Helmholtz pair corresponding to one basis direction of the field vector. The details of the Helmholtz coils can be found in Table 1. Each set of Helmholtz coils is driven by an Advanced Motion Controls S16A8 PWM analog servo drive, capable of 8 A continuous current and 16 A peak current. The S16A8 is designed to drive three-phase brushless motors with sinusoidal current profiles, which is similar to the task of generating rotating magnetic fields required herein. The three S16A8 drives are powered by a single Advanced Motion Controls PS2x300W power supply. Analog communication between the PC and the drives is accomplished with a Sensoray 626 Analog and Digital I/O card. The relationship between the generated magnetic field and the commanded current was calibrated in the center of the workspace using a Hirst GM08 gaussmeter. A 25 mm $\times$ 25 mm square-cross-section vial with a length of 50 mm is located in the common center of the Helmholtz coils. A Basler A602FC camera fitted with a Computar MLH-10X macro zoom lens has a lateral view of the contents of the vial, which is backlit by a Coherent Cold Cathode ML-0405 Backlight Panel that gives high-contrast images. The entire system is cooled from above with a desk fan in a temperature-controlled room in order to maintain an approximately constant viscosity of the swimmer's

environment. The system is controlled with a PC containing a 1.2-GHz dual-core processor and 2 GB of RAM running with Linux.

4.2. Fabrication of the Magnetic Helical Swimmer

The helical swimmer pictured in Fig. 5 was fabricated from Nitinol tubing with an outer diameter of 1.0 mm and inner diameter of 0.68 mm using micro wire electrical discharge machining (WEDM). The WEDM machine was designed and built at the University of Utah to utilize small-diameter wires ranging from 50 to 100 μm [18]. For the helical cut shown in Fig. 5a, the machine was equipped with a rotary axis (A-axis) with its axis of rotation perpendicular to the EDM wire. In order to achieve a pitch of 1 mm and a helix ribbon width of 0.2 mm, the 100-μm wire first penetrated the tube to a depth of 0.15 mm below the axis of rotation (y-axis). The helix was then cut in a single sweep by synchronizing the horizontal linear motion (x-axis) with the rotation of the A-axis. Using a 100-μm brass wire at 250 V open-circuit voltage and a 5.5-nF capacitor, the EDM cuts for the helical swimmer including a cylindrical cut for attaching the magnet took approximately 1 h. The geometry of the helix was chosen to approximate the geometry of the microswimmers in Ref. [4].

As can been seen in Fig. 5a and b, a hemicylindrical pocket was machined into the 'head' of the helix. After fabricating the helix, a 1-mm long, 0.75-mm diameter axially magnetized cylindrical permanent magnet (nickel-plated NdFeB Grade N50 from SuperMagnetMan) was seated into the pocket using epoxy, such that the magnetization (i.e., dipole axis) of the magnet is perpendicular to the central axis of the helix.

The helical swimmer fabricated herein is approximately the size that could be used in a number of *in vivo* medical applications [1]. However, we are primarily interested in applying our results to the type of microswimmers that have been designed for use as untethered micromanipulators under an optical microscope. In this regard, our helical swimmer is a scaled model of the microswimmers that have been created. We use corn syrup as our fluid medium herein, whereas microswimmers would typically swim in water or a fluid with properties similar to water. To

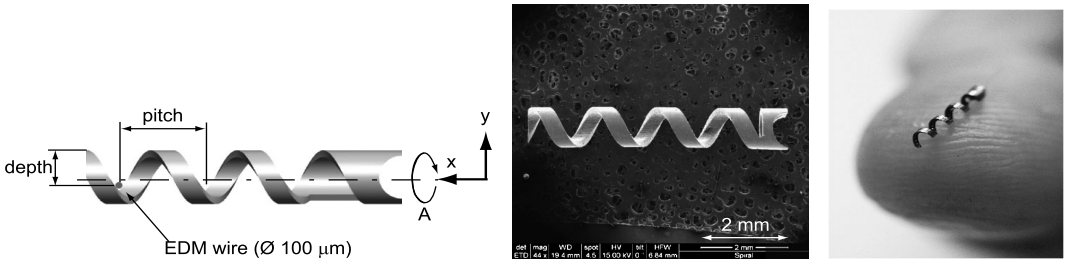

Figure 5. (a) Helical swimmer machined from 1-mm outer diameter Nitinol tubing using micro electrical discharge machining to produce a 5-mm long helix with 3.5 turns in a single sweep. (b) Scanning electron micrograph of the fabricated helix. (c) Helical swimmer on a human fingertip.

understand for what size of microswimmer our results directly apply, we consider matching of Reynolds number:

$$\mathrm{Re} = \frac{\rho_{\mathrm{mic}} L_{\mathrm{mic}} V_{\mathrm{mic}}}{\eta_{\mathrm{mic}}} = \frac{\rho_{\mathrm{mod}} L_{\mathrm{mod}} V_{\mathrm{mod}}}{\eta_{\mathrm{mod}}}, \tag{61}$$

where 'mod' denotes our model and 'mic' denotes the equivalent microscale swimmer in water. We are interested in finding the length scale of a microswimmer that corresponds to our experimental results. For our characteristic length we will consider the radius of the helix: r_{h}. For our characteristic velocity we will consider the velocity of a segment of the helix moving through the fluid: $r_{\mathrm{h}}\Omega$. The achievable rotation speed Ω is invariant to scaling, due to the fact that magnetic torque scales with volume, which is proportional to length cubed, and rotational viscous drag also scales as length cubed (see model of Section 2). The result is a relation that describes the radius of the microswimmer that matches our experimental results:

$$r_{\mathrm{h,mic}} = \sqrt{\left(\frac{\rho_{\mathrm{mod}}\eta_{\mathrm{mic}}}{\rho_{\mathrm{mic}}\eta_{\mathrm{mod}}}\right) r_{\mathrm{h,mod}}^2}. \tag{62}$$

Our model swims in corn syrup, which has a viscosity of approximately $\eta_{\mathrm{mod}} = 2500$ cps, compared to $\eta_{\mathrm{mic}} = 1$ cps for water. The density of corn syrup is approximately $\rho_{\mathrm{mod}} = 1.36$ g/ml, compared to $\rho_{\mathrm{mic}} = 1$ g/ml for water. The radius of our helical swimmer is $r_{\mathrm{h,mod}} = 420$ μm. Thus, the experimental results from our helical swimmer in corn syrup will correspond directly to a microswimmer with a radius $r_{\mathrm{h,mic}} = 9.8$ μm swimming in water, which is reasonably close to the 1.5-μm radius of the microswimmers of Ref. [4] and which places our results squarely into the low-Reynolds-number regime of interest.

4.3. Characterization of the Magnetic Helical Swimmer

Since (58) and (60) require only d_{11}, d_{22} and e_{11}, only the two terms in ${}^{\mathrm{h}}\mathbf{A}$ and the b_{11} term from ${}^{\mathrm{h}}\mathbf{B}$ need to be determined. Rather than explicitly calculating these parameters using the derived equations, (19)–(30), we experimentally measured the necessary parameters using a method similar to that described in Ref. [12] using (35) with known non-fluidic force (gravitational force in this case). The mass of the robot was measured to be 8.9 mg, resulting in a gravitational force acting on the swimmer of -8.7×10^{-5} N. Using this force, the a_{11} and a_{22} terms of ${}^{\mathrm{h}}\mathbf{A}$ were calculated by measuring the velocity of the swimmer as it sinks in the fluid at room temperature, first oriented vertically to obtain a_{11} and then horizontally to obtain a_{22}. As the swimmer sinks, a static magnetic field was applied to enforce $\boldsymbol{\omega} = \mathbf{0}$, making (35) a relation between $\mathbf{f}$ and $\mathbf{v}$. With $\mathbf{v}$ measured and $\boldsymbol{\omega} = 0$, $a_{11} = 0.42$ N·s/m and $a_{22} = 4.4$ N·s/m were found. To find the b_{11} coefficient, rather than applying a static field to force $\boldsymbol{\omega} = \mathbf{0}$, the microswimmer was oriented vertically and made to rotate fast enough so the forward propulsion in the upward direction balanced the gravitational force downward. At this point of equilibrium, $\boldsymbol{\omega}$ is known and $\mathbf{v} = 0$, turning (35) into a relation between applied force and rotation speed along the $\mathbf{x}_{\mathrm{h}}$ axis. Experimentally, the rotational

speed necessary to balance the gravitational force was found to be 2.23 Hz making $b_{11} = -3.9 \times 10^{-5}$ N · s. Since $d_{11} = 1/a_{11}$, $d_{22} = 1/a_{22}$ and $e_{11} = -b_{11}/a_{11}$, then we calculate the necessary parameters as: $d_{11} = 2.4$ N^{-1} · m/s, $d_{22} = 0.23$ N^{-1} · m/s and $e_{11} = 9.3 \times 10^{-5}$ m.

4.4. Experimental Results

A variety of experiments were performed to study how the helical swimmer discussed in Sections 4.2 behaves under open-loop velocity control. Each experiment was performed with the swimmer submerged in a 50 × 20 × 20-mm rectangular tank of corn syrup arranged in the center of the Helmholtz coils.

Presenting the user with control over the microswimmer's velocity in the world frame is an intuitive method to direct the swimmer. Without the algorithm presented in Section 3, performing simple maneuvers requires non-intuitive control over the direction to point the swimmer and how fast to rotate it. In the experiment shown in Fig. 6, the user held the vertical velocity at zero and manually adjusted the desired velocity in the horizontal direction to make the swimmer go from a stationary hover, ramp up to a constant horizontal velocity of 0.35 mm/s and then return to hover. Although it is intuitive that the swimmer must turn in the direction of the desired velocity and increase its rotation speed, the exact pitch angle from vertical and the rotation speed of the swimmer required to execute this maneuver are not immediately obvious to a human operator. With each change in input from the user, the control algorithm immediately adjusts the axis around which the magnetic field rotates and its rotational speed. The algorithm naively neglects the transient response of the swimmer to the changes in output. During the transient response, the robot sinks as seen in Fig. 6a between the swimmer at time 1 and 54 s. This is discussed further in Section 5.

The algorithm is not only designed to maintain a constant elevation by keeping $\|\mathbf{v}_{\text{ver}}\| = 0$. Figure 7a and b shows the resulting trajectories after commanding the swimmer to attain a velocity of 0.1 mm/s pitched 30° above horizontal and 30° below horizontal, respectively. The results show the swimmer moves in a straight trajectory approximately as commanded, achieving desired velocities of 0.12 mm/s 20° above horizontal and 0.17 mm/s 17° below the horizontal for the respective cases.

We found while performing the experiments that the steady-state behavior of the microswimmer is sensitive to changes in the viscosity of the corn syrup. The effect of fluid viscosity on fluidic characteristics can be understood by examining the terms of the ${}^{\text{h}}\mathbf{A}$ and ${}^{\text{h}}\mathbf{B}$ matrices. The $\xi_{\parallel}$, $\xi_{\perp}$ and $\xi_{\omega\text{m}}$ coefficients that appear in each term of ${}^{\text{h}}\mathbf{A}$ and ${}^{\text{h}}\mathbf{B}$ are linearly scaled by the viscosity of the medium (η) [15], making ${}^{\text{h}}\mathbf{A}$ and ${}^{\text{h}}\mathbf{B}$ themselves also linearly related to viscosity. The matrix ${}^{\text{h}}\mathbf{D}$ and ${}^{\text{h}}\mathbf{E}$ from which the control equations were derived are not related to viscosity in this manner, however. As ${}^{\text{h}}\mathbf{D} = {}^{\text{h}}\mathbf{A}^{-1}$, ${}^{\text{h}}\mathbf{D}$ (and subsequently its terms) is inversely proportional to viscosity. Analyzing the matrix ${}^{\text{h}}\mathbf{E} = -{}^{\text{h}}\mathbf{A}^{-1}{}^{\text{h}}\mathbf{B}$ shows that because ${}^{\text{h}}\mathbf{A}^{-1}$ is inversely proportional to viscosity and ${}^{\text{h}}\mathbf{B}$ is proportional to

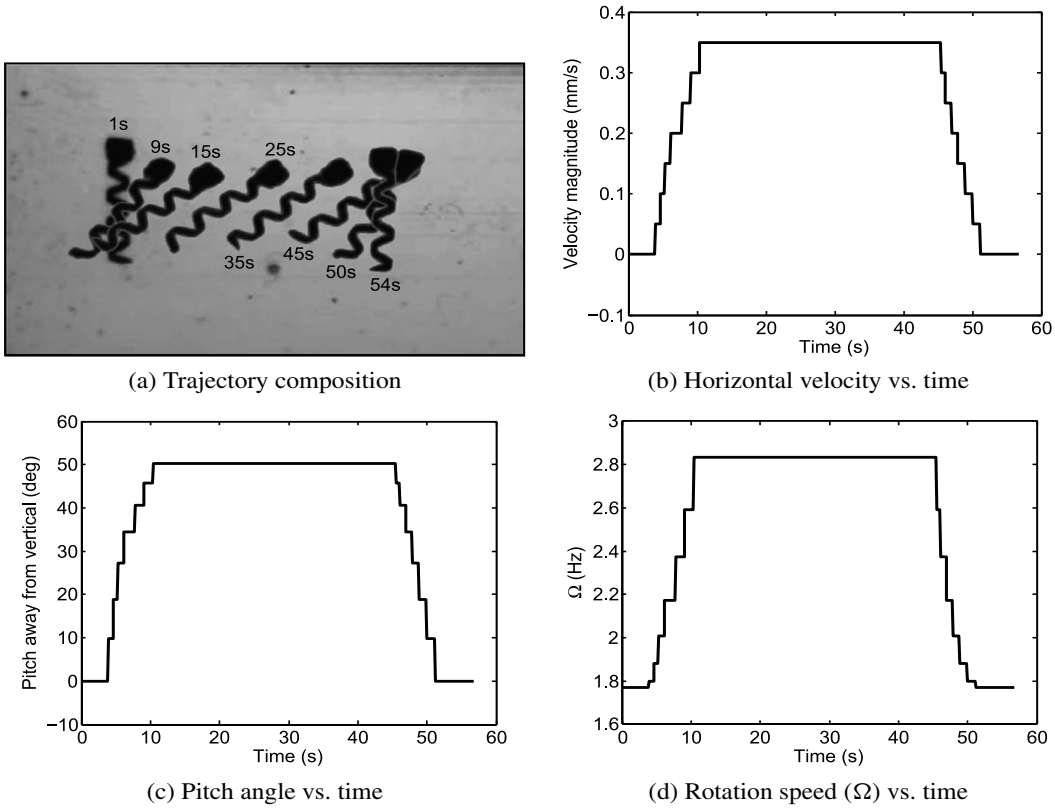

(a) Trajectory composition

(b) Horizontal velocity vs. time

(c) Pitch angle vs. time

(d) Rotation speed (Ω) vs. time

Figure 6. Experimental results of a human operator commanding a hovering swimmer to accelerate up to a constant horizontal velocity and then decelerate back to hover while imparting no vertical motion. (a) Composite image sequence. (b) Manually commanded horizontal velocity. The human operator updates the desired velocity in 0.5-mm/s steps, up to a velocity of 0.35 mm/s. The outputs to control the swimmer — the pitch angle of $\tilde{\mathbf{x}}$ (c) and the rotation speed Ω (d) — are computed by the algorithm and are not intuitive to the human operator even for simple maneuvers such as this.

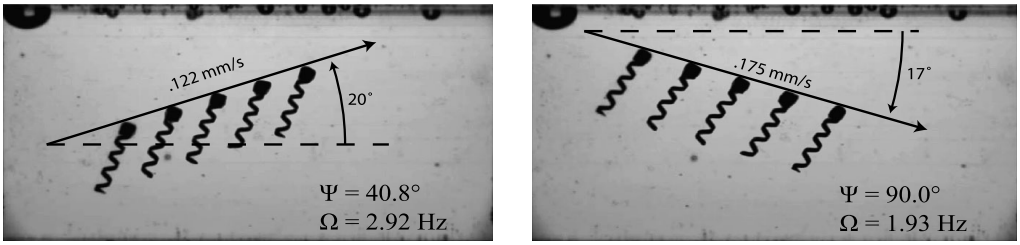

(a) Ascent under velocity control

(b) Descent under velocity control

Figure 7. Composite experimental image sequences showing resulting trajectories after commanding the swimmer to attain a velocity of (a) 0.1 mm/s angled 30° above horizontal and (b) 0.1 mm/s angled 30° below horizontal. These results show a velocity error of 33% error in direction and 22% error in magnitude for (a). For (b), the results show a velocity error of 43% error in direction and 75% error in magnitude. Detailed discussion of these errors are presented in Section 4.4.

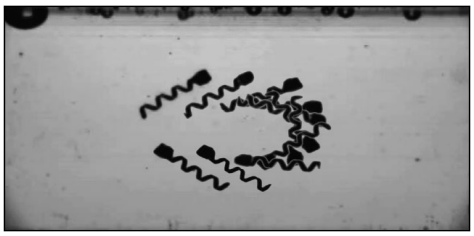

Figure 8. Composite experimental image sequence demonstrating that the algorithm seamlessly controls maneuvers such as this 'U-turn' while maintaining a constant forward velocity.

viscosity, their net effect cancels and ${}^{\mathrm{h}}\mathbf{E}$ itself is invariant to changes in viscosity. The error shown in Fig. 7 is likely attributable to a change in fluid viscosity caused by fluctuation in ambient temperature after the swimming properties were characterized using methods discussed in the preceding section, as well as changes in the distance between the swimmer and the walls of the container. Simple sensitivity analysis when commanding the swimmer to obtain a velocity of 30° above horizontal at 0.1 mm/s (as is the case shown in Fig. 7a) shows that altering the parameters d_{11} and d_{22} (near the values obtained in Section 4.3) by overpredicting viscosity by 15% induces the microrobot to swim at an angle 10% less than desired above horizontal and with magnitude 17% less than desired. Underpredicting viscosity by 15% causes the microrobot to swim at an angle 10% more than desired above horizontal with magnitude 23% greater than desired. Additionally, we have found that the sensitivity to error in viscosity increases when operating in fluids with less viscosity than that used in this paper. Although potentially large, these disturbances can be compensated for by the human operator if he/she perceives that the swimmer is not moving as desired, since correction in the velocity commands are more intuitive to the human than corrections in pitch and rotation speed.

The algorithm presented in this paper is not limited to maneuvers where the swimmer is primarily oriented vertically, like those in the preceding experiments. The algorithm can determine the necessary control outputs given any spatial velocity. Figure 8, for example, shows the trajectory of the swimmer under control of the algorithm for a maneuver where the user initially commands the swimmer to move horizontally and then rotates the velocity 180° returning back to horizontal velocity opposite that at the start (as if performing a 'U-turn' in a car), while maintaining constant velocity magnitude. As can be seen in Fig. 8, the algorithm handles maneuvers such as these seamlessly.

5. Discussion

There are a number of assumptions built into the algorithm presented herein. (i) We assume that the microswimmer is always rotating in sync with the applied field, implying that the commanded rotation speed Ω is not above the step-out frequency of the microswimmer. The step-out frequency is well understood when swimming parallel to the central axis, but the effect of steering maneuvers on step-out is not

well understood. (ii) We assume the microswimmer is swimming stably, meaning that, in addition to rotating in sync with the magnetic field, the central axis of the microswimmer $\mathbf{x}_\mathrm{h}$ is asymptotically converging on the field's rotation axis $\tilde{\mathbf{x}}$. During rapid steering maneuvers at high Ω, microswimmers have been shown to go unstable, essentially requiring a kind of system reset. These first two assumptions are highly related. (iii) If the microswimmer's transient response to steering commands is too slow (i.e., the microswimmer's central axis $\mathbf{x}_\mathrm{h}$ takes too long to converge on $\tilde{\mathbf{x}}$), the microswimmer may ascend or descend unintentionally as it turns, resulting in an error in velocity until it reaches steady state. Using a smooth desired-velocity trajectory with limits on acceleration will mitigate unintended consequences of the microswimmer's transient behavior by ensuring that the microswimmer is never asked to make rapid changes in its pitch. This acceleration cap will also mitigate potential instability. (iv) We assumed a microswimmer with a spherical permanent magnet, but our fabricated swimmer, as well as previously published microswimmers, have different magnet geometries and some have utilized soft magnetic materials. With regard to magnet geometry, it is known that viscous drag coefficients are insensitive to small changes in geometry in Stokes flow. With regard to the use of soft magnetic material, this difference is inconsequential if we satisfy the above assumptions of stable swimming below step-out.

Since the presented algorithm is open loop and subject to modeling errors, it will be subject to errors and drift, but the drift should be slower than without the algorithm, providing the human operator with time to correct for perceived errors in the microswimmer's motion. In addition, the correction required by the operator will be straightforward compared to the prior method, since directly commanding velocity in the workspace is intuitive (e.g., if the microswimmer has undesired sinking, simply command it to move upward). It will also be straightforward to incorporate the algorithm presented herein into a closed-loop position or velocity control system using sensor feedback, such as the image from an optical microscope. This is likely to only require only the 3-d.o.f. position of the microswimmer or even just focus information. During the course of our experiments, we found that the performance of the algorithm is particularly sensitive to the viscosity of the fluid, which is affected by its temperature, as well as surface effects from the container, which are widely known to be important in a low-Reynolds-number regime. As discussed above, both of these factors could be accounted for in an intuitive manner by the human operator, but both factors also motivate the potential benefits of closing a control loop using visual feedback.

6. Conclusions

We have developed a 6-d.o.f. model for helical microswimmers in a low-Reynolds-number regime. Using this model, we derived a simple open-loop controller that allows a human user to directly command a desired velocity to magnetic helical microswimmers. The method incorporates a gravity-compensation routine that pre-

vents the microswimmer from sinking due to its own weight. The method is more intuitive than controlling the orientation and rotation speed of the microswimmer directly, which is the method utilized in prior works. We found good agreement between experimental results and predictions.

Acknowledgements

This work was supported by the National Science Foundation under grants IIS-0952718 and DGE-0654414. The Nitinol tube used to manufacture the helical microswimmer was provided by Johnson Matthey Medical. The photo in Fig. 5c is courtesy *Utah Daily Chronicle*. The authors wish to thank Lisandro Leon for his contributions during the construction of the Helmholtz coil system and Kathrin Peyer (ETH Zurich) for her extremely useful correspondence on RFT.

References

1. B. J. Nelson, I. K. Kaliakatsos and J. J. Abbott, Microrobots for minimally invasive medicine, *Ann. Rev. Biomed. Eng.* **12**, 55–85 (2010).
2. C. Pawashe, S. Floyd and M. Sitti, Modeling and experimental characterization of an untethered magnetic micro-robot, *Int. J. Robotics Res.* **28**, 1077–1094 (2009).
3. D. R. Frutiger, K. Vollmers, B. E. Kratochvil and B. J. Nelson, Small, fast, and under control: wireless resonant magnetic micro-agents, *Int. J. Robotics Res.* **29**, 613–636 (2010).
4. L. Zhang, J. J. Abbott, L. X. Dong, B. E. Kratochvil, D. Bell and B. J. Nelson, Artificial bacterial flagella: fabrication and magnetic control, *Appl. Phys. Lett.* **94**, 064107 (2009).
5. M. P. Kummer, J. J. Abbott, B. E. Kratochvil, R. Borer, A. Sengul and B. J. Nelson, OctoMag: an electromagnetic systems for 5-DOF wireless micromanipulation, in: *Proc. IEEE Int. Conf. on Robotics and Automation*, Anchorage, AK, pp. 1610–1616 (2010).
6. E. M. Purcell, Life at low Reynolds number, *Am. J. Phys.* **45**, 3–11 (1977).
7. T. Honda, K. I. Arai and K. Ishiyama, Micro swimming mechanisms propelled by external magnetic fields, *IEEE Trans. Magn.* **32**, 5085–5087 (1996).
8. A. Ghosh and P. Fischer, Controlled propulsion of artificial magnetic nanostructured propellers, *Nano Lett.* **9**, 2243–2245 (2009).
9. J. J. Abbott, K. E. Peyer, M. Cosentino Lagomarsino, L. Zhang, L. X. Dong, I. K. Kaliakatsos and B. J. Nelson, How should microrobots swim? *Int. J. Robotics Res.* **28**, 1434–1447 (2009).
10. K. E. Peyer, L. Zhang, B. E. Kratochvil and B. J. Nelson, Non-ideal swimming of artificial bacterial flagella near a surface, in: *Proc. IEEE Int. Conf. Robotics and Automation*, Anchorage, AK, pp. 96–101 (2010).
11. B. Behkem and M. Sitti, Design methodology for biomimetic propulsion of miniature swimming robots, *ASME J. Dyn. Syst. Meas. Control* **128**, 36–43 (2006).
12. L. Zhang, J. J. Abbott, L. X. Dong, K. E. Peyer, B. E. Kratochvil, H. Zhang, C. Bergeles and B. J. Nelson, Characterizing the swimming properties of artificial bacterial flagella, *Nano Lett.* **9**, 3663–3667 (2009).
13. E. Lauga, W. DiLuzio, G. Whitesides and H. Stone, Swimming in circles: motion of bacteria near solid boundaries, *Biophys. J.* **90**, 400–412 (2005).
14. J. Gray and G. J. Hancock, The propulsion of sea-urchin spermatozoa, *J. Exp. Biol.* **32**, 802–814 (1955).

15. J. Lighthill, Flagellar hydrodynamics, *SIAM Rev.* **18**, 161–230 (1976).
16. J. J. Craig, *Introduction to Robotics: Mechanics and Control*, 2nd edn. Addison Wesley, Reading, MA (1989).
17. F. M. White, *Viscous Fluid Flow*, 2nd edn. McGraw-Hill, New York, NY (1991).
18. C. Orino, D. Rakwal, J. D. Jorgensen and E. Bamberg, Development of a precision, low-cost, small footprint wire electron discharge machine (WEDM), in: *Proc. Amer. Society of Precision Engineering Conf.*, Monterey, CA, pp. 239–242 (2006).

About the Authors

Arthur W. Mahoney received a BS degree in Computer Science and a BS degree in Computational Mathematics from Utah State University, Logan, UT, in 2009. As an undergraduate, he performed research and actively published in the fields of parallel computing, robot motion planning and computational biology. He is an NSF Graduate Research Fellow, a Hertz Fellowship finalist and is pursuing a PhD as a member of the Telerobotics Laboratory, Department of Mechanical Engineering, University of Utah, where he is studying magnetic control of meso- and microscale robots.

John C. Sarrazin received his MS and BS degrees in Mechanical Engineering from Montana State University, Bozeman, MT, in 2009 and 2007, respectively. He was awarded an IGERT Traineeship from the NSF for Biomimetic Robotics at the University of Utah, Salt Lake City, UT, in 2009, and is pursuing a PhD in Mechanical Engineering studying electroactive polymer actuators.

Eberhard Bamberg is currently a Research Assistant Professor in the Department of Mechanical Engineering at the University of Utah and the Director of the Precision Design Laboratory. He received a MS from Brunel University, Uxbridge, UK, in 1993, and a Dipl.-Ing. from the University of Stuttgart, Germany, in 1996, in Mechanical Engineering. He earned his PhD from the Massachusetts Institute of Technology, in 2000, in the area of precision design. His research interests include precision engineering, novel micro- and meso-level manufacturing technologies, non-traditional machining techniques for semiconductors, and optical instrumentation.

Jake J. Abbott received the PhD degree in Mechanical Engineering from Johns Hopkins University, Baltimore, MD, in 2005. He became a Postdoctoral Research Associate at the Institute of Robotics and Intelligent Systems, ETH Zurich, Switzerland, in 2005, and an Assistant Professor at the University of Utah, Salt Lake City, UT, in 2008. He is currently the Head of the Telerobotics Laboratory, Department of Mechanical Engineering, University of Utah, where his research involves medical and microscale telerobotics.

CHAPTER 3

BEHAVIOR OF ROTATING MAGNETIC MICROROBOTS ABOVE THE STEP-OUT FREQUENCY WITH APPLICATION TO CONTROL OF MULTI-MICROROBOT SYSTEMS

For all rotating untethered magnetic devices, there exists an applied field rotation frequency above which the generated magnetic torque is not strong enough to keep the magnetic device rotating synchronously with the applied field. This frequency is referred to as the "step-out" frequency (alternatively, it has also been referred to as the "cut-off" frequency). When the magnetic device is operated with the field rotating above the step-out frequency, the magnetic device's velocity rapidly declines and, to the eye, looks as if it is rotating chaotically. As a result, it has been assumed that rotating magnetic devices should always be operated so that they synchronously rotate with the applied field. In fact, the behavior of the magnetic device, above the step-out frequency, is not chaotic, and I have found that there are properties of the magnetic device's decline in velocity that can be exploited for the control of multimicrorobot systems. This is described in the following paper that was published in the journal *Applied Physics Letters*. The experimental data shown in Fig. 3(a) was provided by K. E. Peyer and B. J. Nelson from the Institute of Robotics and Intelligent Systems, ETH Zurich.

APPLIED PHYSICS LETTERS **104**, 144101 (2014)

Behavior of rotating magnetic microrobots above the step-out frequency with application to control of multi-microrobot systems

Arthur W. Mahoney,[1] Nathan D. Nelson,[2] Kathrin E. Peyer,[3] Bradley J. Nelson,[3] and Jake J. Abbott[2]
[1]*School of Computing, University of Utah, Salt Lake City, Utah 84112, USA*
[2]*Department of Mechanical Engineering, University of Utah, Salt Lake City, Utah 84112, USA*
[3]*Institute of Robotics and Intelligent Systems, ETH Zurich, CH-8092 Zurich, Switzerland*

(Received 7 March 2014; accepted 26 March 2014; published online 7 April 2014)

This paper studies the behavior of rotating magnetic microrobots, constructed with a permanent magnet or a soft ferromagnet, when the applied magnetic field rotates faster than a microrobot's step-out frequency (the frequency requiring the entire available magnetic torque to maintain synchronous rotation). A microrobot's velocity dramatically declines when operated above the step-out frequency. As a result, it has generally been assumed that microrobots should be operated beneath their step-out frequency. In this paper, we report and demonstrate properties of a microrobot's behavior above the step-out frequency that will be useful for the design and control of multi-microrobot systems. © *2014 AIP Publishing LLC*. [http://dx.doi.org/10.1063/1.4870768]

Untethered magnetic microrobots show promise for a variety of applications including minimally invasive medicine[1] and manipulation.[2] Magnetic microrobots are generally simple devices actuated by externally applied magnetic fields that exert some combination of magnetic force and torque upon the microrobot.

This paper studies microrobots whose primary form of locomotion converts magnetic torque into propulsion using a continuously rotating magnetic field. This includes microrobots that roll or propel via an attached rigid chiral structure (e.g., a helix or screw). When the applied magnetic field rotates sufficiently slowly, the microrobots synchronously rotate with the field. There exists a field rotation frequency, however, above which the applied magnetic torque is not strong enough to keep the microrobot synchronized with the field. This frequency is the "step-out" frequency.[3] The step-out frequency depends on the microrobot's magnetization, friction, and the field strength. When operated above the step-out frequency, the microrobot's velocity rapidly declines.

The ability to control multi-microrobot systems is desirable for manipulation applications.[2] Most existing multi-microrobot systems are actuated by uniform magnetic fields where each microrobot experiences the same actuating signal, making true independent control difficult. Control methods for multi-microrobot systems exist when each microrobot responds differently to the actuating signal.[4] Common techniques include designing each microrobot to convert a rotating magnetic field into spatial motion at different rates, and varying the step-out frequency between microrobots so that one loses synchronization with the rotating field before another, enabling semi-selective binary control.[3] In this paper, we present properties of a microrobot's decline in velocity, above step-out, that enables the velocity of individuals in a multi-microrobot system to be designed to selectively respond uniformly to the rotating field (where the microrobot rotation velocities are the same), respond heterogeneously where some microrobots have lost synchronization and others have not (where the ratio of the microrobot rotation velocities is large as demonstrated by Ishiyama *et al.*[3]), or respond heterogeneously with all microrobots having lost synchronization (where the ratio of the microrobot rotation velocities approaches a pre-designed constant). The phenomenon we present can be exploited by control-theoretic techniques,[4] or it can add an additional level of microrobot differentiation to existing multi-microrobot control strategies such as addressable microrobot methods, which have been demonstrated to be well-suited for positioning and manipulation tasks.[2]

When a microrobot with dipole moment $\mathbf{m} \in \mathbb{R}^3\,\mathrm{A\,m^2}$ is placed in a magnetic field $\mathbf{h} \in \mathbb{R}^3\,\mathrm{A/m}$, a magnetic torque $\boldsymbol{\tau}_\mathbf{h} = \mu_0 \mathbf{m} \times \mathbf{h}$ will be applied, where $\mu_0 = 4\pi \times 10^{-7}\,\mathrm{T\,m/A}$. For a permanent-magnet microrobot, the dipole moment is fixed with respect to the microrobot's geometry. For a microrobot with a soft-magnetic body of volume v that can be approximated as an ellipsoid, the dipole moment varies with the applied magnetic field according to $\mathbf{m} \approx v\mathcal{X}\mathbf{h}$, where $\mathcal{X} \in \mathbb{R}^{3\times3}$ is the apparent susceptibility matrix. When expressed in a coordinate system with axes aligned to the principal directions of the approximating ellipsoid, then $\mathcal{X}$ can take on the form

$$\mathcal{X} = \mathrm{diag}\left(\frac{\chi}{1+n_a\chi}, \frac{\chi}{1+n_r\chi}, \frac{\chi}{1+n_r\chi}\right), \tag{1}$$

where n_a and n_r are the demagnetization factors in the directions of the major and minor ellipse axes (so that $n_a < n_r$), respectively, and χ is the susceptibility of the material.[5] When the applied magnetic fields are sufficiently strong, then the moment becomes saturated so that $\|\mathbf{m}\| = m_{\mathrm{sat}}$ and $\mathbf{m}$ aligns to minimize the total magnetic energy. Let h_{sat} be the field magnitude required to saturate the microrobot's magnetic body.

In this paper, we assume a simple 1-degree-of-freedom (DOF) model where the magnetic microrobot's angular velocity $\boldsymbol{\omega}_\mathbf{m} \in \mathbb{R}^3\,\mathrm{rad/s}$ and the applied magnetic torque $\boldsymbol{\tau}_\mathbf{h}$ are parallel to the microrobot's principal axis, and the microrobot's dipole moment $\mathbf{m}$ and the applied field $\mathbf{h}$ are perpendicular to,

0003-6951/2014/104(14)/144101/4/$30.00

and rotate around, the same principal axis (see Fig. 1). The magnetic field's angular velocity is denoted as $\boldsymbol{\omega}_\mathbf{h} \in \mathbb{R}^3$ rad/s, which we assume to be constant. In low-Reynolds-number regimes, a microrobot's spatial velocity is generally assumed to be proportional to its rotational frequency. The magnitudes of the magnetic torque, the microrobot's angular velocity, and the magnetic field's angular velocity are denoted by τ_h, ω_m, and ω_h, respectively. Although the 1-DOF assumption is not true in general for helical microrobots, whose chiral asymmetry causes precession particularly at slow rotation speeds, the model tends to be a good approximation.

We also assume the applied magnetic field is uniform (i.e., no magnetic force is applied) and the microrobot operates in low-Reynolds-number regime fluids, where inertia is negligible and the microrobot's angular velocity is proportional to the applied magnetic torque by a viscous drag coefficient c, which varies with surface friction, fluid viscosity, and microrobot geometry. Under these assumptions, a permanent- and soft-magnetic microrobot's angular velocity can be modeled as

$$\omega_\mathrm{m} = \frac{1}{c}\tau_\mathrm{h} = \begin{cases} \omega_\mathrm{so}\sin(\alpha), & \text{permanent magnet} \\ \omega_\mathrm{so}\sin(2\alpha), & \text{soft magnet}, \end{cases} \tag{2}$$

where α is the angle illustrated in Fig. 1. The soft-magnetic microrobot's angular velocity in (2) is accurate when either well below or above saturation.[5] The scalar ω_so is the maximum angular velocity achievable (when τ_h is maximized at $\alpha = \pi/2$ rad and $\alpha = \pi/4$ rad for a permanent- and soft-magnetic microrobot, respectively).

For a permanent magnet, the step-out frequency is

$$\omega_\mathrm{so} = \mu_0 \|\mathbf{m}\| \|\mathbf{h}\| / c, \tag{3}$$

which is linear with $\|\mathbf{h}\|$ and the microrobot's dipole moment $\|\mathbf{m}\|$, which depends on the remanent magnetization and volume v of the magnetic body.

The step-out frequency of a soft-magnetic microrobot changes between the magnetic saturation regimes and is

$$\omega_\mathrm{so} = \begin{cases} \dfrac{\mu_0}{c}\dfrac{|n_a - n_r|}{2n_a n_r} v \|\mathbf{h}\|^2, & \text{when } \|\mathbf{h}\| \ll h_\mathrm{sat} \\ \dfrac{\mu_0}{c}\dfrac{|n_a - n_r|}{2} v m_\mathrm{sat}^2, & \text{when } \|\mathbf{h}\| \geq h_\mathrm{sat}, \end{cases} \tag{4}$$

which increases quadratically with $\|\mathbf{h}\|$ below saturation, but is limited by the saturated moment m_sat of the magnetic body above saturation. The step-out frequency varies with the soft-magnetic body's geometry through the demagnetization factors, n_a and n_r, and is proportional to the soft-magnetic body's volume v. Between the two magnetization regimes, the step-out frequency falls between the frequencies given in (4).

The *average* microrobot angular velocity $\bar{\omega}_\mathrm{m}$, as a function of the field rotating frequency ω_h, has been solved in closed-form for both rotating permanent magnets[6–8] and ferromagnetic ellipsoids.[9] In both cases, $\bar{\omega}_\mathrm{m}$ is found as

$$\bar{\omega}_\mathrm{m} = \begin{cases} \omega_\mathrm{h}, & \text{when } \omega_\mathrm{h} \leq \omega_\mathrm{so} \\ \omega_\mathrm{h} - \omega_\mathrm{h}\sqrt{1 - (\omega_\mathrm{so}/\omega_\mathrm{h})^2}, & \text{when } \omega_\mathrm{h} > \omega_\mathrm{so}. \end{cases} \tag{5}$$

Equation (5) can be used to study the effects of scaling an individual microrobot's step-out frequency or the comparative difference between microrobots in a group with varying step-out frequencies. Fig. 2(a) shows the scaled average microrobot angular velocity $\bar{\omega}_\mathrm{m}/\omega_\mathrm{so}$ of four hypothetical microrobots. The first microrobot (the "baseline") has a step-out frequency of ω_so and is the curve labeled A. The remaining three curves labeled B, C, and D show the scaled average angular velocity for three other microrobots whose step-out frequencies are scaled by a factor s (i.e., $s\omega_\mathrm{so}$) with $s = 2$, 3, and 4, respectively. The step-out frequency of the other microrobots could be scaled by increasing the microrobot's magnet volume by a factor of 2, 3, and 4, respectively.

The comparative effect of scaling a microrobot's step-out frequency is illustrated in Fig. 2(b), which shows the ratio $R(s)$ of each scaled microrobot's average rotation frequency to that of the baseline microrobot at the same frequency. For scaled field frequencies beneath the baseline step-out frequency $(\omega_\mathrm{h}/\omega_\mathrm{so} \leq 1)$, the ratio $R(s) = 1$. When the baseline microrobot reaches step-out, $R(s)$ increases. The maximum value of $R(s)$ occurs at the step-out frequency of the scaled microrobot, which produces

$$R_\mathrm{max}(s) = \frac{1}{1 - \sqrt{1 - (1/s)^2}} \underset{s\to\infty}{=} 2s^2. \tag{6}$$

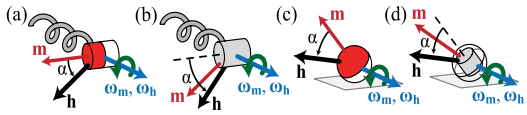

FIG. 1. This figure illustrates the 1-DOF model used herein. For permanent-magnet microrobots [(a) and (c)], α measures the angle between the applied field $\mathbf{h}$ and the microrobot's dipole moment $\mathbf{m}$. For soft-magnetic microrobots [(b) and (d)], α measures the angle between the applied field $\mathbf{h}$ and the major axis of the magnetic body.

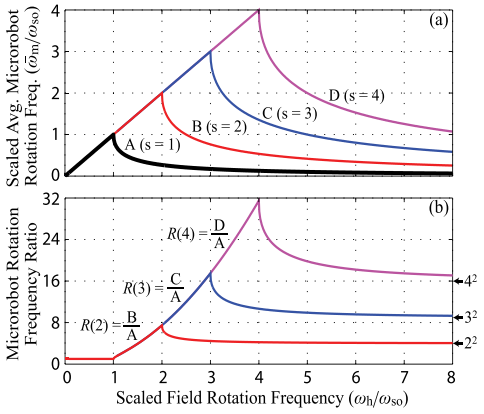

FIG. 2. (a) The scaled average microrobot rotation frequency $\bar{\omega}_\mathrm{m}/\omega_\mathrm{so}$ for four hypothetical microrobots as a function of the scaled field rotation frequency $\omega_\mathrm{h}/\omega_\mathrm{so}$, where ω_so is the step-out frequency of the "baseline" microrobot (with $s = 1$ and labeled A). The plots labeled B, C, and D are for three microrobots with the step-out frequency scaled from the baseline by factors $s = 2$, 3, and 4, respectively. (b) The ratio $R(s)$ of the scaled average microrobot rotation frequencies.

The maximum of $R(s)$ could be useful in the context of multi-microrobot control if it is desired that two sets of microrobots (denoted as set $\mathcal{A}$ and $\mathcal{B}$) have the ability to alternate between a mode where all microrobots rotate at the same frequency, and a mode where set $\mathcal{A}$ rotates a factor of $R_{\max}$ faster than set $\mathcal{B}$, selected by the magnetic field rotation frequency. In this example, the smallest factor s that the step-out frequency of the microrobots in set $\mathcal{A}$ should be scaled to achieve a desired maximum ratio $R_{\max}$ can be found by solving (6). The minimum factor s to achieve a desired $R_{\max}$ is $s \approx \sqrt{R_{\max}/2}$. Note that $R(s)$ ranges from 1 to $\sim 2s^2$ when the field rotation frequencies ranges between the baseline and scaled microrobot's step-out frequencies.

As the magnetic field rotation frequency increases past the scaled microrobot's step-out frequency, the ratio $R(s)$ drops and approaches a horizontal asymptote [see Fig. 2(b)]. In this regime, $R(s)$ is given by

$$R(s) = \frac{1 - \sqrt{1 - (s\omega_{so}/\omega_h)^2}}{1 - \sqrt{1 - (\omega_{so}/\omega_h)^2}} \underset{\omega_h \to \infty}{=} s^2. \quad (7)$$

In the context of controlling multiple sets of microrobots, the fact that $R(s)$ approaches a horizontal asymptote when both sets have lost field synchronization creates the possibility for complex control methods. For example, if there are three sets of microrobots denoted by $\mathcal{A}$, $\mathcal{B}$, and $\mathcal{C}$ with step-out frequencies scaled by factors $s = 1$, 2, and 3, respectively, then the ratios of their angular velocities can take on many combinations [refer to Fig. 2(b)]. For example, if the field is rotated at a scaled frequency in the range of [2.5, 3], then the ratio of set $\mathcal{B}$ and $\mathcal{A}$ velocities remains approximately constant near 4, while the ratio of set $\mathcal{C}$ and $\mathcal{A}$ velocities can range from approximately 12 to 18. Many combinations are possible, however a microrobot cannot rotate faster than another with a higher step-out frequency, provided the field rotates at a constant angular velocity. Additional selection can be achieved by designing groups to convert the rotating field to spatial velocity at different rates.

Fig. 3(a) shows the average microrobot rotation frequency $\bar{\omega}_m$ (left axis) and the corresponding average forward velocity (right axis) for the soft-magnetic helical swimmer[10] (shown in the inset) with two magnetizations resulting from the application of a 2 mT and 4 mT field, obtained while swimming in Methyl cellulose (0.2% w/v) near a silicon surface within a triaxial Helmholtz-coil system, which applies negligible magnetic forces. The average rotation frequency is deduced from measured forward velocity by recognizing that the microrobot and field rotation frequencies are the same below step-out (i.e., the slope of the average microrobot rotation frequency, plotted as a function of field rotation frequency, is 1 below step-out). A least-squares fit of (5) to each dataset is also shown. The step-out frequencies of the swimmer magnetized with the 2 mT (the "baseline") and 4 mT fields are 17.7 Hz and 23.9 Hz, respectively, indicating a scaling factor of $s = 1.35$. The ratio of the average microrobot rotation frequencies is plotted in Fig. 3(b), which falls in the range of [1.0, 3.0] for $\omega_h \in [17.7\,\text{Hz}, 23.9\,\text{Hz}]$, and approaches the horizontal asymptote $1.35^2 = 1.82$.

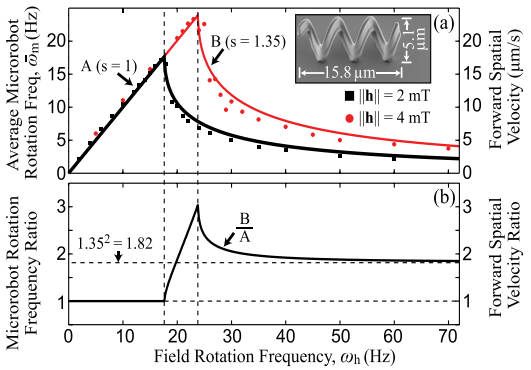

FIG. 3. (a) The average microrobot rotation frequency $\bar{\omega}_m$ for a soft-magnetic helical swimmer [shown in the inset] magnetized by a 2 mT and 4 mT magnitude field, as a function of field rotation frequency ω_h. The "baseline" swimmer ($s = 1$) is magnetized by the 2 mT magnitude field. The right axis denotes the swimmer's forward spatial velocity. The numerical similarity between the left and right axes is coincidental. (b) The ratio of the average microrobot rotation frequencies at both magnetizations. The right axis denotes the ratio of the forward spatial velocities.

Fig. 4(a) shows the average rotation frequency $\bar{\omega}_m$ for two permanent-magnet "microrobot" devices [one is shown in the inset of Fig. 4(a)], obtained from measured average device forward velocity in the same manner as Fig. 3(a), with $\|\mathbf{h}\| = 8$ mT. Each permanent-magnet "microrobot" device consists of a 2.55 mm diameter, 3.18 mm tall cylinder with an axially magnetized 1.59 mm diameter, 1.59 mm tall cylindrical NdFeB magnet positioned in the device's geometric center and polarized perpendicular to the device's longitudinal axis. Both devices are geometrically identical, but one contains an N52-grade magnet and the other contains an N42-grade magnet. The devices are actuated in a triaxial Helmholtz-coil system and roll on a polystyrene surface immersed in corn syrup with viscosity and density of 2500 cps and 1.36 g/ml, respectively. Reynolds-number analysis

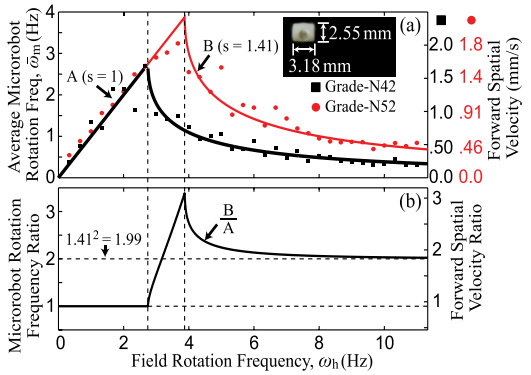

FIG. 4. (a) The average rotation frequency $\bar{\omega}_m$ is shown for two permanent-magnet rolling "microrobot" devices of the same geometry [see the inset of (a)], but one contains a N42-grade magnet and the other a N52-grade magnet, and with $\|\mathbf{h}\| = 8$ mT as a function of field rotation frequency ω_h. The right axes denote the devices' spatial velocities. (b) The ratio of the average device rotation frequencies. The right axis denotes the ratio of the devices' spatial velocities. Reynolds-number analysis predicts that both "microrobot" devices behave equivalently to a 60 μm diameter microrobot in water.

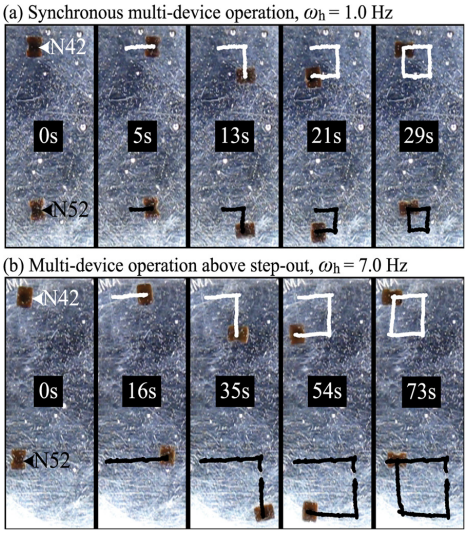

FIG. 5. A demonstration of selective control over the forward velocity ratio of two permanent-magnet "microrobot" devices by varying the field rotation frequency ω_h. In (a), both devices follow a square path with $\|\mathbf{h}\| = 8.0$ mT and $\omega_h = 1$ Hz, which is *below* both devices' step-out frequencies. The measured forward velocity ratio is 0.80. In (b), both devices follow a square path with $\|\mathbf{h}\| = 8.0$ mT and $\omega_h = 7$ Hz, which is *above* both devices' step-out frequencies. The measured forward velocity ratio is 1.7. (Multimedia view) [URL: http://dx.doi.org/10.1063/1.4870768.1]

predicts the behavior of both devices to be equivalent to a 60 μm diameter microrobot in water.

Although both "microrobot" devices are geometrically the same, unintended surface irregularities cause the forward velocity of the N42-grade device to be 9.9% faster than the N52-grade device for the same rotating frequencies. The step-out frequencies of the N42-grade (i.e., the "baseline") and N52-grade devices are 2.75 Hz and 3.88 Hz, respectively, which indicates a scaling factor of $s = 1.41$. Fig. 4(b) shows the ratio of the average device rotation frequencies, which falls in the range of [1.0, 3.38] for $\omega_h \in [2.75\,\text{Hz}, 3.88\,\text{Hz}]$, and approaches the horizontal asymptote $1.41^2 = 1.99$. The average forward velocity ratio approaches the horizontal asymptote 1.8.

Fig. 5 (with associated multimedia) demonstrates the use of the step-out behavior described herein for the simultaneous control of the two "microrobot" devices used in Fig. 4. Fig. 5(a) shows both devices actuated along a square path by driving the devices forward for 5 s, turning the devices $\pi/2$ rad clockwise over 3 s, and repeating until a square has been completed. The field rotates at 1 Hz, where both "microrobot" devices synchronously rotate, and $\|\mathbf{h}\| = 8.0$ mT. The N42- and N52-grade devices follow 4.4 mm and 3.4 mm square paths and travel at 0.88 mm/s and 0.68 mm/s, respectively, indicating a forward velocity ratio of 0.80 (Fig. 4(b) predicts 0.91).

Fig. 5(b) shows both permanent-magnet "microrobot" devices operated with $\|\mathbf{h}\| = 8.0$ mT and $\omega_h = 7$ Hz, which is above both devices' step-out frequencies. In this case, the path is generated by driving the devices for 16 s and turning for 3 s. The N42- and N52-grade "microrobot" devices follow 5.1 mm and 8.8 mm square paths and travel at 0.32 mm/s and 0.55 mm/s, respectively, indicating a forward velocity ratio of 1.7 (Fig. 4(b) predicts 1.8). This demonstrates the ability to selectively control the ratio of the microrobots' forward velocities by operating both devices above their step-out frequencies.

The analysis presented herein can add an additional level of microrobot differentiation to existing multi-microrobot control methods (e.g., addressable actuation strategies that have proven useful for positioning and manipulation[2]), and may be applied to exploit natural variance in batch-manufactured microrobots for the control of microrobot swarms. This work was partially funded by the National Science Foundation under Grant No. 0952718 and European Research Council Advanced Grant BOTMED.

[1]B. J. Nelson, I. K. Kaliakatsos, and J. J. Abbott, Annu. Rev. Biomed. Eng. **12**, 55 (2010).
[2]E. Diller and M. Sitti, Found. Trends Rob. **2**, 143 (2013).
[3]K. Ishiyama, M. Sendoh, and K. I. Arai, J. Magn. Magn. Mater. **242–245**, 41 (2002).
[4]T. Bretl, IEEE Trans. Robot. **28**, 351 (2012).
[5]J. J. Abbott, O. Ergeneman, M. P. Kummer, A. M. Hirt, and B. J. Nelson, IEEE Trans. Rob. **23**, 1247 (2007).
[6]B. H. McNaughton, K. A. Kehbien, J. N. Anker, and R. Kopelman, J. Phys. Chem. B **110**, 18958 (2006).
[7]A. Ghosh, P. Mandal, S. Karmakar, and A. Ghosh, Phys. Chem. Chem. Phys. **15**, 10817 (2013).
[8]V. M. Fomin, E. J. Smith, D. Makarov, S. Sanchez, and O. G. Schmidt, Phys. Rev. B **84**, 174303 (2011).
[9]P. Tierno, J. Claret, F. Sagues, and A. Cebers, Phys. Rev. E **79**, 021501 (2009).
[10]S. Tottori, L. Zhang, F. Qiu, K. K. Krawczyk, A. Franco-Obregón, and B. J. Nelson, Adv. Mater. **24**, 811 (2012).

CHAPTER 4

GENERATING ROTATING MAGNETIC FIELDS WITH A SINGLE PERMANENT MAGNET FOR PROPULSION OF UNTETHERED MAGNETIC DEVICES IN A LUMEN

Visualizing the rotation behavior of the dipole-shaped magnetic field produced by a single rotating permanent magnet is difficult except in a few select positions in space. As a result, prior work that employs a rotating permanent magnet for the propulsion of an untethered magnetic device has restricted operation to the easily visualized positions. This artificially imposed restriction has made rotating-permanent-magnet systems impractical for clinical use. The following paper, published in *IEEE Transactions on Robotics*, analyzes the behavior of rotating dipole fields in all positions (not just those that are easily visualized) and develops control methods that enable untethered magnetic devices to be actuated in any position relative to the rotating permanent magnet, thus eliminating the artificially imposed constraints. Systems that employ the methods that the paper presents will be much more flexible than prior work.

Generating Rotating Magnetic Fields With a Single Permanent Magnet for Propulsion of Untethered Magnetic Devices in a Lumen

Arthur W. Mahoney, *Student Member, IEEE*, and Jake J. Abbott, *Member, IEEE*

***Abstract*—To date, untethered magnetic devices actuated with a single rotating permanent magnet, such as active capsule endoscopes and magnetic microrobots, have been constrained to operate in positions where the rotating dipole field behavior is simple and easy to visualize. In this paper, we show how to generate a rotating magnetic field with any desired rotation axis, for magnetic device actuation, at any device position in space using a single rotating-magnet actuator. The methods presented can control untethered rotating magnetic devices, while the rotating actuator magnet follows trajectories independent of the untethered devices themselves. We demonstrate our methods by actuating rotating magnetic devices in a lumen. Applications include minimally invasive medical tasks requiring an untethered magnetic device to operate in natural lumen pathways of the body (e.g., the gastrointestinal system, the subarachnoid space of the nervous system, or vasculature).**

***Index Terms*—Capsule endoscopy, magnetic manipulation, medical robotics, microrobotics.**

I. Introduction

UNTETHERED magnetic devices (UMDs), such as magnetic microrobots [1] and magnetically actuated capsule endoscopes [2], have become an active area of research because of their potential impact on minimally invasive medicine. These devices derive their power from externally applied magnetic fields. Some forms of actuation utilize magnetic forces for dragging [3]–[7], others apply magnetic torque to roll on a surface [8]–[10], swim through a fluid or lumen via helical screw propulsion [11]–[15], screw through soft tissue [16], [17], or swim with a flexible tail [18]. Because these devices range in size from the microscale to the mesoscale and employ many forms of magnetic propulsion, we refer to them herein as UMDs without any implied size, propulsion method, or application. These devices can be viewed as simple end-effectors of a larger robotic system.

Due to the ability of permanent magnets to generate strong magnetic fields at low cost, researchers are considering permanent magnet systems for UMD actuation [8]–[12]. Actuation of UMDs using permanent magnets tends to be nontrivial due to the complex nature of the generated magnetic fields. In the case of actuation using a single permanent magnet, UMD control strategies developed to date have employed either attractive magnetic force *or* magnetic torque in simple ways for propulsion. Strategies exclusively employing attractive magnetic force, generated between a single permanent magnet and a UMD, employ the magnetic force for dragging [3], [4], [6], [7]. Strategies exclusively employing magnetic torque typically apply rotating magnetic fields, generated by a single rotating permanent magnet, that cause the UMD to rotate; UMD rotation is then transformed into propulsion using a helix or screw [11], [12], or by rolling [8]–[10].

Strategies that employ the magnetic force generated by a single permanent magnet tend to be limited by the fact that the force magnitude decreases faster than that of magnetic torque with increasing UMD-actuator separation distance, requiring either a large actuating magnet or performing actuation with the permanent magnet placed close to the UMD. Strategies that employ magnetic torque generated by a single rotating permanent magnet tend to be limited by the complexity of the rotating dipole field generated by the magnet. To simplify control, rotating UMDs have been exclusively operated in *radial* or *axial* positions relative to the rotating magnet (see Fig. 1) [8]–[12]. In these two positions, the rotating magnetic field $\mathbf{h}$ applied to

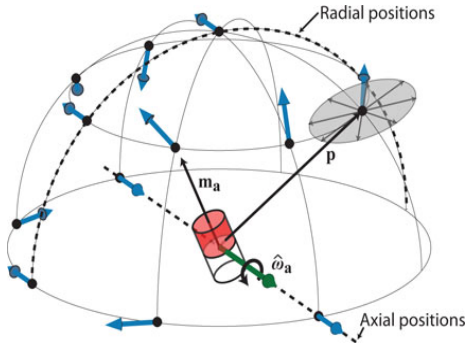

Fig. 1. When an actuator magnet with moment $\mathbf{m}_a$ rotates around the axis $\hat{\omega}_a$ with $\mathbf{m}_a$ perpendicular to $\hat{\omega}_a$, the dipole field vector $\mathbf{h}$ at any given position rotates around, and is perpendicular to, a constant axis $\hat{\omega}_h$. The axis $\hat{\omega}_h$ at various positions are illustrated with large blue arrows. A representation of the ellipse traced out by the rotating magnetic field at the position $\mathbf{p}$ is shown. Any position on the $\hat{\omega}_a$ axis is denoted to be in an *axial* position and any position in the plane spanned by the rotating $\mathbf{m}_a$ is a *radial* position. The magnetic field at $\mathbf{p}$ is illustrated by gray arrows rotating around $\hat{\omega}_h$.

Manuscript received June 6, 2013; accepted October 22, 2013. Date of publication November 21, 2013; date of current version April 1, 2014. This paper was recommended for publication by Associate Editor N. Simaan and Editor B. J. Nelson upon evaluation of the reviewers' comments. This work was supported by the National Science Foundation under Grant 0952718 and Grant 0654414.

A. W. Mahoney is with the School of Computing, University of Utah, Salt Lake City, UT 84112 USA (e-mail: art.mahoney@utah.edu).

J. J. Abbott is with the Department of Mechanical Engineering, University of Utah, Salt Lake City, UT 84112 USA (e-mail: jake.abbott@utah.edu).

This paper has supplementary multimedia (movie) downloadable material available at http://ieeexplore.ieee.org. The file size is 5.1 Mb.

Color versions of one or more of the figures in this paper are available online at http://ieeexplore.ieee.org.

Digital Object Identifier 10.1109/TRO.2013.2289019

the UMD rotates around an axis $\hat{\boldsymbol{\omega}}_{\mathrm{h}}$ that lies parallel to the actuator magnet's rotation axis $\hat{\boldsymbol{\omega}}_{\mathrm{a}}$, making it easy to visualize the coupling between the rotating actuator magnet and the UMD. Requiring UMDs to be exclusively operated in these two positions, however, significantly constrains the physical placement of the actuator magnet.

It has been shown that when a dipole (e.g., rotating permanent magnet) rotates such that its magnetic moment is perpendicular to its rotation axis, the generated field at any position in space rotates around, and is perpendicular to, a constant axis, and its field magnitude is described by an ellipse (see Fig. 1) [19]. In this paper, we reformulate this phenomenon in a manner that readily enables a unique rotation axis of the actuator magnet to be found that produces *any* desired magnetic field rotation axis (which may be specifically required to produce rotating UMD propulsion) at *any* UMD position. This removes the need for rotating UMDs to be actuated exclusively in axial and radial positions, enabling the actuator magnet's position to move freely during UMD operation to avoid obstacles in the workspace, improve control authority, and potentially employ attractive magnetic force to simultaneously contribute to propulsion.

We demonstrate our results by measuring the rotating magnetic field, and driving a threaded-capsule UMD and rolling a spherical UMD through a lumen, using a rotating permanent magnet (which we will refer to as the "actuator magnet") positioned in space by a 6-degrees-of-freedom (DOF) robotic manipulator. Applications include any minimally invasive medical task that requires a UMD to operate in the natural lumen pathways of the body (e.g., the gastrointestinal (GI) tract, the subarachnoid space of the nervous system, or vasculature). Robotic systems that apply our method for actuating UMDs will be more flexible in their choice of actuator-magnet position.

This paper contains results that first appeared in [20], as well as additional formal analysis of magnetic field properties, experimental results, and discussion. The experimental results presented are proof-of-concept experiments that confirm the theory contained herein. The problem of finding the optimal actuator-magnet position for UMD actuation, the best choice of localization system, and the magnetic fields necessary for propulsion in the human GI tract is beyond this paper's scope.

II. Controlling Rotating Untethered Magnetic Devices With a Single Rotating Permanent Magnet

In this paper, scalars are denoted by lower-case standard font (e.g., c), vectors are denoted by lower-case bold font (e.g., $\mathbf{x}$), and matrices are denoted by capital standard font (e.g., M). The $\hat{}$ symbol denotes a unit-length vector (e.g., $\hat{\mathbf{x}}$).

Let the dipole moment of the UMD's magnet be $\mathbf{m}_{\mathrm{d}} \in \mathbb{R}^3$ $\{\mathrm{A{\cdot}m^2}\}$. If a magnetic field $\mathbf{h} \in \mathbb{R}^3$ $\{\mathrm{A{\cdot}m^{-1}}\}$ is applied to the UMD, then a magnetic torque $\boldsymbol{\tau}$ $\{\mathrm{N{\cdot}m}\}$ and a magnetic force $\mathbf{f}$ $\{\mathrm{N}\}$ will be produced:

$$\boldsymbol{\tau} = \mu_0 \mathbf{m}_{\mathrm{d}} \times \mathbf{h} \tag{1}$$

$$\mathbf{f} = \mu_0 (\mathbf{m}_{\mathrm{d}} \cdot \nabla)\mathbf{h} \tag{2}$$

where $\mu_0 = 4\pi \times 10^{-7}$ $\mathrm{N{\cdot}A^{-2}}$ is the permeability of free space [21]. Note that in the literature, the magnetic field is typically denoted as $\mathbf{H}$, however, we denote it in lower-case as $\mathbf{h}$ to maintain the conventions of this paper.

The magnetic torque causes $\mathbf{m}_{\mathrm{d}}$ to rotate in the direction of $\mathbf{h}$. If the magnetic field $\mathbf{h}$ rotates around an axis $\hat{\boldsymbol{\omega}}_{\mathrm{h}}$ (with direction of rotation given by the "right-hand" rule), then $\boldsymbol{\tau}$ will cause $\mathbf{m}_{\mathrm{d}}$ (and thus the UMD) to continuously rotate. The magnetic force $\mathbf{f}$ causes the UMD to translate in a direction determined by the UMD's dipole moment $\mathbf{m}_{\mathrm{d}}$ and the spatial derivative of the magnetic field. UMD propulsion can be produced using the magnetic torque to generate UMD rotation, which is converted into propulsion via rolling or with a screw thread, the magnetic force can be employed for pulling, or both can be used in concert.

If the magnetic field $\mathbf{h}$ is generated using a single actuator magnet, then its field at the UMD's position $\mathbf{p}$ (see Fig. 1), relative to the actuator-magnet center, can be approximated by the point-dipole model

$$\mathbf{h} = \frac{1}{4\pi \|\mathbf{p}\|^3} H \mathbf{m}_{\mathrm{a}} \tag{3}$$

where $\mathbf{m}_{\mathrm{a}} \in \mathbb{R}^3$ $\{\mathrm{A{\cdot}m^2}\}$ is the dipole moment of the actuator magnet, $H = 3\hat{\mathbf{p}}\hat{\mathbf{p}}^{\mathsf{T}} - I$, and $I \in \mathbb{R}^{3\times 3}$ is the identity matrix [21]. Equation (3) exactly predicts the field produced by a spherical magnet. For all other geometries, it is an approximation that becomes more accurate with increasing distance. A nonspherical geometry can be chosen to be well approximated by (3) at smaller distances [22].

A. Rotation Axis of the Magnetic Field

For UMDs that employ magnetic torque generated by the rotating magnetic field $\mathbf{h}$ for propulsion, appropriately selecting the rotation axis $\hat{\boldsymbol{\omega}}_{\mathrm{h}}$ of the magnetic field is a critical component of the control strategy. For UMDs in free medium (e.g., helical microswimmers in fluid) or those that roll, the UMD rotation axis naturally aligns itself with $\hat{\boldsymbol{\omega}}_{\mathrm{h}}$ and varying $\hat{\boldsymbol{\omega}}_{\mathrm{h}}$ steers the UMD. For screw-like UMDs constrained in a lumen (e.g., a magnetic capsule endoscope in the small intestine), $\hat{\boldsymbol{\omega}}_{\mathrm{h}}$ should be locally aligned with the lumen in order to apply the most useful magnetic torque.

1) Choosing $\hat{\boldsymbol{\omega}}_{\mathrm{a}}$ Given $\hat{\boldsymbol{\omega}}_{\mathrm{h}}$ and $\hat{\mathbf{p}}$: For a dipole field generated by an actuator magnet that rotates around the axis $\hat{\boldsymbol{\omega}}_{\mathrm{a}}$, the required rotation axis $\hat{\boldsymbol{\omega}}_{\mathrm{a}}$ to make the magnetic field $\mathbf{h}$ at any desired position $\mathbf{p}$ rotate around a desired axis $\hat{\boldsymbol{\omega}}_{\mathrm{h}}$ is not easy to visualize. If the actuator magnet is rotated such that its dipole moment $\mathbf{m}_{\mathrm{a}}$ is perpendicular to $\hat{\boldsymbol{\omega}}_{\mathrm{a}}$ (i.e., $\mathbf{m}_{\mathrm{a}}^{\mathsf{T}}\hat{\boldsymbol{\omega}}_{\mathrm{a}} = 0$) and it is desired that the field $\mathbf{h}$ be perpendicular to $\hat{\boldsymbol{\omega}}_{\mathrm{h}}$ (i.e., $\mathbf{h}^{\mathsf{T}}\hat{\boldsymbol{\omega}}_{\mathrm{h}} = 0$), then the necessary $\hat{\boldsymbol{\omega}}_{\mathrm{a}}$ given a desired $\hat{\boldsymbol{\omega}}_{\mathrm{h}}$ can be found by substituting (3) into the projection $\mathbf{h}^{\mathsf{T}}\hat{\boldsymbol{\omega}}_{\mathrm{h}}$ and applying the symmetry of H to produce the expression

$$\mathbf{h}^{\mathsf{T}}\hat{\boldsymbol{\omega}}_{\mathrm{h}} = \frac{1}{4\pi \|\mathbf{p}\|^3} \mathbf{m}_{\mathrm{a}}^{\mathsf{T}} H \hat{\boldsymbol{\omega}}_{\mathrm{h}} = 0. \tag{4}$$

Because $H\hat{\boldsymbol{\omega}}_{\mathrm{h}}$ does not vary as the actuator magnet rotates, and because $\mathbf{m}_{\mathrm{a}}^{\mathsf{T}}\hat{\boldsymbol{\omega}}_{\mathrm{a}} = 0$, letting $\hat{\boldsymbol{\omega}}_{\mathrm{a}}$ lie parallel to $H\hat{\boldsymbol{\omega}}_{\mathrm{h}}$ is the only solution for $\hat{\boldsymbol{\omega}}_{\mathrm{a}}$ that satisfies (4) and is simultaneously invariant to the rotation of $\mathbf{m}_{\mathrm{a}}$. Therefore, given $\hat{\boldsymbol{\omega}}_{\mathrm{h}}$ and the UMD position $\mathbf{p}$, the necessary actuator-magnet rotation axis $\hat{\boldsymbol{\omega}}_{\mathrm{a}}$ can be found

with

$$\hat{\boldsymbol{\omega}}_{\mathrm{a}} = \widehat{H\hat{\boldsymbol{\omega}}_{\mathrm{h}}}. \tag{5}$$

Because H is constructed using $\hat{\mathbf{p}}$, H only varies with changes in the direction of $\hat{\mathbf{p}}$. This implies that solutions obtained from (5) are invariant to scaling $\|\mathbf{p}\|$ by moving the actuator magnet nearer to or farther away from the UMD, provided that the direction of $\mathbf{p}$ remains unchanged. Naturally, the magnitude of the field will depend on $\|\mathbf{p}\|$. In addition, it is shown in Appendix A that $\mathbf{p}$, $\hat{\boldsymbol{\omega}}_{\mathrm{h}}$, and $\hat{\boldsymbol{\omega}}_{\mathrm{a}}$ are always coplanar.

It can be easily verified using (3) that the eigenvectors of H include $\hat{\mathbf{p}}$ and a two-dimensional eigenspace consisting of vectors in the plane orthogonal to $\hat{\mathbf{p}}$, with corresponding eigenvalues $\lambda_1 = 2$ and $\lambda_2 = \lambda_3 = -1$, respectively. Because $\det(H) = \lambda_1\lambda_2\lambda_3 = 2$ for all $\mathbf{p}$, H is always invertible and there exists exactly one actuator-magnet rotation axis $\hat{\boldsymbol{\omega}}_{\mathrm{a}}$ to generate a desired field rotation about the axis $\hat{\boldsymbol{\omega}}_{\mathrm{h}}$ for any UMD position $\mathbf{p}$. The forward problem, which gives the local field axis of rotation $\hat{\boldsymbol{\omega}}_{\mathrm{h}}$ at the position $\mathbf{p}$, given the actuator magnet's axis of rotation $\hat{\boldsymbol{\omega}}_{\mathrm{a}}$, is found with

$$\hat{\boldsymbol{\omega}}_{\mathrm{h}} = \widehat{H^{-1}\hat{\boldsymbol{\omega}}_{\mathrm{a}}} \tag{6}$$

where $H^{-1} = (H - I)/2$ (derived in Appendix B). Fig. 1 shows $\hat{\boldsymbol{\omega}}_{\mathrm{h}}$ at positions on a half-hemisphere with a given $\hat{\boldsymbol{\omega}}_{\mathrm{a}}$.

With $\mathbf{p}$ obtained from a localization system and the desired applied field rotation axis $\hat{\boldsymbol{\omega}}_{\mathrm{h}}$ known, the necessary actuator-magnet axis of rotation $\hat{\boldsymbol{\omega}}_{\mathrm{a}}$ can be quickly found by (5). As the UMD or the actuator magnet moves and the direction of $\mathbf{p}$ changes, (5) must be updated by repacking the matrix H, and a new solution $\hat{\boldsymbol{\omega}}_{\mathrm{a}}$ must be produced to maintain the desired applied field rotation axis at $\mathbf{p}$. Theoretically, a desired actuator-magnet position trajectory can be first established and the necessary $\hat{\boldsymbol{\omega}}_{\mathrm{a}}$ can be found during execution given the position of the actuator magnet and the UMD. In practice, however, the actuator magnet's position trajectory should adapt to the UMD's behavior in order to maintain control authority while simultaneously avoiding hardware collisions or other constraints. If the actuator magnet is positioned using a robotic manipulator, every potential orientation of $\hat{\boldsymbol{\omega}}_{\mathrm{a}}$ may not be physically achievable at every manipulator pose due to range constraints of the manipulator's joints. This issue may be alleviated during motion planning by utilizing the fact that a desired $\hat{\boldsymbol{\omega}}_{\mathrm{a}}$ is achievable from at least two unique manipulator poses by reversing the actuator magnet's rotation direction.

2) Choosing $\hat{\mathbf{p}}$ Given $\hat{\boldsymbol{\omega}}_{\mathrm{h}}$ and $\hat{\boldsymbol{\omega}}_{\mathrm{a}}$: If the direction of the actuator magnet's rotation axis $\hat{\boldsymbol{\omega}}_{\mathrm{a}}$ is fixed (e.g., if the actuator magnet is positioned using only a 3-DOF gantry robot), then any desired applied field rotation axis $\hat{\boldsymbol{\omega}}_{\mathrm{h}}$ can still be achieved at any UMD position by sacrificing actuator-magnet positioning flexibility and placing the actuator magnet in a specific position $\hat{\mathbf{p}}$. If the direction of $\hat{\boldsymbol{\omega}}_{\mathrm{a}}$ can be reversed by changing the actuator magnet's spin direction, then there exist at least four unique directions of position $\hat{\mathbf{p}}$ where the actuator magnet can be placed to achieve any desired $\hat{\boldsymbol{\omega}}_{\mathrm{h}}$.

With the desired field rotation axis $\hat{\boldsymbol{\omega}}_{\mathrm{h}}$ given and the actuator-magnet rotation axis $\hat{\boldsymbol{\omega}}_{\mathrm{a}}$ fixed and known, the solutions for the necessary actuator-magnet position (actually computed as the position direction $\hat{\mathbf{p}}$ of the UMD relative to the actuator magnet) are found using the projection $\gamma = \hat{\mathbf{p}}^{\mathsf{T}}\hat{\boldsymbol{\omega}}_{\mathrm{h}}$, obtained by first computing the intermediate projection

$$\rho = \hat{\boldsymbol{\omega}}_{\mathrm{h}}^{\mathsf{T}}\hat{\boldsymbol{\omega}}_{\mathrm{a}} = \frac{\hat{\boldsymbol{\omega}}_{\mathrm{h}}^{\mathsf{T}} H\hat{\boldsymbol{\omega}}_{\mathrm{h}}}{\|H\hat{\boldsymbol{\omega}}_{\mathrm{h}}\|} = \frac{3\gamma^2 - 1}{\sqrt{3\gamma^2 + 1}} \tag{7}$$

after substituting (5) for $\hat{\boldsymbol{\omega}}_{\mathrm{a}}$. (The value of ρ is known since $\hat{\boldsymbol{\omega}}_{\mathrm{h}}$ and $\hat{\boldsymbol{\omega}}_{\mathrm{a}}$ are given.) Squaring both sides of (7) and grouping terms produces a polynomial in terms of the unknown γ

$$9\gamma^4 - 3\left(2 + \rho^2\right)\gamma^2 + \left(1 - \rho^2\right) = 0. \tag{8}$$

There are two solutions of (8) for γ^2, which can be found using the quadratic formula

$$\gamma_+^2 = \frac{2 + \rho^2 + \sqrt{8\rho^2 + \rho^4}}{6} \geq \frac{1}{3} \tag{9}$$

$$\gamma_-^2 = \frac{2 + \rho^2 - \sqrt{8\rho^2 + \rho^4}}{6} \leq \frac{1}{3} \tag{10}$$

and are verifiably bound by $1/3$ from below and above, respectively. After examining the right-hand side of (7), it is clear that $\rho \leq 0$ requires $\gamma^2 \leq 1/3$ and $\rho \geq 0$ requires $\gamma^2 \geq 1/3$. Given the lower and upper bounds of (9) and (10), respectively, the solution of (7) is

$$\gamma^2 = \begin{cases} \gamma_+^2 & \text{if } \rho \geq 0 \\ \gamma_-^2 & \text{if } \rho \leq 0 \end{cases}. \tag{11}$$

For a value of γ^2 given by (11), two solutions for $\hat{\mathbf{p}}$ can be found (due to $\pm\gamma$) in opposite directions of each other: the solution where $\gamma \geq 0$ is denoted by $+\hat{\mathbf{p}}$ and the opposite solution where $\gamma \leq 0$ is denoted by $-\hat{\mathbf{p}}$. Using the fact that $\hat{\boldsymbol{\omega}}_{\mathrm{a}}$, $\hat{\boldsymbol{\omega}}_{\mathrm{h}}$, and $\pm\hat{\mathbf{p}}$ are always coplanar (see Appendix A), $+\hat{\mathbf{p}}$ can be constructed by first generating an orthonormal basis for the plane spanned by $\hat{\boldsymbol{\omega}}_{\mathrm{a}}$ and $\hat{\boldsymbol{\omega}}_{\mathrm{h}}$. After selecting the first basis vector to be $\hat{\boldsymbol{\omega}}_{\mathrm{h}}$, a second basis vector $\hat{\boldsymbol{\omega}}_{\mathrm{h}}^{\perp}$ is

$$\hat{\boldsymbol{\omega}}_{\mathrm{h}}^{\perp} = \frac{(I - \hat{\boldsymbol{\omega}}_{\mathrm{h}}\hat{\boldsymbol{\omega}}_{\mathrm{h}}^{\mathsf{T}})\hat{\boldsymbol{\omega}}_{\mathrm{a}}}{\|(I - \hat{\boldsymbol{\omega}}_{\mathrm{h}}\hat{\boldsymbol{\omega}}_{\mathrm{h}}^{\mathsf{T}})\hat{\boldsymbol{\omega}}_{\mathrm{a}}\|}. \tag{12}$$

Since γ is the projection of $\hat{\mathbf{p}}$ onto $\hat{\boldsymbol{\omega}}_{\mathrm{h}}$, the vector $+\hat{\mathbf{p}}$ can be formed from the orthonormal basis as

$$+\hat{\mathbf{p}} = |\gamma|\hat{\boldsymbol{\omega}}_{\mathrm{h}} + \sqrt{1 - |\gamma|^2}\hat{\boldsymbol{\omega}}_{\mathrm{h}}^{\perp} \tag{13}$$

where $|\boldsymbol{\gamma}|$ is obtained from (11), and the solution for $-\hat{\mathbf{p}}$ is given by $-1(+\hat{\mathbf{p}})$. After $\pm\hat{\mathbf{p}}$ is determined, $\|\mathbf{p}\|$ can be selected without changing the result of (13).

There are two cases when (12) becomes degenerate and the aforementioned approach for constructing $\pm\hat{\mathbf{p}}$ breaks down, both are illustrated in Fig. 2(a). The first case occurs when $\hat{\boldsymbol{\omega}}_{\mathrm{h}} = \hat{\boldsymbol{\omega}}_{\mathrm{a}}$. In this case, it can be verified using (11) that $\gamma^2 = 1$ implying that $\pm\hat{\mathbf{p}}$ are parallel to $\hat{\boldsymbol{\omega}}_{\mathrm{h}}$ and $\hat{\boldsymbol{\omega}}_{\mathrm{a}}$. These positions correspond to axial positions (see Fig. 1). The second degenerate case occurs when $\hat{\boldsymbol{\omega}}_{\mathrm{h}} = -\hat{\boldsymbol{\omega}}_{\mathrm{a}}$. In this case, $\gamma^2 = 0$ implying that $\pm\hat{\mathbf{p}}$ must be perpendicular to $\hat{\boldsymbol{\omega}}_{\mathrm{h}}$ and $\hat{\boldsymbol{\omega}}_{\mathrm{a}}$. There are an infinite number of solutions in this case, and all correspond to radial positions (see Fig. 1). Reversing the actuator magnet's spin direction turns one degenerate case into the other.

In every other nondegenerate case, spinning the actuator magnet about $\hat{\boldsymbol{\omega}}_{\mathrm{a}}$ in one direction admits two unique solutions for $\hat{\mathbf{p}}$, and spinning in the opposite direction changes the sign of

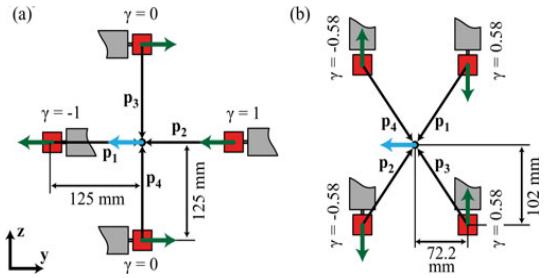

Fig. 2. (a) Configurations that cause (12) to become degenerate, for $\|\mathbf{p}\| = 125$ mm. (b) An example set of actuator-magnet position solutions that achieve a desired field rotation axis $\hat{\boldsymbol{\omega}}_\mathrm{h} = [0, -1, 0]^\mathsf{T}$ when the actuator magnet's rotation axis is constrained to $\hat{\boldsymbol{\omega}}_\mathrm{a} = [0, 0, -1]^\mathsf{T}$ and $\|\mathbf{p}\| = 125$ mm. The positions $\mathbf{p_1}$ and $\mathbf{p_2}$ are the $+\hat{\mathbf{p}}$ and $-\hat{\mathbf{p}}$ solutions, respectively, given by (13). If the actuator magnet's spin direction can be reversed such that $\hat{\boldsymbol{\omega}}_\mathrm{a} = [0, 0, 1]^\mathsf{T}$, then $\mathbf{p_3}$ and $\mathbf{p_4}$ are the corresponding $+\hat{\mathbf{p}}$ and $-\hat{\mathbf{p}}$ solutions.

ρ, produces another value of γ^2 from (11), and admits two additional unique solutions for $\hat{\mathbf{p}}$ making, in total, four unique solutions that produce a desired field rotation axis $\hat{\boldsymbol{\omega}}_\mathrm{h}$ given a reversible actuator-magnet rotation axis $\hat{\boldsymbol{\omega}}_\mathrm{a}$. Fig. 2(b) shows an example set of actuator-magnet positions that achieve a desired field rotation axis when the actuator magnet's rotation axis is constrained but is permitted to reverse direction.

B. Magnitude and Rotation Speed of the Magnetic Field

For rotating UMDs, a common failure mode that results in the loss of control authority occurs when the UMD steps out of synchronization with the rotating field as the field rotates. The rotation frequency above which the applied magnetic torque is too weak in magnitude to keep the UMD synchronized with the rotating field is referred to as the "step-out" frequency and is denoted by $\|\boldsymbol{\omega}_\mathrm{so}\|$. If a UMD's rotational dynamics are dominated by friction and inertia is negligible, then its angular velocity is approximately proportional to the magnetic torque by a linear damping coefficient c, and $\|\boldsymbol{\omega}_\mathrm{so}\|$ is the speed that requires the total available magnetic torque to maintain synchronization (a similar property holds for UMDs with nonnegligible inertia). The maximum available torque at any instant in time is $\|\boldsymbol{\tau}\|_\mathrm{max} = \mu_0 \|\mathbf{m_d}\| \|\mathbf{h}\|$ resulting in the step-out frequency $\|\boldsymbol{\omega}_\mathrm{so}\| = \|\boldsymbol{\tau}\|_\mathrm{max}/c$.

In rotating nonuniform fields produced by an actuator magnet, the applied field magnitude and angular velocity, at any given UMD position $\mathbf{p}$, depend on the orientation of $\mathbf{m_a}$ and $\mathbf{p}$. During actuator-magnet rotation, the instantaneous field magnitude $\|\mathbf{h}\|$ fluctuates in an elliptical fashion, and is

$$\|\mathbf{h}\| = \frac{\|\mathbf{m_a}\|}{4\pi\|\mathbf{p}\|^3}\sqrt{1 + 3(\hat{\mathbf{m}}_\mathbf{a}^\mathsf{T}\hat{\mathbf{p}})^2} \tag{14}$$

and the minimum and maximum field magnitudes are

$$\|\mathbf{h}\|_\mathrm{min} = \frac{\|\mathbf{m_a}\|}{4\pi\|\mathbf{p}\|^3} \tag{15}$$

$$\|\mathbf{h}\|_\mathrm{max} = \frac{\|\mathbf{m_a}\|}{4\pi\|\mathbf{p}\|^3}\sqrt{1 + 3\|\tilde{\mathbf{p}}\|^2} \tag{16}$$

where the vector $\tilde{\mathbf{p}} = (I - \hat{\boldsymbol{\omega}}_\mathrm{a}\hat{\boldsymbol{\omega}}_\mathrm{a}{}^\mathsf{T})\hat{\mathbf{p}}$ is the projection of $\hat{\mathbf{p}}$ onto the plane perpendicular to $\hat{\boldsymbol{\omega}}_\mathrm{a}$ (the plane in which $\mathbf{m_a}$ resides). The maximum field magnitude occurs when $\mathbf{m_a}$ is parallel to $\tilde{\mathbf{p}}$, and the minimum field magnitude occurs when $\mathbf{m_a}$ is perpendicular to $\tilde{\mathbf{p}}$. In the special case of $\hat{\boldsymbol{\omega}}_\mathrm{a} = \hat{\mathbf{p}}$, corresponding to the axial positions that are depicted in Fig. 1, then $\tilde{\mathbf{p}} = 0$ and $\|\mathbf{h}\|_\mathrm{min} = \|\mathbf{h}\|_\mathrm{max}$.

The instantaneous angular velocity of the applied field, as it rotates around $\hat{\boldsymbol{\omega}}_\mathrm{h}$, varies through each actuator-magnet cycle as well. If $\boldsymbol{\omega}_\mathrm{h}$ and $\boldsymbol{\omega}_\mathrm{a}$ denote the instantaneous angular velocities of the applied field and the actuator magnet, respectively, then the relation between $\|\boldsymbol{\omega}_\mathrm{h}\|$ and $\|\boldsymbol{\omega}_\mathrm{a}\|$ is given by

$$\|\boldsymbol{\omega}_\mathrm{h}\| = \left(\frac{\|\mathbf{h}\|_\mathrm{min}\|\mathbf{h}\|_\mathrm{max}}{\|\mathbf{h}\|^2}\right)\|\boldsymbol{\omega}_\mathrm{a}\|. \tag{17}$$

Because $\|\mathbf{h}\| > 0$ at all times, it is clear that the maximum angular velocity of the applied field occurs at the instant when the magnetic field strength $\|\mathbf{h}\|$ is the weakest, and the minimum angular velocity occurs when $\|\mathbf{h}\|$ is the strongest.

Because rotating the field faster than $\|\boldsymbol{\omega}_\mathrm{so}\|$ causes the UMD to become unsynchronized with the field, $\|\boldsymbol{\omega}_\mathrm{a}\|$ should be limited so that $\|\boldsymbol{\omega}_\mathrm{h}\| \leq \|\boldsymbol{\omega}_\mathrm{so}\|$ for all time. Since both the magnitude and angular velocity of the rotating field vary through each cycle, the maximum actuator-magnet rotation speed that guarantees synchronization also varies through each cycle. The maximum actuator speed can be found using

$$\|\boldsymbol{\omega}_\mathrm{h}\| \leq \|\boldsymbol{\omega}_\mathrm{so}\| = \frac{\|\boldsymbol{\tau}\|_\mathrm{max}}{c} = \frac{\mu_0\|\mathbf{m_d}\|\|\mathbf{h}\|}{c}. \tag{18}$$

Substituting (17) for $\|\boldsymbol{\omega}_\mathrm{h}\|$, then solving for $\|\boldsymbol{\omega}_\mathrm{a}\|$ produces

$$\|\boldsymbol{\omega}_\mathrm{a}\| \leq \frac{\mu_0\|\mathbf{m_d}\|\|\mathbf{h}\|^3}{c\|\mathbf{h}\|_\mathrm{min}\|\mathbf{h}\|_\mathrm{max}}. \tag{19}$$

The fastest constant actuator-magnet angular velocity that satisfies (19) can be found as

$$\|\boldsymbol{\omega}_\mathrm{a}\| = \frac{\mu_0\|\mathbf{m_d}\|\|\mathbf{h}\|_\mathrm{min}^2}{c\|\mathbf{h}\|_\mathrm{max}} \tag{20}$$

after substituting $\|\mathbf{h}\|_\mathrm{min}$ for $\|\mathbf{h}\|$ in (19).

If desired, the step-out frequency can be increased by moving the rotating actuator magnet closer to the UMD (i.e., decreasing $\|\mathbf{p}\|$ and increasing $\|\mathbf{h}\|$), without changing the solution for $\hat{\boldsymbol{\omega}}_\mathrm{h}$. This should be done with care, however, as decreasing $\|\mathbf{p}\|$ also increases the applied magnetic force. In most situations, it is likely that the friction coefficient c will vary and will not be known *a priori*. For magnetic capsule endoscopy, Hall-effect sensors aboard a mockup capsule have been used to estimate the onset of step-out [23]. When step-out is detected, either the actuator magnet should adapt by moving closer to the capsule or by rotating slower.

C. Applied Magnetic Force

The actuator magnet's field causes a magnetic force to be applied to the UMD, which can be derived from (2) as

$$\mathbf{f} = \frac{3\mu_0}{4\pi\|\mathbf{p}\|^4}\left(\hat{\mathbf{p}}\mathbf{m}_\mathbf{d}^\mathsf{T} + \mathbf{m_d}\hat{\mathbf{p}}^\mathsf{T} + (\mathbf{m}_\mathbf{d}^\mathsf{T}\hat{\mathbf{p}})Z\right)\mathbf{m_a} = F\mathbf{m_a} \tag{21}$$

where the matrix $Z = I - 5\hat{\mathbf{p}}\hat{\mathbf{p}}^{\mathsf{T}}$. When actuated well beneath a UMD's step-out frequency, the magnetic force generally tends to attract the UMD toward the actuator magnet. For configurations where the actuator magnet is positioned in a way that attractive magnetic force has a component in the desired direction of propulsion, then the attractive force can be beneficial. If the actuator magnet is placed where the magnetic force has a component directed against the desired propulsion direction, then the attractive force hinders actuation.

UMDs that are able to convert a rotating magnetic field into propulsion can propel themselves against attractive forces so long as the propulsive force is larger than the magnetic force. In the case where the desired propulsion direction is against the attractive magnetic force, the rotation speed at which the UMD's propulsive force balances the attractive force is called the "break-away" speed [11]. If the UMD is actuated slower than its break-away speed, then the UMD will be attracted toward the actuator magnet. The attraction can become self-compounding as the magnetic force increases dramatically (as $\|\mathbf{p}\|^{-4}$ according to (21)) with decreasing distance between the actuator magnet and the UMD. In this paper, the UMD is actuated at distances where the UMD's weight, friction, and the propulsive force overpower any attractive magnetic force.

The ability of a rotating UMD to propel against attractive magnetic forces increases flexibility in actuator-magnet placement compared with other propulsion strategies. Stably driving a UMD away from a single permanent magnet, when solely applying magnetic force for pushing actuation, is challenging because the magnetic torque tends to align the UMD's dipole moment $\mathbf{m}_\mathrm{d}$ such that the magnetic force is always attractive.

For clinical applications, it is likely that the magnetic force must be managed to ensure safety [4], [24]. It has been found that actuating a UMD at its step-out frequency, in any actuator-magnet position, reduces the magnitude of the force and redirects it such that no component of the average magnetic force applied to the UMD over one rotation cycle is attractive [24]. In the event of loss of UMD localization or loss of control authority, the actuator magnet's ability to apply undesirable magnetic force to a UMD can be dramatically reduced by rapidly increasing the separation distance $\|\mathbf{p}\|$, or by rotating the actuator magnet well above the UMD's step-out frequency. If the actuator magnet is rotated fast enough, the UMD's dipole moment $\mathbf{m}_\mathrm{d}$ will remain approximately stationary in space. Assuming $\mathbf{p}$ is approximately constant over one actuator-magnet revolution and the actuator magnet's rotation about $\hat{\boldsymbol{\omega}}_\mathrm{a}$ is parameterized by the angle ϕ, the averaged magnetic force applied to the UMD is then

$$\bar{\mathbf{f}} = \frac{1}{2\pi}\int_0^{2\pi} F\mathbf{m}_\mathrm{a}\,d\phi = \frac{1}{2\pi}F\int_0^{2\pi}\mathbf{m}_\mathrm{a}\,d\phi = \mathbf{0} \qquad (22)$$

since F is approximately constant and the rotation of $\mathbf{m}_\mathrm{a}$ about the axis $\hat{\boldsymbol{\omega}}_\mathrm{a}$ generates an odd function in $\mathbb{R}^3$, which integrates to zero over a complete actuator-magnet revolution.

Equation (22) will become more accurate as $\|\boldsymbol{\omega}_\mathrm{h}\|$ increases above step-out. This is demonstrated in Fig. 3, which shows $\|\bar{\mathbf{f}}\|$ obtained from a simulation of a UMD whose dynamics are dominated by friction [and whose step-out frequency $\|\boldsymbol{\omega}_\mathrm{so}\|$ is given by (18)] in two positions relative to the actuator magnet. The results of Fig. 3 are nondimensionalized by scaling $\|\bar{\mathbf{f}}\|$ by $\delta = 3\mu_0\|\mathbf{m}_\mathrm{d}\|\|\mathbf{m}_\mathrm{a}\|/(4\pi\|\mathbf{p}\|^4)$ to remove the influence of $\|\mathbf{p}\|$, $\|\mathbf{m}_\mathrm{d}\|$, and $\|\mathbf{m}_\mathrm{a}\|$, and by scaling $\|\boldsymbol{\omega}_\mathrm{h}\|$ by the UMD's step-out frequency to remove the influence of friction c. The results in two UMD positions are shown. In position 1 the UMD is in a radial position. In position 2, the UMD is nearly in an axial position. In general, as the UMD's position approaches an axial position, $\|\bar{\mathbf{f}}\|$ approaches 0 for all rotation speeds. In *any* position, $\|\bar{\mathbf{f}}\|$ asymptotically approaches 0 as $\|\boldsymbol{\omega}_\mathrm{h}\|$ increases. Detailed discussion on the influence of the UMD's position on the magnetic force can be found in [24].

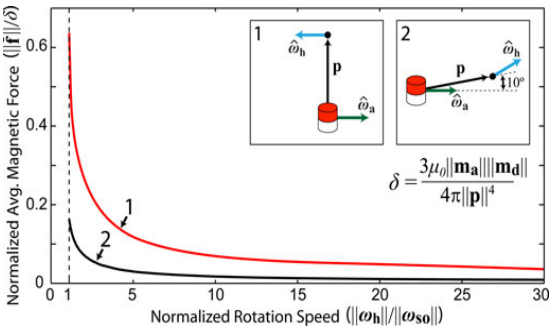

Fig. 3. The average magnetic force $\bar{\mathbf{f}}$ applied to a UMD over one actuator-magnet revolution asymptotically approaches $\mathbf{0}$ as the rotation frequency increases above step-out. Nondimensionalized simulation results of $\|\bar{\mathbf{f}}\|$ (normalized by δ) are shown for a UMD whose dynamics are dominated by friction (the step-out frequency is given by (18)) as $\|\boldsymbol{\omega}_\mathrm{h}\|$ (normalized by $\|\boldsymbol{\omega}_\mathrm{so}\|$) increases. Results in two UMD positions are shown.

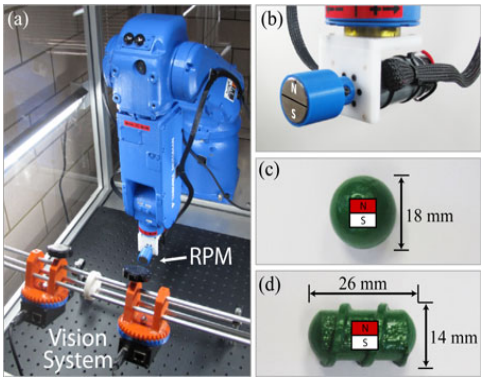

Fig. 4. The Yaskawa Motoman MH5 6-DOF robotic manipulator (a) is used to position the actuator magnet (b) for point-dipole calibration, and for actuating a spherical rolling UMD (c) and a threaded capsule-mockup UMD (d). The screw thread of the capsule UMD has a pitch of 7 mm and is 1.5 mm deep. Both devices contain a 6.35- mm cube Grade-N52 NdFeB magnet.

III. Experimental Results and Discussion

In our experiments, the actuator magnet is positioned with a Yaskawa Motoman MH5 6-DOF robotic manipulator [see Fig. 4(a)], and consists of a cylindrical 25.4 mm diameter, 25.4 mm long, Grade-N42, diametrically magnetized (i.e., along the diameter) NdFeB permanent magnet [see Fig. 4(b)]

driven by a Maxon 24 V A-Max DC motor with an Advanced Motion Controls servo control drive and amplifier. We demonstrate propulsion of rotating UMDs by actuating a rolling spherical device [see Fig. 4(c)], and a threaded capsule-shaped device [see Fig. 4(d)] similar to the design in [13], that produces translational motion along its principal axis from rotation around the same axis. Both UMDs contain a 6.35- mm cubic Grade-N52 NdFeB magnet positioned at the device's center of gravity, with the dipole moment oriented perpendicular to the device's principal axis in the case of the threaded capsule.

The UMDs were constrained during experimentation in a clear PVC lumen with 22.2 mm inner diameter, lightly lubricated with personal lubricant jelly. Although the PVC lumen is not representative of the human GI system, it is sufficient for our proof-of-concept experiments. (Note that there is experimental evidence to suggest that capsule-shaped UMDs, similar to Fig. 4(d), can be successfully actuated in the human GI system [13], [25].) The UMD position was obtained using a stereo vision system [see Fig. 4(a)] consisting of two Basler A602FC cameras each fitted with a 4.5- mm fixed-focal-length lens producing sub-millimeter tracking accuracy at 30 frames-per-second. Although visually tracking a UMD is not clinically relevant, it is sufficient for our proof-of-concept experiments. Existing clinically relevant UMD localization strategies include RF triangulation [26], magnetic methods [27]–[30], and CT scan or X-ray fluoroscopy [31]. Irrespective of the tracking method, the effect of localization uncertainty on the control techniques presented has been studied in [32].

The actuator magnet's dipole moment magnitude $\|\mathbf{m_a}\|$ was found using a least-squares fit of the measured field to the point-dipole model. The magnetic field was measured with a custom-made three-axis sensor shown in the corner of Fig. 5(a) and (b), constructed using three pairs of Allegro A1301 linear Hall-effect sensors mounted on the six sides of a 7- mm cube. Each sensor has a sensitivity of 25 V/T and a range of ± 0.1 T. The average value of each sensor pair on two opposing faces approximates the component of the field at the cube's center in the direction normal to the faces. One hundred samples of the field were obtained per millimeter between 30 and 140 mm from the actuator-magnet center in an axial position, resulting in the fit $\|\mathbf{m_a}\| = 12.7$ A·m^2 with $R^2 = 0.999$.

The accuracy of the fit and correctness of the theory were verified by measuring the magnetic field while rotating the actuator magnet in two positions located 100 mm from the actuator magnet's center. The positions $\mathbf{p_1} = [0, 100, 0]^\mathsf{T}$ mm [see Fig. 5(a)] and $\mathbf{p_2} = [81.61, 57.79, 0]^\mathsf{T}$ mm [see Fig. 5(b)] are described in the coordinate system depicted at the top of Fig. 5. Fig. 5(c) and (d) shows the measured and predicted magnetic fields and axes of rotation at both positions projected onto the $\mathbf{xz}$ and $\mathbf{yz}$ planes. The actuator magnet rotates at 1 rad/s in both positions. The predicted $\hat{\boldsymbol{\omega}}_\mathbf{h}$, obtained by (6), differed from the measured $\hat{\boldsymbol{\omega}}_\mathbf{h}$, obtained using principal-component analysis (the direction of least variance), by 2.94° for $\mathbf{p_1}$ and 0.73° for $\mathbf{p_2}$. Fig. 5 clearly shows that the actuator magnet's field and its axis of rotation are closely predicted by the point-dipole model with $\|\mathbf{m_a}\| = 12.7$ A·m^2 in the positions indicated, even though the actuator magnet is nonspherical. The actuator magnet's field is within 3% of a point-dipole field (3) in every position, provided $\|\mathbf{p}\| \geq 36$ mm [22].

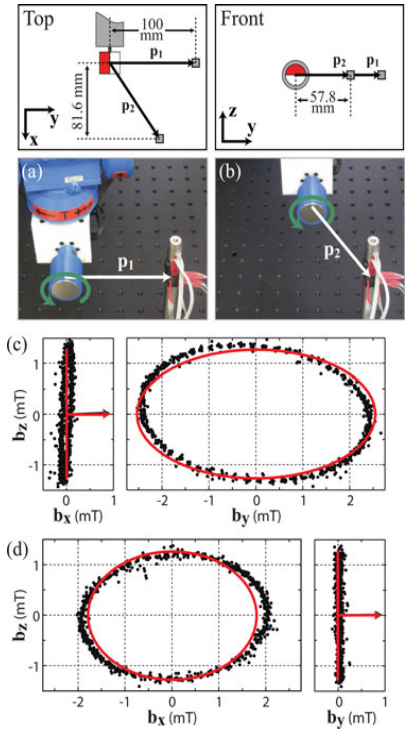

Fig. 5. The components of the magnetic flux density $\mathbf{b} = \mu_0 \mathbf{h}$ measured and predicted at the positions $\mathbf{p_1} = [0, 100, 0]^\mathsf{T}$ mm (a) and $\mathbf{p_2} = [81.61, 57.79, 0]^\mathsf{T}$ mm (b) are shown in (c) and (d), respectively. The predicted $\hat{\boldsymbol{\omega}}_\mathbf{h}$ at $\mathbf{p_1}$ and $\mathbf{p_2}$ differed from the measured $\hat{\boldsymbol{\omega}}_\mathbf{h}$ by 2.94° and 0.73°, respectively. The custom field sensor used to obtain the data appears in the lower right corners of (a) and (b). Note that in the literature, the magnetic flux density is typically denoted as $\mathbf{B}$, however, we denote it in lower-case as $\mathbf{b}$ to maintain the conventions of this paper.

The following experiments were intentionally performed at slow rotation speeds to demonstrate the methods presented herein as purely magnetic effects, with minimal contribution of inertia. Helical UMD propulsion has been previously shown to be robust to misalignment in applied-field rotation axis [32]. The successful actuation of the spherical UMD, which is more sensitive to rotation-axis alignment, will demonstrate that proper control of the rotating magnetic field is achieved.

A. *Demonstration Varying* $\hat{\boldsymbol{\omega}}_\mathbf{a}$, *Given* $\hat{\boldsymbol{\omega}}_\mathbf{h}$ *and* $\hat{\mathbf{p}}$

To date, rotating UMDs have been actuated in axial or radial positions where the applied field rotation is easy to visualize and the coupling between the actuator magnet and the UMD is easy to understand. In the radial position, for example, the magnetic field rotates around an axis parallel to that of the actuator magnet, although in the opposite direction. Actuation of the threaded UMD in the radial position is demonstrated in Fig. 6(a). While the UMD travels along the lumen (from right to left), the actuator magnet's position is maintained at $\mathbf{p} = [0, 0, -125]^\mathsf{T}$ mm (in the coordinate system depicted in

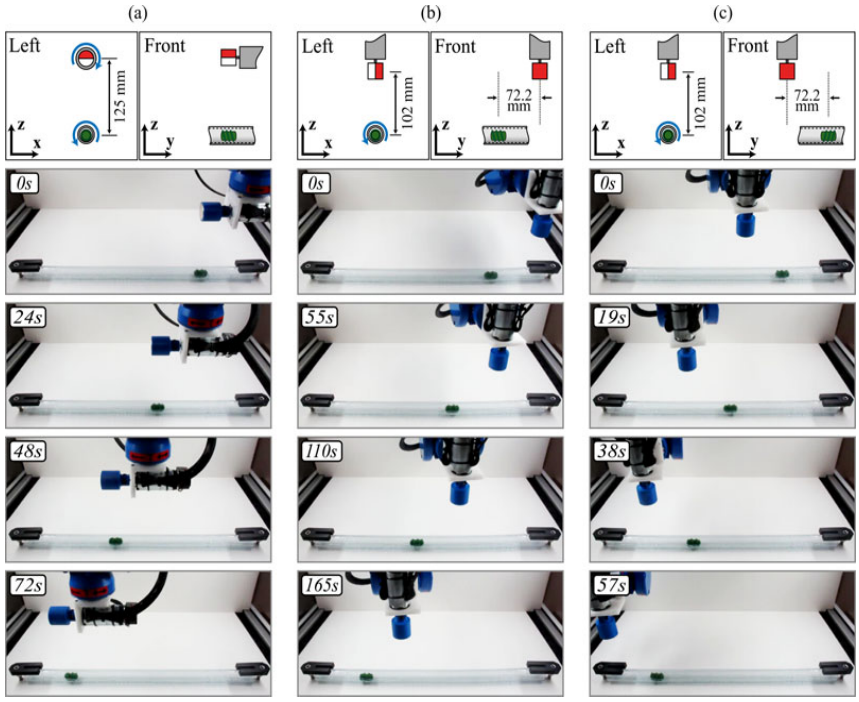

Fig. 6. The threaded capsule UMD is propelled in the (a) radial position with the actuator magnet's position regulated to maintain $\mathbf{p} = [0, 0, -125]^\mathsf{T}$ mm (in the coordinate system depicted above the captured images) where the necessary actuator-magnet rotation axis is intuitive. Captured images taken during operation with the actuator magnet's position maintained (b) at $\mathbf{p} = [0, -72.2, -102]^\mathsf{T}$ mm and (c) at $\mathbf{p} = [0, 72.2, -102]^\mathsf{T}$ mm demonstrate the UMD being actuated where the necessary actuator-magnet rotation axis (found by applying (5)) is nonintuitive. In all three examples, $\|\mathbf{p}\| = 125$ mm and the actuator magnet was rotated at a constant speed of $\|\boldsymbol{\omega}_\mathrm{a}\| = 5$ rad/s. The scale drawings above the images depict the scene from direct left and front views. Please see supplementary multimedia.

Fig. 6) using the stereo vision system. Because the external thread converts rotation about the UMD's principal axis to propulsion parallel to its principal axis, $\hat{\boldsymbol{\omega}}_\mathrm{a}$ must be parallel to the $\mathbf{y}$-axis for propulsion through the lumen. In Fig. 6(a), the UMD travels at an average speed of 3.4 mm/s. Rotating UMDs actuated in the radial position can be found in [8]–[12].

The theory presented in Section II enables operation of UMDs in nonintuitive ways. Fig. 6(b) shows the threaded UMD actuated with the actuator magnet's position regulated to maintain $\mathbf{p} = [0, -72.2, -102]^\mathsf{T}$ mm. After substituting the appropriate $\mathbf{p}$ and $\hat{\boldsymbol{\omega}}_\mathrm{h} = [0, -1, 0]^\mathsf{T}$ into (5), it can be found that the actuator magnet's rotation axis must be $\hat{\boldsymbol{\omega}}_\mathrm{a} = [0, 0, 1]^\mathsf{T}$. It is particularly nonintuitive that the necessary actuator-magnet rotation axis is perpendicular to the desired UMD rotation axis in this position. Note that the rotation axis of the field in an equivalent position is measured in Fig. 5(d). The actuator magnet is rotated at 5 rad/s and causes the UMD to travel from right to left with an average speed of 1.5 mm/s.

Although the attractive magnetic force must always be managed, it can significantly contribute to propulsion. Fig. 6(c) shows the UMD actuated with $\mathbf{p} = [0, 72.2, -102]^\mathsf{T}$ mm. In this position, a component of the magnetic force attracts the UMD in the desired direction of motion, producing an average speed of 4.3 mm/s, which is faster than the average speed in the radial position [see Fig. 6(a)], where the force neither hinders nor helps actuation, and much faster than the position where the actuator magnet trails the UMD [see Fig. 6(b)], where the force hinders actuation. This demonstrates that a rotating UMD can be simultaneously driven and pulled, using the available magnetic torque and force, resulting in faster UMD propulsion. (A threaded UMD in a similar experiment achieved forward velocities of 21.0 mm/s in the same configuration [24].)

In Fig. 6, the position of the actuator magnet is regulated to maintain a constant relative position with respect to the UMD. Due to the presence of obstacles in a clinical setting that an actuator magnet must avoid, including the patient, it is unlikely that a UMD will always be actuated in this manner. The theory presented in Section II enables a UMD to be actuated in any position, which may change as the UMD or the actuator magnet move in space, provided that the actuator magnet's rotation axis $\hat{\boldsymbol{\omega}}_\mathrm{a}$ is adjusted according to (5). This is demonstrated in Fig. 7, which shows two examples of the spherical UMD being propelled while the actuator magnet follows a trajectory independent of the UMD. In both examples, the actuator magnet's instantaneous rotation axis $\hat{\boldsymbol{\omega}}_\mathrm{a}$ is set according to (5) using the known actuator-magnet position, and the instantaneous UMD position obtained from the stereo vision system, to update the instantaneous position vector $\mathbf{p}$. Fig. 7(a) shows superimposed still images demonstrating the UMD being rolled from left to right while the actuator magnet's position remains stationary.

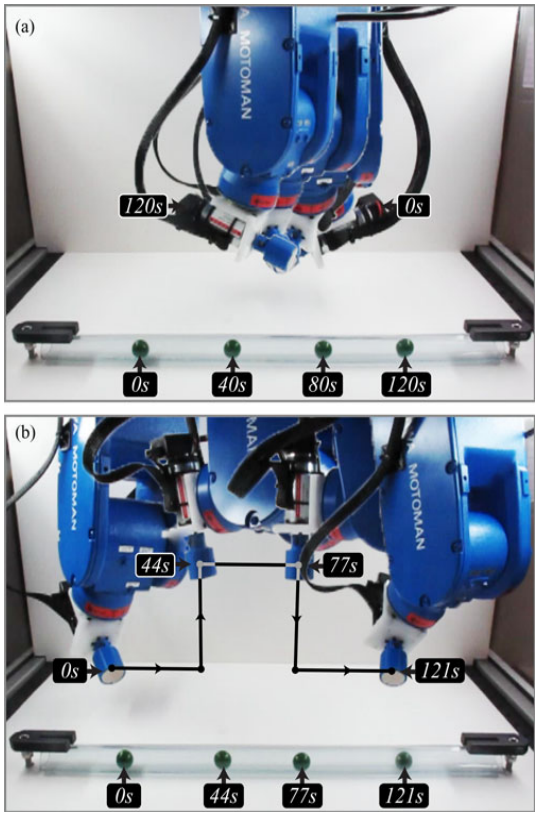

Fig. 7. The spherical UMD [see Fig. 4(c)] is propelled with the actuator magnet's position remaining stationary (a) and following a rectangular step trajectory (b). In both examples, the actuator magnet's position follows the predefined trajectory in an open-loop fashion, independent of the UMD's position. The direction of the actuator magnet's rotation axis $\hat{\boldsymbol{\omega}}_{\mathrm{a}}$ is constantly updated to maintain $\hat{\boldsymbol{\omega}}_{\mathrm{h}} = [-1, 0, 0]^{\mathsf{T}}$ (in the same coordinate system as Fig. 6) by applying (5), using the known actuator-magnet position and the measured UMD position to update the relative position $\mathbf{p}$. $\|\boldsymbol{\omega}_{\mathrm{a}}\| = 0.25$ rad/s in both cases. Please see supplementary multimedia.

In the case of Fig. 7(b), the UMD rolls from left to right while the actuator magnet follows a rectangular step trajectory. The actuator magnet initially travels parallel to the lumen until it jogs vertically at $t = 33$ s with a rate of 9.47 mm/s; at $t = 44$ s, the actuator magnet continues parallel to the lumen at 3.16 mm/s until $t = 77$ s, when the actuator magnet moves back to its original height at 9.47 mm/s; the actuator magnet then finishes moving parallel to the lumen at 3.16 mm/s. It is easy to imagine this trajectory being used to avoid an obstacle.

In both examples, $\hat{\boldsymbol{\omega}}_{\mathrm{h}} = [-1, 0, 0]^{\mathsf{T}}$ (in the same coordinate system as Fig. 6) without entering a radial or axial position, and the actuator magnet is rotated at $\|\boldsymbol{\omega}_{\mathrm{a}}\| = 0.25$ rad/s. Although both actuator-magnet trajectories are arbitrary, they demonstrate UMD actuation that was not possible using prior methods that only considered axial or radial positions. In practice, actuator-magnet position trajectories should be planned to prevent loss of control authority, employ available magnetic force, avoid collision with obstacles, avoid manipulator singularities or joint limits, and mitigate the influence of localization uncertainty on UMD actuation [32].

B. Demonstration Varying $\hat{\mathbf{p}}$, Given $\hat{\boldsymbol{\omega}}_{\mathrm{h}}$ and $\hat{\boldsymbol{\omega}}_{\mathrm{a}}$

If the rotation axis of the actuator magnet is constrained such as by the use of a 3-DOF robotic manipulator, then any desired field rotation axis can still be achieved by appropriately selecting the actuator magnet's position (refer to Section II-A2). Although they were originally obtained by setting the actuator magnet's position and solving for the required actuator-magnet axis of rotation, Fig. 6(b) and (c) can also be used to demonstrate the actuation of the capsule UMD while maintaining a constrained actuator-magnet rotation axis. In this example, the desired field rotation axis at the UMD's position is $\hat{\boldsymbol{\omega}}_{\mathrm{h}} = [0, -1, 0]^{\mathsf{T}}$, and the actuator magnet's rotation axis is constrained to lie parallel to the $\mathbf{z}$-axis, with the ability to reverse the actuator magnet's direction of spin. The four position solutions, given by (13), that achieve the desired field rotation axis are shown in Fig. 2(a). Two of the four solutions, $\mathbf{p_2}$ and $\mathbf{p_3}$, place the actuator magnet below the experimental setup's floor and are not physically achievable. The other two solutions, $\mathbf{p_1}$ and $\mathbf{p_4}$, correspond to the actuator-magnet rotation axes $\hat{\boldsymbol{\omega}}_{\mathrm{a}} = [0, 0, -1]^{\mathsf{T}}$ and $\hat{\boldsymbol{\omega}}_{\mathrm{a}} = [0, 0, 1]^{\mathsf{T}}$, and are shown in Fig. 6(b) and (c), respectively. When multiple feasible solutions exist, the position can be chosen to maximize the contribution of magnetic force to actuation, improve the robustness of actuation to uncertainty in the UMD's location [32], or maximize the configuration-space distance of the robot manipulator from singularities or joint limits.

In the previous example, the desired field rotation axis $\hat{\boldsymbol{\omega}}_{\mathrm{h}}$ remains constant through time and the four actuator-magnet position solutions never change. Fig. 8 shows superimposed still images demonstrating the spherical UMD traveling from left to right along a curved lumen, where the field rotation axis and the actuator magnet's position solutions change. At every instant in time, the position of the actuator magnet is chosen using (13) to insure that the field rotation axis $\hat{\boldsymbol{\omega}}_{\mathrm{h}}$ is always perpendicular to the curved lumen. The desired field rotation axis $\hat{\boldsymbol{\omega}}_{\mathrm{h}}$ is adjusted manually by the operator as the UMD rolls through the lumen. Fig. 8(a) shows the actuator magnet propelling the spherical UMD, while the actuator magnet's rotation axis is kept fixed at $\hat{\boldsymbol{\omega}}_{\mathrm{a}} = [-0.71, 0, 0.71]$. The case where the actuator magnet's rotation axis is kept fixed at $\hat{\boldsymbol{\omega}}_{\mathrm{a}} = [0, -0.71, 0.71]$ is shown in Fig. 8(b). Allowing the actuator magnet's spin direction to be reversed, there are four possible positions where the actuator magnet can be positioned to achieve the desired $\hat{\boldsymbol{\omega}}_{\mathrm{h}}$. Two of the potential positions obtained from (13) result in the actuator magnet being placed below the floor of the experimental setup and are physically unrealizable. One of the two physically realizable positions caused the actuator magnet and manipulator to occlude the UMD from the view of the vision system. The actuator magnet was placed in the remaining position at each time step.

C. Effects of Scaling

The actuator magnet's magnetic field scales homothetically, meaning that the field of an actuator magnet, whose dimensions

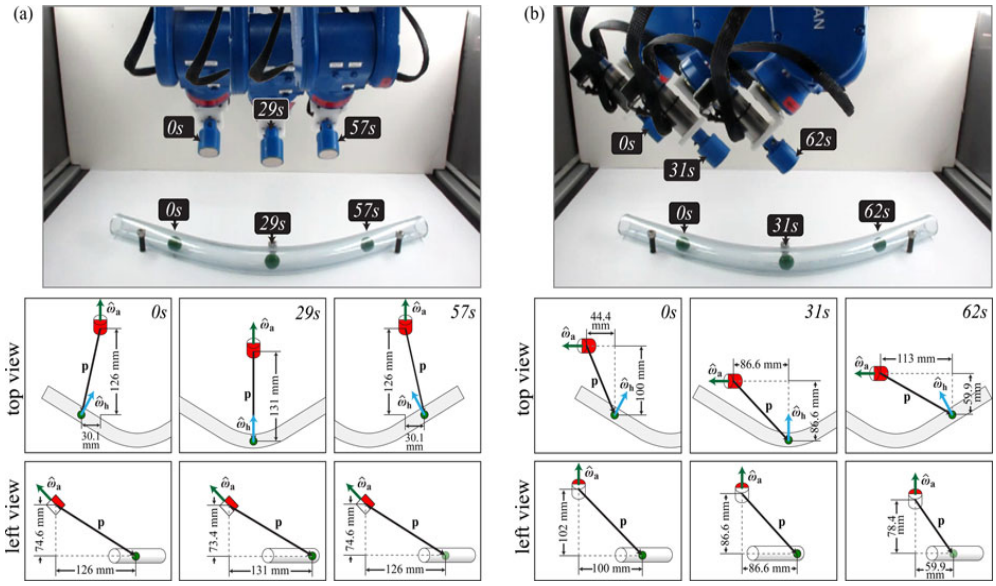

Fig. 8. Spherical UMD [see Fig. 4(c)] is propelled through a curved lumen while maintaining a constant actuator-magnet rotation axis $\hat{\boldsymbol{\omega}}_{\mathrm{a}}$. The magnetic field rotation axis $\hat{\boldsymbol{\omega}}_{\mathrm{h}}$ is kept perpendicular to the curved lumen as the spherical UMD travels. The actuator-magnet poses for three positions of the UMD in the lumen are shown where $\hat{\boldsymbol{\omega}}_{\mathrm{a}} = [-0.71, 0, 0.71]$ in (a), and where $\hat{\boldsymbol{\omega}}_{\mathrm{a}} = [0, -0.71, 0.71]$ in (b). Using the UMD position obtained from the vision system, the actuator magnet's position is adjusted according to (13) to keep $\hat{\boldsymbol{\omega}}_{\mathrm{h}}$ perpendicular to the lumen. Top and side views of each experiment pose are illustrated below (a) and (b). $\|\mathbf{p}\| = 150$ mm in all configurations. Please see supplementary multimedia.

have been scaled by a factor s, measured at the position $s\mathbf{p}$, is the same as that of the unscaled actuator magnet measured at the position $\mathbf{p}$. This can be verified using (3). Because the dipole magnetization $\|\mathbf{m}_{\mathrm{a}}\|$ is proportional to the actuator magnet's volume, scaling by s causes the magnetic dipole to become $s^3\|\mathbf{m}_{\mathrm{a}}\|$. Operating the UMD at an equivalently scaled distance away makes $\mathbf{p}$ become $s\mathbf{p}$. After substituting $s^3\|\mathbf{m}_{\mathrm{a}}\|$ and $s\mathbf{p}$ into (3) for $\|\mathbf{m}_{\mathrm{a}}\|$ and $\mathbf{p}$, respectively, the factor s^3 appears in both the numerator and the denominator and can be canceled, making the field of the scaled actuator magnet at equivalently scaled distances the same as without scaling. Since the magnetic force is amplified by the scalar $3\mu_0\|\mathbf{m}_{\mathrm{d}}\|\|\mathbf{m}_{\mathrm{a}}\|/4\pi\|\mathbf{p}\|^4$, substituting $s^3\|\mathbf{m}_{\mathrm{a}}\|$ and $s\mathbf{p}$ for $\|\mathbf{m}_{\mathrm{a}}\|$ and $\mathbf{p}$, respectively, into this amplification factor shows that the magnetic force scales as s^{-1}. This implies that when the actuator magnet's dimensions are scaled by s and the UMD is operated at an equivalently scaled distance, the magnetic field (and thus the magnetic torque) remains the same, *whereas* the magnetic force is diminished. This demonstrates that the magnetic fields generated by the actuator magnet will scale well for clinical use, assuming magnetic torque is the primary means of actuation. However, if the magnetic force is expected to assist actuation [as demonstrated in Fig. 6(c)], then diminishing the force may be undesirable.

IV. Conclusion

To date, rotating UMDs operated using a single rotating permanent magnet have been actuated in positions where the magnetic field behavior is simple and easy to visualize. Constraining the actuator magnet to these positions, however, may preclude the use of rotating-permanent-magnet actuation in clinical settings due to the presence of obstacles, including the patient's body. We have demonstrated that a desired rotating magnetic field for UMD propulsion can be generated using a single rotating actuator magnet from any position in space, which enables rotating UMDs to be actuated in any position relative to the actuator magnet, provided the UMD position is known. We have experimentally verified the theory presented in this paper by measuring the magnetic field generated by the rotating actuator magnet, and by propelling a spherical rolling UMD and a threaded capsule UMD in two different scenarios: 1) with the actuator magnet positioned arbitrarily in space and actuator magnet's rotation axis determined in a closed-loop fashion, 2) and with the actuator magnet's rotation axis fixed and the actuator magnet's position determined in a closed-loop fashion. Both scenarios assume the 3-DOF position of the UMD is found with a localization system. Systems that employ our method will not be constrained to actuate in positions where the rotating magnetic field is easy to visualize.

Appendix A

The fact that the rotation axis of the applied magnetic field $\hat{\boldsymbol{\omega}}_{\mathrm{h}}$, the UMD's position $\mathbf{p}$, and the rotation axis $\hat{\boldsymbol{\omega}}_{\mathrm{a}}$ of the actuator magnet are coplanar, can be demonstrated by expanding (5):

$$\hat{\boldsymbol{\omega}}_{\mathrm{h}} = \frac{H^{-1}\hat{\boldsymbol{\omega}}_{\mathrm{a}}}{\|H^{-1}\hat{\boldsymbol{\omega}}_{\mathrm{a}}\|} = \left(\frac{3(\hat{\mathbf{p}}^{\mathsf{T}}\hat{\boldsymbol{\omega}}_{\mathrm{a}})}{2\|H^{-1}\hat{\boldsymbol{\omega}}_{\mathrm{a}}\|}\right)\hat{\mathbf{p}} - \left(\frac{1}{\|H^{-1}\hat{\boldsymbol{\omega}}_{\mathrm{a}}\|}\right)\hat{\boldsymbol{\omega}}_{\mathrm{a}} \tag{23}$$

and thus $\hat{\boldsymbol{\omega}}_{\mathrm{h}}$ is in the span of $\hat{\mathbf{p}}$ and $\hat{\boldsymbol{\omega}}_{\mathrm{a}}$, and it holds that $\hat{\boldsymbol{\omega}}_{\mathrm{h}}$, $\hat{\mathbf{p}}$, and $\hat{\boldsymbol{\omega}}_{\mathrm{a}}$ are coplanar. It can be likewise shown that the magnetic field $\mathbf{h}$, the UMD's position vector $\mathbf{p}$, and the actuator magnet's dipole moment $\mathbf{m}_{\mathrm{a}}$ are also coplanar.

APPENDIX B

An explicit representation of H^{-1} can be found with the identity $H^2 = H + 2I$, derived using the definition of H and recognizing that $\hat{\mathbf{p}}^{\mathsf{T}}\hat{\mathbf{p}} = 1$. Multiplying both sides of H^2 by H^{-1} produces $H = I + 2H^{-1}$ and subsequently

$$H^{-1} = \frac{1}{2}(H - I). \tag{24}$$

ACKNOWLEDGMENT

The authors would like to thank K. Popek for her contribution to the custom 3-DOF magnetic field sensor and D. Cowan for his contributions toward system integration.

REFERENCES

[1] B. J. Nelson, I. K. Kaliakatsos, and J. J. Abbott, "Microrobots for minimally invasive medicine," *Annu. Rev. Biomed. Eng.*, vol. 12, pp. 55–85, 2010.

[2] J. L. Toennies, G. Tortora, M. Simi, P. Valdastri, and R. J. Webster III, "Swallowable medical devices for diagnosis and surgery: The state of the art," *J. Mech. Eng. Sci.*, vol. 224, no. 7, pp. 1397–1414, 2010.

[3] G. Ciuti, P. Valdastri, A. Menciassi, and P. Dario, "Robotic magnetic steering and locomotion of capsule endoscope for diagnostic and surgical endoluminal procedures," *Robotica*, vol. 28, no. 2, pp. 199–207, 2010.

[4] M. Salerno, R. Rizzo, E. Sinibaldi, and A. Menciassi, "Force calculation for localized magnetic driven capsule endoscopes," in *Proc. IEEE Int. Conf. Robot. Autom.*, 2013, pp. 5334–5339.

[5] M. P. Kummer, J. J. Abbott, B. E. Kratochvil, R. Borer, A. Sengul, and B. J. Nelson, "OctoMag: An electromagnetic system for 5-DOF wireless micromanipulation," *IEEE Trans. Robot.*, vol. 26, no. 6, pp. 1006–1017, Dec. 2010.

[6] G. Lien, C. Liu, J. Jiang, C. Chuang, and M. Teng, "Magnetic control system targeted for capsule endoscopic operations in the stomach: Design, fabrication, and in vitro and ex vivo evaluations," *IEEE Trans. Biomed. Eng.*, vol. 59, no. 7, pp. 2068–2079, Jul. 2012.

[7] G. T. Gillies, R. C. Ritter, W. C. Broaddus, M. S. Grady, M. A. Howard III, and R. G. McNeil, "Magnetic manipulation instrumentation for medical physics research," *Rev. Sci. Instrum*, vol. 65, no. 3, pp. 533–562, 1994.

[8] M. T. Hou, H.-M. Shen, G.-L. Jiang, C.-N. Lu, I.-J. Hsu, and J. A. Yeh, "A rolling locomotion method for untethered magnetic microrobots," *Appl. Phys. Lett.*, vol. 96, no. 024102, pp. 1–3, 2010.

[9] S. Yim and M. Sitti, "Design and rolling locomotion of a magnetically actuated soft capsule endoscope," *IEEE Trans. Robot.*, vol. 28, no. 1, pp. 183–194, Feb. 2012.

[10] A. W. Mahoney and J. J. Abbott, "Managing magnetic force applied to a magnetic device by a rotating dipole field," *Appl. Phys. Lett.*, vol. 99, no. 134103, pp. 1–3, 2011.

[11] T. W. R. Fountain, P. V. Kailat, and J. J. Abbott, "Wireless control of magnetic helical microrobots using a rotating-permanent-magnet manipulator," in *Proc. IEEE Int. Conf. Robot. Autom.*, 2010, pp. 576–581.

[12] J.-S. Lee, B. Kim, and Y.-S. Hong, "A flexible chain-based screw propeller for capsule endoscopes," *Int. J. Prec. Eng. Manuf.*, vol. 10, no. 4, pp. 27–34, 2009.

[13] A. Chiba, M. Sendoh, K. Ishiyama, K. I. Arai, H. Kawano, A. Uchiyama, and H. Takizawa, "Magnetic actuator for a capsule endoscope navigation system," *J. Magnet.*, vol. 12, no. 2, pp. 89–92, 2007.

[14] A. W. Mahoney, J. C. Sarrazin, E. Bamberg, and J. J. Abbott, "Velocity control with gravity compensation for magnetic helical microswimmers," *Adv. Robot.*, vol. 25, no. 8, pp. 1007–1028, 2011.

[15] L. Zhang, J. J. Abbott, L. X. Dong, B. E. Kratochvil, D. Bell, and B. J. Nelson, "Artificial bacterial flagella: Fabrication and magnetic control," *Appl. Phys. Lett.*, vol. 94, no. 064107, pp. 1–3, 2009.

[16] K. Ishiyama, K. I. Arai, M. Sendoh, and A. Yamazaki, "Spiral-type micromachine for medical applications," *J. Micromechatron.*, vol. 2, no. 1, pp. 77–86, 2003.

[17] A. W. Mahoney, N. D. Nelson, E. M. Parsons, and J. J. Abbott, "Non-ideal behaviors of magnetically driven screws in soft tissue," in *Proc. IEEE/RSJ Int. Conf. Intell. Robots Syst.*, 2012, pp. 3559–3564.

[18] K. Sung Hoon, S, Hashi, and K. Ishiyama, "Methodology of dynamic actuation for flexible magnetic actuator and biomimetic robotics application," *IEEE Trans. Magn.*, vol. 46, no. 6, pp. 1366–1369, Jun. 2010.

[19] E. Paperno, I. Sasada, and E. Leonovich, "A new method for magnetic position and orientation tracking," *IEEE Trans. Magn.*, vol. 37, no. 4, pp. 1938–1940, Jul. 2001.

[20] A. W. Mahoney, D. L. Cowan, K. M. Miller, and J. J. Abbott, "Control of untethered magnetically actuated tools using a rotating permanent magnet in any position," in *Proc. IEEE Int. Conf. Robot. Autom.*, 2012, pp. 3375–3380.

[21] E. P. Furlani, *Permanent Magnet and Electromechanical Devices: Materials, Analysis, and Applications*, 1st ed. San Diego, CA, USA: Academic, 2001.

[22] A. J. Petruska and J. J. Abbott, "Optimal permanent-magnet geometries for dipole field approximation," *IEEE Trans. Magn.*, vol. 49, no. 2, pp. 811–819, Feb. 2013.

[23] K. M. Miller, A. W. Mahoney, T. Schmid, and J. J. Abbott, "Proprioceptive magnetic-field sensing for closed-loop control of magnetic capsule endoscopes," in *Proc. IEEE/RSJ Int. Conf. Intell. Robots Syst.*, 2012, pp. 1994–1999.

[24] A. W. Mahoney, S. E. Wright, and J. J. Abbott, "Managing the attractive magnetic force between an untethered magnetically actuated tool and a rotating permanent magnet," in *Proc. IEEE Int. Conf. Robot. Autom.*, 2013, pp. 5346–5351.

[25] H. Zhou, G. Alici, T. D. Than, and W. Li, "Modeling and experimental characterization of propulsion of a spiral-type microrobot for medical use in gastrointestinal tract," *IEEE Trans. Biomed. Eng.*, vol. 60, no. 6, pp. 1751–1759, Jun. 2013.

[26] D. Fischer, R. Schreiber, D. Levi, and R. Eliakim, "Capsule endoscopy: The localization system," *Gastrointest. Endoscopy Clin. N. Amer.*, vol. 14, no. 1, pp. 25–31, 2004.

[27] M. Salerno, G. Ciuti, G. Lucarini, R. Rizzo, P. Valdastri, A. Menciassi, A. Landi, and P. Dario, "A discrete-time localization method for capsule endoscopy based on on-board magnetic sensing," *Meas. Sci. Technol.*, vol. 23, no. 1, pp. 1–10, 2012.

[28] M.-G. Kim, Y.-S. Hong, and E.-J. Lim, "Position and orientation detection of capsule endoscopes in spiral motion," *Int. J. Prec. Eng. Manuf.*, vol. 11, no. 1, pp. 31–37, 2010.

[29] C. Di Natali, M. Beccani, and P. Valdastri, "Real-time pose detection for magnetic medical devices," *IEEE Trans. Magn.*, vol. 49, no. 7, pp. 3524–3527, Jul. 2013.

[30] K. M. Popek, A. W. Mahoney, T. Schmid, and J. J. Abbott, "Localization method for a magnetic capsule endoscope propelled by a rotating magnetic dipole field," in *Proc. IEEE Int. Conf. Robot. Autom.*, 2013, pp. 5328–5333.

[31] F. Carpi and C. Pappone, "Magnetic maneuvering of endoscopic capsules by means of a robotic navigation system," *IEEE Trans. Biomed. Eng.*, vol. 56, no. 5, pp. 1482–1490, May 2009.

[32] A. W. Mahoney and J. J. Abbott, "Control of untethered magnetically actuated tools with localization uncertainty using a rotating permanent magnet," in *Proc. IEEE Int. Conf. Biomed. Robot. Biomechatron.*, 2012, pp. 1632–1637.

Arthur W. Mahoney (S'10) received the B.S. degrees in computer science and computational mathematics from Utah State University, Logan, UT, USA, in 2009, where he is currently working toward the Ph.D. degree in computing from the Telerobotics Laboratory.

He is a National Science Foundation Integrative Graduate Education and Research Traineeship Trainee, a National Science Foundation Graduate Research Fellow, and a Hertz Fellowship finalist. His research interests include the magnetic control of micro- and mesoscale robots.

Jake J. Abbott (M'05) received the B.S. degree from Utah State University, Logan, UT, USA, in 1999, the M.S. degree from the University of Utah, Salt Lake City, UT, in 2001, and the Ph.D. degree from Johns Hopkins University, Baltimore, MD, USA, in 2005, all in mechanical engineering.

In 2005, he became a Postdoctoral Research Associate with ETH Zurich, Switzerland. In 2008, he became an Assistant Professor with the Department of Mechanical Engineering, University of Utah, where he is the Head of the Telerobotics Laboratory.

Dr. Abbott received the NSF Faculty Early Career Development Award and the 2010 ICRA Best Manipulation Paper Award.

CHAPTER 5

MANAGING MAGNETIC FORCE APPLIED TO A MAGNETIC DEVICE BY A ROTATING DIPOLE FIELD

Prior work has generally made the assumption that the magnetic force applied to a rotating magnetic device by a rotating-permanent-magnet actuator is always attractive in nature. However, in the following paper that was originally published in the journal *Applied Physics Letters*, I present a magnetic phenomenon that actually enables the magnetic force to be directed laterally (i.e., neither attractive nor repulsive) by adjusting the angular velocity of the rotating permanent magnet. This phenomenon can be exploited to contribute toward the propulsion of a rolling untethered magnetic device or limit the magnetic force (e.g., for safety).

APPLIED PHYSICS LETTERS **99**, 134103 (2011)

Managing magnetic force applied to a magnetic device by a rotating dipole field

Arthur W. Mahoney[1,a)] and Jake J. Abbott[2]
[1]*School of Computing, University of Utah, Salt Lake City, Utah 84112, USA*
[2]*Department of Mechanical Engineering, University of Utah, Salt Lake City, Utah 84112, USA*

(Received 31 May 2011; accepted 14 August 2011; published online 29 September 2011)

We demonstrate that the attractive magnetic force acting on a rotating magnetic device (e.g., a magnetic microrobot), actuated using a rotating magnet dipole, can be converted into a lateral force by rotating the actuator dipole according to a specific open-loop trajectory. Results show rotating magnetic devices can be rolled and simultaneously pushed along a surface by the lateral force, resulting in significant increase in velocity. We also demonstrate that the lateral force magnitude can be sufficient to levitate the magnetic device. The results apply to rotating magnetic devices of any size provided inertia has a negligible contribution to its dynamics. © *2011 American Institute of Physics*. [doi:10.1063/1.3644021]

Untethered robots at the micro and mesoscale have become an active area of research because of their potential impact to minimally invasive medicine.[1] Devices fabricated with a magnetic component, on which forces and torques are applied by an external magnetic field, are demonstrating particular promise. Approaches to magnetic locomotion include pulling using magnetic forces and those, where the primary mode of operation is rotation, such as helical propulsion and rolling. In the case of rotating devices using a single rotating permanent magnet as the field source,[2–4] the magnetic dipole field generates torque, which causes the device to rotate while simultaneously generating a magnetic force that typically tends to attract the device toward the permanent magnet (Figs. 1(a) and 1(c)).

For *in vivo* medical applications, an attractive force too large in magnitude may cause the magnetic device to pull toward the actuator, resulting in tissue deformation and potentially trauma. The problem may become self-compounding as the magnitude of the attractive force increases dramatically with decreasing distance from the magnetic actuator. For practical use, the attractive force must be manageable, and in some cases it may need to be substantially eliminated. In this study, we demonstrate that if the actuating permanent magnet is driven according to a specific open-loop rotation trajectory of nonconstant speed, the attractive magnetic force acting on a magnetic device vanishes and is converted into a lateral force nearly constant in magnitude. This lateral force may oppose or contribute to the rolling of the device on a surface (Figs. 1(b) and 1(d), respectively), and it can be large enough in magnitude to overcome the device's weight when oriented against the gravity. This study presents theoretical and experimental analysis of this phenomenon. The results apply to any rotating magnetic device ranging in size from the microscale (e.g., a magnetic microrobot) to the mesoscale (e.g., a magnetic capsule endoscope), actuated by a single rotating permanent magnet, provided that inertial effects are negligible. Such devices may roll on a surface[2,3] or employ a helix to generate forward motion out of rotation.[4,5]

a)Electronic mail: art.mahoney@utah.edu.

Define a stationary world frame with axes {**x**, **y**, **z**}. Assuming that the applied magnetic field **B** is generated using a single magnetic dipole (referred to as the actuator magnet) with dipole moment **M** that can be accurately approximated using the point-dipole model, then **B** at the position of the magnetic device, described relative to the center of the actuator magnet with vector **p**, is

$$\mathbf{B} = \frac{\mu_0}{4\pi|\mathbf{p}|^3}\left[3\frac{\mathbf{p}\mathbf{p}^T}{|\mathbf{p}|^2} - \mathbb{I}\right]\mathbf{M} = \frac{\mu_0|\mathbf{M}|}{4\pi|\mathbf{p}|^3}\begin{bmatrix}0\\ \sin(\theta)\\ 2\cos(\theta)\end{bmatrix}, \quad (1)$$

where μ_0 is the permeability of free space constant, $\mathbb{I}$ is the identity matrix, and θ describes a specific parameterization shown in Fig. 2. Without loss of generality, the rightmost equality in Eq. (1) constrains **p** to lie on the **z** world axis with the actuator rotating around the **x** world axis, constraining **M** to the **y**-**z** plane.

The magnetic torque $\boldsymbol{\tau}$ produced on a dipole moment **m** (i.e., the moment of the magnetic body attached to the rotating device) by the applied field **B** causes **m** to align with **B** and is expressed by $\boldsymbol{\tau} = \mathbf{m} \times \mathbf{B}$. The magnetic torque causes the device to rotate in the opposite rotation direction of the actuator **M**. We model the magnetic device's rotational dynamics rolling on a surface or rotating in a fluid or lumen using the applied magnetic torque and a linear drag torque with coefficient c, while assuming that the torque due to the device's inertia is negligible. If ϕ measures the angle of **m** from the **z** axis, then the device's rotational dynamics are

$$-c\dot{\phi} + |\mathbf{m}||\mathbf{B}|\sin(\alpha) = 0, \quad (2)$$

implying that $\dot{\phi}$ is linearly coupled to the rotating actuator by the magnetic torque, which is maximized when $\alpha = 90°$. By examining the conditions when $\alpha = 90°$ at steady-state, according to Eq. (2), we find that the actuator must be driven so that its rotation velocity $\dot{\theta}$ follows

$$\dot{\theta} = \frac{\mu_0|\mathbf{m}||\mathbf{M}|}{8\pi|\mathbf{p}|^3 c}\left(1+3\cos^2(\theta)\right)^{\frac{3}{2}} = K\left(1+3\cos^2(\theta)\right)^{\frac{3}{2}}. \quad (3)$$

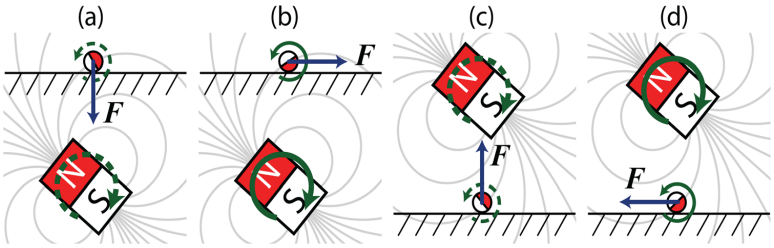

FIG. 1. (Color online) When rotating the actuator quasistatically, the magnetic force tends to attract the magnetic device (e.g., a microrobot) toward the actuator while causing it to roll (a), (c). Operating the actuator dynamically as described herein causes the magnetic force to oppose the magnetic device's rolling motion in the case where the rolling surface lies between the rotating actuator and the device (b) and to contribute to rolling otherwise (d).

Driving the actuator according to Eq. (3) stably maintains $\alpha = 90°$; it can be shown that $\alpha \to 90°$ as $t \to \infty$ for any initial conditions of α and θ. Although the magnetic force acting on the device influences the coefficient c, significant effects to the rotational behavior of the device actuated in this paper are not observed.

Eq. (3) requires the actuator's orientation θ, the device's position $\mathbf{p}$, and the speed coefficient K to be known but does not require measurement of the device's magnetized orientation, which can be difficult for some devices such as microrobots of spherical or cylindrical (polarized diametrically) geometry. In practice, θ is known, the device's position $\mathbf{p}$ can be measured using a variety of methods such as computer vision or medical imaging, and an estimate $\hat{K}$ is used in place of K. If $\hat{K} \leq K$, then it can be shown that α converges to $\sin^{-1}(\hat{K}/K)$. If $\hat{K} > K$, no steady-state α exists and the device will step out of synchronization with the actuator. $\hat{K}$ can be measured by incrementally increasing $\hat{K}$ until the device is observed to step out of synchronization with the actuator, at which time $\hat{K} \approx K$.

When the magnetic device is positioned as in Fig. 2 and the actuator is rotating according to Eq. (3), making the device's dipole moment $\mathbf{m}$ lag the applied field $\mathbf{B}$ by 90°, then we find that the magnetic force $\mathbf{F} = (\mathbf{m} \cdot \nabla)\mathbf{B}$ acting on the device, using Eq. (1), is

$$\mathbf{F} = \frac{3\mu_0|\mathbf{m}||\mathbf{M}|}{4\pi|\mathbf{p}|^4}\left(\frac{1+\cos^2(\theta)}{\sqrt{1+3\cos^2(\theta)}}\right)\begin{bmatrix}0\\-1\\0\end{bmatrix}. \quad (4)$$

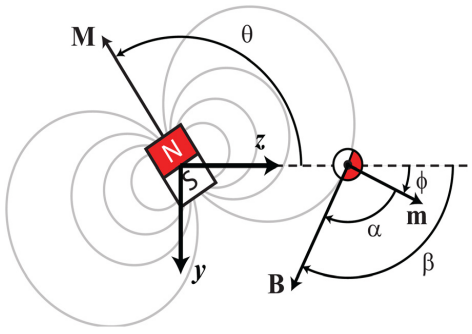

FIG. 2. (Color online) The magnetic device is positioned on the **z** axis and the actuator magnet rotates around the **x** axis (out of the image), constraining the actuator and device dipole moments, **M** and **m**, respectively, to the **y**-**z** plane.

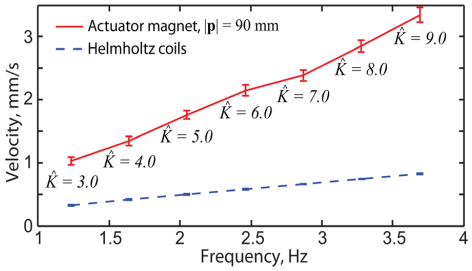

FIG. 3. (Color online) Rolling velocity of the magnetic device as a function of rotation frequency obtained with the actuator positioned 90 mm above the device (Fig. 1(d)) and using a triaxial Helmholtz coil system.[5] Each data point is the average of four trials, and the error bars denote one standard deviation.

When the actuator rotates in the positive direction while satisfying Eq. (3), the applied magnetic force lies in the negative **y** direction. In general, if $\boldsymbol{\Omega}$ represents the actuator's angular velocity vector, then the magnetic force points in the direction of $\boldsymbol{\Omega} \times \mathbf{p}$. No component of the magnetic force attracts the device to the actuator. The magnitude $|\mathbf{F}|$ in Eq. (4) varies from 94.3% to 100% of $\frac{3\mu_0|\mathbf{m}||\mathbf{M}|}{4\pi|\mathbf{p}|^4}$ as θ changes, making the magnetic force nearly constant in magnitude.

The method presented herein was verified experimentally using a magnetic device consisting of a diametrically polarized NdFeB (Grade N42) cylindrical magnet 6.35 mm in length and 3.17 mm in diameter, weighing 1.2 g. The

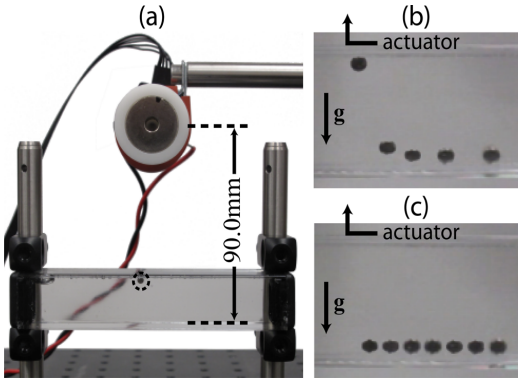

FIG. 4. (Color online) An experimental setup (a) with the magnetic device circled. Image sequences show the device driven right to left using 1.23 Hz actuation with (b) a constant angular velocity and (c) according to Eq. (3) with $\hat{K} = 3.0$. Use of Eq. (3) significantly reduces the attractive magnetic force (enhanced online). [URL: http://dx.doi.org/10.1063/1.3644021.1]

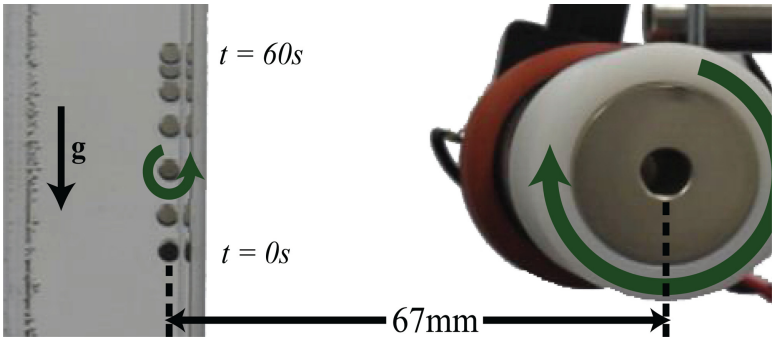

FIG. 5. (Color online) Image sequence shows the magnetic force, the subject of this work, levitating the magnetic device against both its weight and the rolling force. The image sequence begins at $t = 0$ s where the device is at static equilibrium and rises 24 mm to a dynamic equilibrium at $t = 60$ s with the actuator rotation satisfying Eq. (3) for $\hat{K} = 20$. Images are shown in 10 s increments (enhanced online). [URL: http://dx.doi.org/10.1063/1.3644021.2]

device was actuated using magnetic fields produced by a diametrically polarized NdFeB (Grade N42) cylindrical magnet 25.4 mm in length and diameter with magnetic moment $|\mathbf{M}| = 12.6$ A $\cdot$ m^2, driven by a Maxon 24 V A-Max DC motor with an Advanced Motion Controls servo control drive and amplifier. For any $\hat{K}$, the actuator's instantaneous rotation speed (given by Eq. (3)) varies with the actuator's orientation from $\hat{K}$ to $8\hat{K}$ throughout each cycle with an effective peak-to-peak frequency $f \approx 0.41\hat{K}$ Hz. To remain within the torque constraints of the motor while demonstrating the effects of applied force, the drag coefficient c was increased by immersing the magnetic device in a rectangular acrylic tank of corn syrup. A triaxial Helmholtz coil system,[5] which generates uniform magnetic fields and force-free magnetic torque, is used for experimental comparison.

When $\hat{K} < K$ and $\alpha < 90°$ at steady-state, we find numerically that the horizontal and attractive components of the magnetic force are nonzero and fluctuate with θ. As $\hat{K} \to K$, the average lateral and attractive components over one actuator cycle increase and decrease, respectively, until the magnetic force converges to Eq. (4) when $\hat{K} = K$. Fig. 3 shows the horizontal device rolling velocity when positioned as in Fig. 1(d) and actuated according to Eq. (3) with increasing $\hat{K}$. Fig. 3 also shows the horizontal rolling velocity when actuated within the Helmholtz system at equivalent frequencies for comparison. The Helmholtz system applies negligible force; therefore, the significant increase in velocity when driven with the actuator magnet is attributable to the horizontal magnetic force that is the subject of this work. As $\hat{K}$ increases, the horizontal magnetic force and its contribution to the horizontal velocity increase as shown. As $|\mathbf{p}|$ increases, we expect the contribution of the applied force will diminish as $|\mathbf{p}|^{-4}$, making the velocity approach that in the Helmholtz system.

Previous approaches consider quasistatic actuation using a single rotating permanent magnet at constant frequencies where the lead angle α is small.[2–4] When operated in this manner, the magnetic force always attracts the magnetic device toward the actuator magnet. Operating the actuator according to Eq. (3) reduces the attractive force even at equivalent frequencies. Figs. 4(b) and 4(c) show an image sequence of the device operated by rotating the actuator at a constant angular velocity of 1.23 Hz compared to rotating the actuator according to Eq. (3) with the same frequency. With a constant angular velocity, although the magnetic force initially pulls the device in the rolling direction at 1.67 mm/s, it decelerates as the magnetic force transitions upward and overcomes the device's weight, attracting the device toward the actuator. Driving the actuator according to Eq. (3) reduces the attractive magnetic force, and the device remains on the lower surface while traveling at 0.78 mm/s.

Aside from managing the magnetic force in a manner that simultaneously reduces the attractive component and contributes to the device's rolling velocity, the magnetic force can also be used for levitation. Fig. 5 shows an image sequence with the device configured according to Fig. 1(b) (rotated 90°). The device begins at $t = 0$ s in its static equilibrium position with no actuator rotation and rises 24 mm to its dynamic equilibrium position at $t = 60$ s when actuated according to Eq. (3) with $\hat{K} = 20$. When the actuator rotates clockwise, the device rotates counterclockwise producing a rolling force in the same direction as gravity. The component of the applied magnetic force causing the device to levitate, therefore, opposes both the rolling force and the device's weight, resulting in a net vertical motion, while the remaining attractive component pins the device to the wall.

We have demonstrated theoretically and experimentally that the attractive magnetic force acting on a rotating magnetic device can be diminished and converted into a lateral force when positioned as in Fig. 2 and actuated according to Eq. (3) in an open-loop fashion. Such operation can be used to simultaneously roll and push a device on a surface, resulting in potentially significant increases in rolling velocity, or it may be used for device levitation. Although the experiments were performed on a millimeter-scale device, the results of this work apply to rotating magnetic devices of any size with negligible inertia actuated with a single rotating magnetic dipole.

This work is supported by the National Science Foundation under Grant Nos. IIS-0952718 and DGE-0654414.

[1]B. J. Nelson, I. K. Kaliakatsos, and J. J. Abbott, Annu. Rev. Biomed. Eng. **12**, 55 (2010).
[2]M. T. Hou, H.-M. Shen, G.-L. Jiang, C.-N. Lu, I.-J. Hsu, and J. A. Yeh, Appl. Phys. Lett. **96**, 024102 (2010).
[3]G.-L. Jiang, Y.-H. Guu, C.-N. Lu, P.-K. Li, H.-M. Shen, L.-S. Lee, J. A. Yeh, and M. T.-K. Hou, J. Micromech. Microeng. **20**, 085042 (2010).
[4]J.-S. Lee, B. Kim, and Y.-S. Hong, Int. J. Precis. Eng. Manuf. **10**, 27 (2009).
[5]A. W. Mahoney, J. C. Sarrazin, E. Bamberg, and J. J. Abbott, Adv. Rob. **25**, 1007 (2011).

CHAPTER 6

DISCUSSION AND FUTURE POSSIBILITIES

The desire to wirelessly affect an untethered device has led researchers to study magnetic manipulation for quite some time. Many approaches have been developed that employ electromagnets and permanent magnets, and many forms of device propulsion have been applied. Magnetic manipulation is already beginning to have an impact on minimally invasive medicine in the form of magnetic catheter guidance systems [1], [2] and other procedures such as capsule endoscopy [3]–[5]. With the progress of current research, further proliferation of magnetic technology into medicine is almost certain. There are many future possibilities for magnetic systems that employ rotating and nonrotating magnetic fields.

In Chapters 4 and 5, the rotating magnetic field is created using a single permanent magnet. An immediate extension to the state-of-the-art is to use multiple permanent magnets. As demonstrated in [6], nonuniform magnetic fields can be exploited to independently apply forces to individual rotating magnetic devices in a group. In [6], the nonuniform magnetic fields are generated by an arrangement of electromagnets. Creating a nonuniform, rotating magnetic field using multiple permanent magnets (or other dipole sources) has not yet been explored. The results of Chapter 4 may be used to understand the behavior of multiple superimposed rotating dipole fields, although the combined field is likely to have much more complicated behavior than a single rotating dipole field itself. Many properties can be explored. For example, the field measured at a position in space relative to two rotating permanent magnets can have different behavior depending on the phase-lag between both magnets. In some configurations, a 180° phase lag could result in no field being measured (i.e., the field contributed by each rotating magnet perfectly cancels). As another example, the rotation axis of the measured magnetic field generated by a single rotating permanent is well understood from Chapter 4; however, when superimposing multiple rotating dipole fields, the *net* rotation axis of the combined field measured at a position in space is unclear. Understanding the net behavior of superimposed rotating dipole fields could have future

applications for the control of one or multiple untethered magnetic devices.

Employing multiple nonrotating actuator magnets for magnetic manipulation is another area where the state-of-the-art can be advanced. To date, the most successful system utilizing multiple nonrotating permanent magnets is the Stereotaxis Niobe system for cardiac catheter guidance [2]. The Stereotaxis system integrates two large permanent magnets positioned on either side of the patient and a C-arm fluoroscope system positioned at the patient's head. The magnets are oriented robotically in a manner that enables the applied magnetic torque on the tip of a magnetic catheter to be controlled while applying approximately no magnetic force to the catheter's tip. In fact, due to the configuration of the permanent magnets, the applied magnetic force cannot be controlled independently of the magnetic torque. A more capable system can be made by using more permanent magnets, each with a smaller volume. For example, retrofitting the five arms of a da Vinci surgical robot with five end-effectors that each encapsulate a permanent magnet could be used to remotely manipulate a catheter or other surgical instrument with more degrees-of-freedom than the Stereotaxis Niobe system (additionaly, two da Vinci systems could be positioned opposite each other, making a total of ten actuator magnets). The more permanent magnets a system incorporates, the more flexibility it will have to dynamically select permanent-magnet configurations that optimize a desired measure of manipulability subject to geometric constraints. For example, if a C-arm fluoroscope is used for guidance, then the magnets should be kept from configurations that might interfere with imaging.

A major factor that limits the clinical use of permanent magnet systems is safety. Unlike electromagnets, permanent magnets cannot be shut off in an emergency. In the case of the Stereotaxis Niobe system, the permanent magnets are extremely large, and great care must be taken even when not in use. There are several techniques to "shut off" the effect of a permanent magnet's field to some extent. In [7], I show that spinning an actuator magnet well above the step-out frequency of an untethered magnetic device causes the time-averaged applied magnetic force to drop to zero. In the case of a tethered device (e.g., a magnet-tipped catheter), a step-out frequency does not technically exist but the same principle applies. The simplest approach to "shut off" a permanent magnet's field is to exploit the fact that magnetic torque drops off with increasing distance as d^{-3}, and magnetic force drops off as d^{-4} by pulling the actuator magnet away from the magnetic device.

Both approaches are applicable to systems that employ static or rotating permanent magnets, but neither approach instantly turns off the field. In this regard, a system employing multiple small permanent magnets (rather than one large one) may have an

advantage. When positioned near one another and operated in concert, multiple small permanent magnets can produce a field of similar magnitude as a field created by one larger magnet. In the case of an emergency, the total field generated by multiple small magnets may be reduced faster than the field generated by one large magnet by moving the small magnets away from the workspace and simultaneously increasing their separation distance from each other. Additionally, a large magnet must be treated with caution even when not in use. Multiple smaller magnets may be benign individually, provided they are not brought near each other simultaneously.

The study presented in Chapter 5 was limited to a specific configuration where the relative position between the rotating-permanent-magnet actuator and the untethered magnetic device is orthogonal to the actuator magnet's rotation axis (this is one of the configurations where the behavior of the rotating magnetic field is easy to visualize). The results of Chapter 4, however, enables the untethered device to be actuated in any configuration (not just those that are easy to understand). This leads to the natural extension of the study presented in Chapter 5 to all configurations. In a preliminary study, I have found that the applied magnetic force acting on an untethered magnetic device can always be directed laterally (i.e., neither attractive nor repulsive), regardless of the magnetic device's position in space [8]. In addition, there always exists a tradeoff between the applied magnetic torque and the applied magnetic force, i.e., the applied magnetic torque is always maximized when the applied magnetic force is minimized. The extent of this tradeoff varies with the position of the untethered magnetic device. For devices that can be propelled with both the magnetic torque and force, this tradeoff readily lends itself to an optimization problem that determines where the optimal position of the rotating magnet should be and how fast it should rotate to produce the best combination of magnetic torque and force for device propulsion (note that I have largely solved this problem for simple propulsion models).

Aside from the field of medicine, magnetic manipulation is also beginning to impact materials science and biology. For example, in a recent *Nature Communications* article, Tasoglu et al. use an untethered magnetic microrobot to assemble functional materials with tunable structural, morphological, and chemical features [9]. Untethered magnetic devices have been used to capture protein crystals [10], and in [11], an untethered microrobot device is fabricated on which cells can be cultured and then transported for targeted delivery. The understanding of helical-microswimmer control is advancing to the point where they can be used to manipulate individual biological cells [12], [13]. The ability to control multiple microswimmers can increase their usefulness as manipulation devices. Currently,

multiple helical microswimmers have only been controlled as a group or semiselectively on a two-dimensional plane. The results of Chapter 2 could be used to simultaneously control the spatial velocities of multiple helical microswimmers that are differentiated by their physical geometry (i.e., size, helix pitch, etc.) in three dimensions rather than a two-dimensional plane (note that three-dimensional control of multiple magnetic devices has only been demonstrated in [6]). The helical microswimmers could be further differentiated using their magnetization by employing the results of Chapter 3.

Because most prior work has used helical microswimmers constrained to a planar surface, there still remain questions about their behavior in three dimensions. For example, the behavior of a helical-microswimmer when operated above its step-out frequency is well understood when on a two-dimensional surface (see Chapter 3). When not in contact with a surface, however, the behavior of a helical-microswimmer above step-out has not been studied. An additional problem that remains to be studied is the stability of helical-microswimmers while steering. In general, it has been taken for granted that a swimmer's lowest energy state is the configuration where the swimmer's principle axis is aligned with the field's rotation axis. Since a swimmer always wants to be in the lowest energy state possible, adjusting the rotation axis of the applied field causes the swimmer to realign its principle axis with the field's rotation axis (thus steering the swimmer in space). However, it has been observed that when performing large-angle steering at high rotation speeds, the swimmer can become unstable. Understanding this behavior will lead to a better understanding of how to control helical swimmers.

Most prior work employs uniform magnetic fields, generated by triaxial arrangements of Helmholtz coils, to actuate helical microswimmers in bench-top settings. Uniform magnetic fields apply no magnetic force to a helical microswimmer and as a result, the dynamics of helical microswimmers under pure magnetic torque are well understood. Using nonuniform magnetic fields to actuate a helical microswimmer has been studied to a limited degree in [14], which uses a rotating permanent magnet. Nonuniform magnetic fields have the ability to simultaneously apply a magnetic force and a magnetic torque for the propulsion of a swimmer. In general, the spatial and angular velocity of a helical microswimmer are linear combinations of the applied magnetic force and torque. There are interesting implications of this coupling on the control of helical microswimmers in nonuniform fields that are not fully understood. For example, a magnetic force applied parallel to a swimmer's principle axis can effect the swimmer's step-out frequency (the highest frequency that synchronous rotation can be maintained). If the swimmer's helix is right-handed (i.e., the swimmer

moves in the direction of the applied magnetic torque in the presence of no magnetic force), then a magnetic force applied in the same direction as the magnetic torque (i.e., it assists propulsion) results in an increase in the swimmer's step-out frequency. When the magnetic force is applied in the opposite direction (i.e., it impedes propulsion) results in a decrease in the swimmer's step-out frequency. If the swimmer is actuated with a rotating permanent magnet, then this phenomenon has implications for the rotating-permanent-magnet configuration that optimizes device propulsion. This phenomenon may also have interesting implications for the control of multiple swimmers.

6.1 References

[1] G. T. Gillies, R. C. Ritter, W. C. Broaddus, M. S. Grady, M. A. Howard III, and R. G. McNeil, "Magnetic manipulation instrumentation for medical physics research," *Rev. Sci. Instrum.*, vol. 65, no. 3, pp. 533–562, 1994.

[2] "Stereotaxis Niobe Magnetic Navigation System," http://www.stereotaxis.com/niobe.html.

[3] H. Keller, A. Juloski, H. Kawano, M. Bechtold, A. Kimura, H. Takizawa, and R. Kuth, "Method for navigation and control of a magnetically guided capsule endoscope in the human stomach," in *Proc. IEEE Int. Conf. Biomed. Robot. Biomechatron.*, 2012, pp. 859–865.

[4] J. F. Rey, H. Ogata, N. Hosoe, K. Ohtsuka, N. Ogata, K. Ikeda, H. Aihara, I. Pangtay, T. Hibi, S. Kudo, and H. Tajiri, "Feasibility of stomach exploration with a guided capsule endoscope," *Endoscopy*, vol. 42, no. 7, pp. 541–545, 2010.

[5] J. L. Toennies, G. Tortora, M. Simi, P. Valdastri, and R. J. Webster III, "Swallowable medical devices for diagnosis and surgery: the state of the art," *J. Mech. Eng. Sci.*, vol. 224, no. 7, pp. 1397–1414, 2010.

[6] E. Diller, J. Giltinan, and M. Sitti, "Independent control of multiple magnetic microrobots in three dimensions," *Int. J. Robot. Res.*, vol. 32, no. 5, pp. 614–631, 2013.

[7] A. W. Mahoney and J. J. Abbott, "Generating rotating magnetic fields with a single permanent magnet for propulsion of untethered magnetic devices in a lumen," *IEEE Trans. Robot.*, vol. 30, no. 2, pp. 411–420, 2014.

[8] A. W. Mahoney, S. E. Wright, and J. J. Abbott, "Managing the attractive magnetic force between an untethered magnetically actuated tool and a rotating permanent magnet," in *Proc. IEEE Int. Conf. Robot. Autom.*, 2013, pp. 5346–5351.

[9] S. Tasoglu, E. Diller, S. Guven, M. Sitti, and U. Demirci, "Untethered micro-robotic coding of three-dimensional material composition," *Nat. Commun.*, vol. 5, no. 3124, pp. 1–9, 2014.

[10] H.-W. Tung, D. F. Sargent, and B. J. Nelson, "Protein crystal harvesting using the rodbot: a wireless mobile microrobot," *J. Appl. Crystallogr.*, vol. 4, pp. 692–700, 2014.

[11] S. Kim, F. Qiu, S. Kim, A. Ghanbari, C. Moon, L. Zhang, B. J. Nelson, and H. Choi, "Fabrication and characterization of magnetic microrobots for three-dimensional cell

culture and targeted transportation," *Adv. Mater.*, vol. 25, no. 41, pp. 5863–5868, 2013.

[12] K. E. Peyer, L. Zhang, and B. J. Nelson, "Localized non-contact manipulation using artificial bacterial flagella," *Appl. Phys. Lett.*, vol. 99, no. 174101, pp. 1–3, 2011.

[13] S. Tottori, L. Zhang, F. Qiu, K. K. Krawczyk, A. Franco-Obregón, and B. J. Nelson, "Magnetic helical micromachines: fabrication, controlled swimming, and cargo transport," *Adv. Mater.*, vol. 24, no. 6, pp. 811–816, 2012.

[14] T. W. R. Fountain, P. V. Kailat, and J. J. Abbott, "Wireless control of magnetic helical microrobots using a rotating-permanent-magnet manipulator," in *Proc. IEEE Int. Conf. Robot. Autom.*, 2010, pp. 576–581.

CHAPTER 7

CONCLUSION

This dissertation is motivated by problems in microscale manipulation and minimally invasive medicine that require a small untethered device to be wirelessly manipulated and controlled either under a microscope (e.g., helical microswimmers) or within the human body (e.g., capsule endoscopes). This dissertation has presented advancements in exerting force and torque to untethered devices, fabricated with a magnetic body, by externally applied rotating magnetic fields. The rotating fields can be created using specially designed electromagnetic systems or using rotating permanent magnets.

Many untethered magnetic devices with varying methods of propulsion have been developed. In Chapter 2, a method is presented to control the spatial velocity of helical microswimmers (devices that replicate the helical propulsion of natural bacterial flagella) in three-dimensional fluid, using a uniform rotating magnetic field created by an electromagnet arrangement called a Helmholtz system. The work presented in Chapter 2 first developed a six degree-of-freedom model for a helical swimmer of arbitrary geometry and then applied it to solve the inverse problem of determining the correct field rotation axis and frequency that achieve a desired three-dimensional swimmer spatial velocity. The results make the control of helical swimmers more intuitive for a human operator, opening the doors for coordinated use of helical microswimmers in three dimensions.

Helical microswimmers have been applied to the task of manipulating microscale objects (e.g., biological cells) underneath a microscope. The ability to control multiple untethered magnetic devices (e.g., helical microswimmers) simultaneously is a grand-challenge problem in the field of microscale manipulation. Chapter 3 presented analysis and experimental results that describe an unintuitive behavior of untethered magnetic devices when placed in a rotating magnetic field that rotates above their step-out frequency (the frequency where the applied magnetic torque is not strong enough to keep the device rotating synchronously with the applied field). The phenomenon is exploited to add a level of differentiation for the simultaneous control of multiple rotating magnetic devices, thus demonstrating that

operating a rotating untethered magnetic device above its step-out frequency can, in fact, be useful (contrary to the assumptions of prior work).

Due to the fact that permanent magnets can create stronger magnetic fields than electromagnets in smaller form-factors, permanent-magnet actuation systems are gaining attention for clinical applications. The complex geometry of a rotating dipole field, generated by a rotating magnet, makes the behavior of the field difficult to understand and visualize in most configurations. This has limited the use of rotating permanent magnets to control untethered magnetic devices except in specific configurations where the field is easy to understand. Chapter 4 presents an analysis of the behavior of a rotating dipole field that enables a magnetic devices to be controlled in all configurations, not just those that are simple to visualize. The results enable much more flexible use of a rotating permanent magnet for the actuation of untethered magnetic devices.

In prior work, the magnetic force applied to a magnetic device by a single rotating permanent magnet was assumed to be attractive in nature. Chapter 5 presented an analysis of the applied magnetic force, which predicted that the force could actually be manipulated to point in a lateral direction (i.e., neither attractive nor repulsive). This phenomenon was demonstrated in Chapter 5 by varying the rotation speed of the rotating-permanent-magnet actuator. The ability to direct the applied magnetic force, in previously unknown ways, can be useful for simultaneously applying magnetic torque and force for device propulsion and safety in clinical applications. Both uses are demonstrated in Chapter 5.

The results of this dissertation advance the state-of-the-art of magnetic manipulation by making magnetic systems that employ rotating magnetic fields more intuitive to control, able to control multiple devices simultaneously, and increasing our understanding of how the field and forces generated by a single rotating permanent magnet behave. The results contribute to the body of research that is paving the way for further proliferation of magnetic technology into medicine and manipulation.